Coating and hydrodynamics of random column packing Dixon rings

Mohamed Abdelraouf

A thesis submitted to Lancaster University in partial fulfilment of the requirements for the degree of

Doctor of Philosophy

June 2022

Engineering Department

Faculty of Science and Technology

Lancaster University

s

Declaration

I declare that this thesis is the result of my own independent work/investigation, except where otherwise stated. Other sources are acknowledged by explicit references.

June 2022

Acknowledgments

I want to thank all my supervisors for their help without them this journey wouldn't be possible. Thank you, Farid, Vesna and Allan! I'd also would love to thank my parents for giving me all the support I need during the tough times. Thanks for the financial support from the Centre for Global Eco-Innovation at Lancaster University, the European Regional Development Fund (Grant Reference: 03R17P01835 – Eco-Innovation Cheshire and Warrington) and Croft Filters Ltd, Warrington, UK.

Contents

Table of figures

Table of tables

Acronyms

Nomenclature

a_e	Effective area ($m^2.m^{-3}$)
a_p	Packing area per unit volume ($m^2.m^{-3}$)
c	Capillary width (m)
C	Conductivity ($mS.cm^{-1}$)
d_p	Packing diameter (m)
E(t)	Residence time distribution (-)
G	Chemical potential density ($J.m^{-2}$)
g	Gravity constant ($m.s^{-2}$)
h_L	Liquid holdup (-)
h_o	Static liquid holdup (-)
f_o	friction factor (-)
F_g	Gravitational forces (N)
F_{r_L}	Froude number (-)
F_s	Surface tension forces (N)
p	Pressure (Pa)
ΔP_{dru}	Dry pressure drop (Pa)
ΔP_{wet}	Wet pressure drop (Pa)
R_e	Reynolds number
T	Viscous deformation tensor
u_0	Liquid inlet velocity ($m.s^{-1}$)
z	Packing height (m)
u_g	superficial gas velocity ($m.s^{-1}$)
W_e	Weber number (-)
V_f	Volume fraction

Abbreviations

AFM	Atomic force microscopy
AIP	Aluminum isopropoxide
Al_2O_3	Alumina
BET	Brunauer, Emmett and Teller
CCD	Charged Couple Device
$CCI_{Grad,95,th}$	95^{th} confidence intervals values
CFD	Computational fluid dynamics
CVD	Chemical vapour deposition
DEM	Discretized element method
EDS	Energy-dispersive X-ray spectroscopy
FEM	Finite Element Method
FVM	Finite Volume Methods
HMDS	Hexamethyldisilazane
MEA	Monoethanolamine
PEI	Polyethylenimine
PVD	Physical vapor deposition
RPM	Rotations per minute
SCMOS	Complementary Metal–Oxide–Semiconductor
TEOS	Tetraethyl orthosilicate
TBR	trickle bed reactors
MTS	Methyltrichlorosilane
MTEOS	Methyltriethoxysilane
VOF	Volume of Fluid
SE	Standard error
SEM	Scanning electron microscope
XRD	X-ray powder diffraction

Greek letters

ρ_L	Liquid Density (kg/m^3)
ρ_g	Gas density (kg.m^{-3})
μ_L	Liquid viscosity (kg/m.hr)
σ_L	Surface tension coefficient (N/m)
β	Slip length (m)
ϕ	Phase field variable (-)
λ	Mixing energy density (N)
τ	Average residence time (s)
γ	Mobility parameter (-)
ε	Packing porosity (-)
θ	Contact angle (°)

Abstract

In this thesis, three main objectives were covered using experiments and modelling studies. Firstly, the coating of Dixon rings cheaply and repeatably using alumina sol-gel. Secondly, the new understanding of fluid flow over curved wire meshes. Thirdly, the effect of Dixon rings on process parameters such as pressure drop, liquid holdup and mass transfer coefficient were investigated using experiments and model.

Packed columns are filled with solid structures to improve the heat and mixing of multiphase processes. The packing usually interacts with the fluid, increasing the mixing but creating a pressure drop. Packing are typically evaluated based on their hydrodynamic behavior, such as pressure drop, liquid holdup, and mass transfer coefficient. Packing with low-pressure drop, high mass transfer, and high flooding velocities are the preferred choice for users. Wire mesh packing are an example of packing that offer low-pressure drop and increased mass transfer. The pore openings in the mesh provide a path for the gas to flow, resulting in good mixing and low-pressure drop. Dixon rings are an example of wire mesh packings made of stainless steel and rolled into a cylindrical shape with a bisecting section in the middle. The stainless-steel structure of Dixon rings makes them resistant to high temperature and chemical constraints. Packing with such properties has great potential in water treatment, hydrocracking, and more. However, the hydrodynamic behavior of Dixon rings has not been investigated deeply in the literature.

Secondly, a new understanding of fluid flow on a microscale and macroscale over curved surface of the wire mesh was achieved. The macroscale experiments were conducted in a semi-pilot plant with gas and liquid flow in counter-current for the uncoated Dixon rings. The effect of Dixon rings on pressure drop, liquid holdup, and mass transfer were measured and compared to commercial packing of similar size and material. The microscale study was focused on the liquid flow distribution, which is critical in the design and operation of packed columns. The liquid flow distribution changes the packing's wetting efficiency, affecting several hydrodynamic parameters, such as the liquid holdup and the effective surface area. The liquid wetting efficiency was evaluated using imaging experiments and CFD simulations for the coated and uncoated Dixon rings. The flow regime and several hydrodynamic parameters such as liquid holdup, effective surface area, and pressure drop were anticipated to affect the mass transfer capabilities highly.

Finding smaller unit operations is required to cut down the global emission. It is not a surprise that process intensification is needed in packed columns. Packing with a tunable surface can achieve both hydrophobic and hydrophilic properties that are highly desired due to their tendency to control the liquid dispersion and wetting properties. Changing the surface properties using uniform coating is a common approach to produce tunable contact angle and surface wetting. Coating metals have been fraught with difficulties, and Dixon rings have a complex geometry which hinders their use in many applications, specifically when a coating is required. This research considered the application of a uniform adhesive coating via the sol-gel deposition method of alumina on Dixon rings. The coated film was investigated for the first time on stainless steel wire mesh for use as Dixon rings. The kinetics of deposition of the sol-gel was followed for a range of initial compositions of the coating, such as the ratios of alumina to water, acid content, polyethyleneimine binder content and the number of deposition cycles. The coated Dixon rings were characterised by surface optical microscopy, scanning electron microscopy (SEM), energy-dispersive X-ray spectroscopy (EDS), and Brunauer, Emmett and Teller (BET). Adhesive tests included assessing coating behaviour against shear forces, ultrasound, and temperature constraints. Well-adhered alumina with a thickness of up to 20 µm was successfully deposited.

Imaging experiments and 3D volume-of-fluid modelling investigated the microscale behaviour of liquid flow over coated and uncoated Dixon rings. An alumina coating modified the surface of the wire mesh ring to reach both hydrophilic and hydrophobic characteristics. The contact angle was varied due to the coating and resulted in different mass and heat exchanges of the multiphase chemical systems. The cycle of capillary droplet flow over the uncoated ring exhibited penetration of the hydrophilic mesh openings, adherence to the surface of the ring, and accumulation as drips at the bottom region of the rings. However, over the hydrophobic ring, the droplet exhibited low adherence to the ring surface, accumulation at the top surface of the ring, no penetration of the openings, slipping by the gravitational forces over the vertical curvature and accumulation as drips at the bottom region. In agreement with the classical observations at the macroscale, the observations at the pore-scale confirmed the increase of the wetting efficiency, liquid holdup and effective surface area at increased liquid flowrate and reduced contact angle. The 3D model had a relative deviation of 7.21 % with Stichlmair's model for the liquid holdup, particularly in the hydrophilic zone of the contact angle and low flow as well as a relative deviation of 14.24% with Linek's model for effective area, particularly in the hydrophobic range of the contact angle.

Considering the results at the pore scale, the packing material was then investigated at a larger scale using the non-coated Dixon rings exclusively. The hydrodynamic and mass transfer properties for Dixon rings packing are not currently available within the literature. A semi-pilot plant was used to evaluate the pressure drop, the liquid holdup, and the mass transfer coefficient for Dixon rings packing $^{5}/_{8}$ in and $^{1}/_{4}$ in. The study was extended to various operational conditions for gas and liquid counter-current flow. The results were compared to commercial random packing and validated, showing that Dixon rings offer low-pressure drop, high liquid holdup, and mass transfer coefficient.

Data from classical literature were used for the comparison of pressure drops, liquid holdup, and mass transfer with other random packings of similar size and material with Dixon rings. Selecting appropriate sizes for testing the Dixon rings in fluid flow applications is crucial. Testing small-sized packing for industrial applications is not a realistic approach due to their large pressure and expensive cost of manufacture. On the other hand, large-sized packing rings result in poor mixing. Dixon rings $^{5}/_{8}$Hiflow rings $^{5}/_{8}$ in. Pall rings $^{1}/_{4}$ in were found to have lower pressure drop than Dixon rings$^{1}/_{4}$ in due to the lateral openings. The value of the liquid holdup for Dixon rings $^{1}/_{4}$ in was double the value for Dixon rings $^{5}/_{8}$ in. Pall rings had the highest liquid holdup with a value of 0.5. Conversely, Reflux rings $^{5}/_{8}$ in have the lowest liquid holdup of 0.25. The height equivalent to a theoretical plate (HETP) value for Dixon rings $^{5}/_{8}$ and $^{1}/_{4}$ in were approximately 0.45 and 0.05, respectively. Pall rings $^{5}/_{8}$ in had the highest HETP, which indicates the lowest separation efficiency. In addition to the experimental investigations, models were developed to describe the dry pressure drop and loading point. The 95th centile confidence intervals were evaluated for all models to ensure the model's accuracy. The pressure drop for the dry packing and the loading point behaviour exhibit linear correlations. The Standard of the intercept (SE_{Inter}) was found to be less than 3% for the dry pressure drop and loading point. The standard of the gradient (SE_{Grad}) of the dry pressure drop and loading point were less than 5% and 3%, respectively. The model may not be able to adequately describe the pressure drop when the gas flow rate is small. The low values of standard error (SE) suggested that the models are adequate to use to predict the dry pressure drop and loading region for Dixon rings $^{5}/_{8}$ and $^{1}/_{4}$ in.

This study successfully investigated a method to coat metallic wire mesh packing using sol-gel. The thickness and distribution of the coating were investigated by a parametric analysis for several ratios such as the acid, water, and Al content. Microscopic and SEM tests showed that the coating has a uniform thickness, and adhesive tests were conducted to ensure the coating is well attached to the Dixon rings' surface. This coating method can be used for any type of metallic wire mesh substrate to produce alumina coating with tunable thickness. A microscopic study was implemented to investigate the liquid flow behaviour for coated and uncoated Dixon rings using a 3D VOF model and imaging experiments. The liquid holdup and the effective surface area from the 3D model were compared to results from the literature. The coated Dixon rings have a hydrophobic nature, while the uncoated rings have hydrophilic properties. The pressure drop, liquid holdup and mass transfer value were reported for Dixon rings for the first time on a macroscopic level. Based on the experimental data, models were developed to predict the dry pressure drop and the loading point. The model showed good reliability with a SE less than 5%

1 Chapter 1: Introduction

1.1 Research motivation

In industry, multiphase processes are conducted in columns with different internal configurations such as spray towers, tray columns, and packed columns: either random or structured. Packed columns are widely used due to their low operational costs. Packed bed columns are employed in multiphase systems as they are estimated to account for 40-70% of the capital and operating costs of modern process industries [1]. Packed columns are well-known and widely used in processes in the industry (e.g., distillation, absorption, adsorption, catalytic systems, etc.). A gas-liquid-packed column with catalysed or inert packing is used to carry out operations by sufficiently mixing the reactants [2]. Smaller, cleaner and more efficient processes are needed to reduce emissions. Process intensification in packed columns is highly desired. The packing inside these columns promotes the heat and mass transfer of the reactants or feed material [3]. Therefore, the packing material must be characterised and optimised to yield the maximum efficiency possible for the process. In addition, improvements in liquid flow inside the packed columns regarding relevant flow characteristics are essential. This requires studying hydrodynamics, mass transfer on a local level and at a large scale to help design and develop operations in packed columns. These studies are widely available for commercial packing such as Raschig rings, however they are still missing for some packing.

The mass transfer and pressure drop performance of commercial corrugated packing sheets was investigated significantly in the literature. Random packings, including metal pall rings, Raschig rings and Intalox saddles, were investigated thoroughly for gas-liquid absorption [4]. Packing with mesh structures can deliver excellent phase contacts in gas-liquid applications while keeping the pressure drop low due to the mesh openings. An example of such packing is Dixon rings.

Despite their high surface area, open structure, and thermal and chemical resistance, the Dixon rings packing's hydrodynamic, and mass transfer properties are still missing. Dixon rings offer a larger surface area, which envisages higher mixing capabilities and void percentage, allowing the gas to flow with lower pressure drop. Dixon rings have a complex geometry that hinders some chemical applications, including changes in surface properties through applying a uniformly adhesive coating. Therefore, the research presented in this thesis is focused on coating the Dixon rings and studying hydrodynamics. Simplified hydrodynamics models were developed for Dixon

rings packing to predict the pressure drop and the loading point, as described in Chapter 6. The investigation opens many opportunities for reactive and non-reactive operations for Dixon rings in packed columns [5].

A sol-gel coating method is developed on the Dixon Ring type packing to change the surface properties. Alumina is used as a coating because it is a cheap and well-known catalyst support [6]. The methods used in this study can be placed under the umbrella of parametric studies, that is, the perturbing of certain parameters and investigation into the effect of the change. The manufacturing methods for a sol-gel coating have been researched, replicated, and tweaked until uniform coating on the Dixon Ring has been achieved. The coated rings are characterised using weight change measurements and loading over multiple coatings. Thickness measurements via optical microscopy, adhesive tests, utilising shear forces and ultrasound, adhesive tests under elevated temperature, surface analysis via Scanning electron microscope (SEM), Energy-dispersive X-ray spectroscopy (EDS) and Brunauer, Emmett and Teller (BET). The successfully coated Dixon Rings are then integrated into a gas-liquid mass transfer column. The fluid flow properties around the coated packings are compared with uncoated Dixon Rings and commercial coated column packings.

The improvement of liquid flow inside the packed columns, in terms of relevant flow characteristics such as liquid phase dispersion and wetting efficiency, has been extensively investigated owing to the impacts of these characteristics on process design economically and environmentally [5]. An example of such packing is Dixon rings which is shown in Figure 1.1.

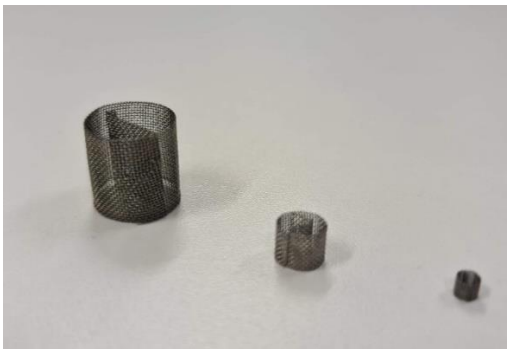

Figure 1.1: Dixon rings packing.

The mesh structure of the Dixon ring offers paths for gas to flow into the ring through the openings of the grids, resulting in a highly effective surface area that is of utmost importance in the catalytic

and gas-liquid separation applications. The gas-liquid operations in packed columns are well-known and have been investigated extensively in the literature, and have been found as an efficient separation method for hydrogen isotopes and many more applications [7]. However, a lack of research is still not sufficiently explored, particularly local events and thus the fluid flow inside packed columns. Therefore, in computational flow models, the effect of various issues influencing the performance of the trickle bed reactors (TBR) can be studied. However, it is essential to set models available from literature related to TBR operations under similar operating conditions to validate and quantify uncertainties and predict flow and inherent mixing [5]. It was required to improve the liquid dispersion by investigating local phenomena of fluid flow and mass transfer inside the gas-liquid packed column, thus increasing its viability in practical applications. The study was conducted using coated, and uncoated Dixon rings and the results from both were compared locally using Computational Fluid Dynamics (CFD) simulations and laboratory experiments.

Identifying the hydraulic capacity in a packed column on a macroscale is needed to calculate the minimum requirement for the column's height and inner diameter. Studies [8] [9] showed that increasing the hydraulic capacity reduces the mass transfer performance due to the flooding phenomena, and packing accompanying lower pressure drops tends to have a higher hydraulic capacity and mass transfer efficiency [10]. Therefore, for application in industry, first, it is necessary to demonstrate and characterise packing performance in terms of hydraulic capacity and then compare them with other commercially available packing media. Thus, parameters such as pressure drop and liquid hold-up are widely investigated in the literature [11]. Gas-liquid absorption is an extensively used application to separate a specific component from a gas stream by absorption into a liquid stream [12]. Experiments are conducted in an absorption pilot plant (Armfield Ltd, UK) to test the hydrodynamics of Dixon rings in a counter-current setup. It aims to extend the application of Dixon ring packing for intensified processes of absorption of carbon dioxide (CO_2) from gas mixtures by fluid flow testing (hydrodynamics), mass transfer testing and packing modelling. The results have been compared to commercial packing to evaluate the hydrodynamics efficiency of Dixon rings. In addition, customized models have been developed for Dixon rings to describe the dry pressure drop and loading points, as described in Chapter 6.

1.2 Overall aim and objectives

This research aims to test and analyse the hydrodynamic performance of the coated and uncoated Dixon rings. Despite several researchers analysing fluid flow for random packing, and the unique physical properties of Dixon rings, there is still no study on the influence of Dixon on the overall packed bed hydrodynamics. This investigation has been conducted on a pore level, and a macroscale of the Dixon rings in gas-liquid columns. It also aims to extend the application of Dixon ring packing for intensified processes of gas and liquid mixtures. First, the Dixon rings were coated using a sol-gel method. Consequently, experiments tested hydrodynamics, and CFD modelling techniques were developed in this research to understand better the effects of non-uniform local flow and mass transfers in a packed column. A critical literature review is provided in Chapter 2.

1.2.1 Sol-gel alumina coating of wire mesh packing

Metallic wire mesh has excellent properties; however, its complex geometry abstains use in many applications, especially where a coating is needed. This part of the thesis focuses on changing its surface properties using a uniform alumina coating. Alumina is selected because it is well-known catalyst support which is used in many applications. This research investigates α-Al2O3 deposition on stainless steel mesh, Dixon rings under controlled coatings. The coating thickness, morphology, and adhesiveness were reported when the starting ratios (i.e., alumina and acid content, mixing and aging time) were changed. The list of objectives is summarised as the following:

1. Achieving a coating that has uniform thickness without blocking the mesh opening;
2. Reaching excellent adhesive properties suitable for harsh environments where turbulence occurs;
3. Having no cracks in the coating;
4. Reporting the detailed method for replicating the coating with low costs.

1.2.2 Tuning the wetting efficiency of wire mesh column: pore-scale flow analysis

After utilising dip coating to deposit the alumina sol-gel, Dixon Rings were able to be coated consistently with a homogenous coating, with wetting efficiency tests conducted using image processing and CFD. The liquid wetting efficiency is defined as the percentage of the wetted area to the total area of the packing**.** The wetting efficiency of the packing is a critical design parameter

as it affects the gas-liquid interface where the chemical process takes place as well as the pattems of flow of multiphase systems. It shapes variations of the liquid flow under various regimes (i.e. droplets, rivulets, channeled or trickle types), directly influencing mass and heat transfer phenomena. The wetting efficiency is entangled by the hysteresis of the liquid distribution over a surface, the operating flow, and the type of packing (i.e. materials and geometries) [13]. Therefore, the local flow around an element of coated and uncoated Dixon rings is visualised by experimental imaging and compared with those obtained by 3D CFD simulation.

1.2.3 Macroscale experiments for hydrodynamics and mass transfer of Dixon rings

It is essential to evaluate and characterize the packing performance and compare them with another commercial packing. The results are validated using existing models of pressure drop and mass transfer. Discussion on process performance in terms of effects of operational parameters such as liquid flowrate and gas flowrate is included. Finally, process model validation is achieved by comparing the results against experimental data obtained in existing models in the literature. This research has tested and analysed the performance of Dixon random packing. It also aims to extend the application of Dixon ring packing for intensified absorption of CO_2 from gas mixtures using liquid in a counter-current operation. The list of objectives is summarised as follows and is shown in Figure 1.2:

1. Fluid flow testing (hydrodynamics)
2. Mass transfer testing

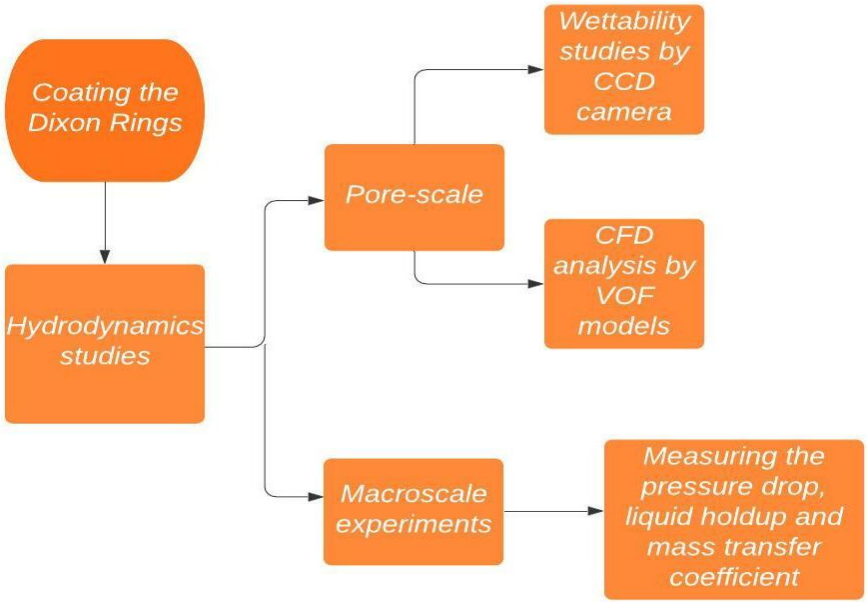

Figure 1.2: Flowchart with the project's aims and objectives

1.3 Methodology

1.3.1 Sol-gel alumina coating of wire mesh

The sol-gel method is implemented to overcome the complex geometry of Dixon rings. This method is based on two main reactions, hydrolysis, and polycondensation. The steps to conducting this part of the study are summarised as follows:

1. Conducting parametric studies on the effect of the starting amounts of the sol-gel (i.e., water to precursor ratio, pH, mixing time, aging time, temperature, and stirring rate);
2. Performing surface characterisation tests via optical microscopy, SEM, EDS and BET;
3. Doing adhesive tests under shear forces, ultrasound, and elevated temperature.

1.3.2 Tuning the wetting efficiency of wire mesh

Various modelling approaches are applied to study the fluid flow for coated and uncoated Dixon rings. CFD tests were conducted using a mesh of 586524 element and a maximum element size of 0.322 mm was found similar to more refined mesh in describing the liquid flow pattern. This 3D transient model was for the laminar flow liquid to illustrate the trickle flow regime over the Dixon

rings. A computer-aided design (CAD) model of the Dixon ring geometry provided by Croft Filters Ltd (Risley, UK);

1. The CAD model is modified to remove the skewed elements occurring due to the wire intersections;
2. The CAD model is then embedded into the commercial CFD package (COMSOL Multiphysics 5.3a);
3. VOF framework for multiphase flow is established using The Laminar Two-Phase Field module on COMSOL Multiphysics 5.3a;
4. A grid independence study is conducted to ensure that the solution is independent of the size of the mesh used in the simulation;
5. Validation of the VOF model via experiments using Charged Couple Device (CCD) camera;
6. The influence of the liquid inlet velocity and the contact angle on the wetting efficiency are investigated through a parametric study relevant to hydrophobic and hydrophilic types of packing surfaces;
7. The liquid hold-up and effective surface area were calculated and validated using models from the literature.

1.3.3 Macroscale experiments for hydrodynamics and mass transfer of complex stainless-steel gauze packing. Physical Absorption using Dixon Ring Random Packing:

The pressure drop and liquid hold have been measured for Dixon rings $^5/_8$ and $^1/_4$ in, for varying flowrate of gas, at 0 l/min (i.e., dry pressure-drop) liquid flowrate, and varying flowrate liquid (i.e., wet pressure-drop).

1. Pressure-drop experiments for Dixon rings $^5/_8$ and $^1/_4$ in;
2. Liquid hold-up tests for Dixon rings $^5/_8$ and $^1/_4$ in.

1.4 Contribution of the thesis

This thesis thoroughly studies the hydrodynamics of random packing Dixon rings. This study was conducted on a microscale and macroscale for gas-liquid phase applications. It also includes

modification of Dixon ring surface with a uniform alumina coating. The wetting efficiency analysis is conducted using CFD modelling and visualised by CCD camera while hydrodynamic parameters such as pressure drop, liquid hold-up, and overall mass transfer coefficient ($K_{G_a}a_v$) were evaluated in a pilot plant. The overall understanding of the flow characteristics for the coated and uncoated Dixon rings can be seen better understood than at the start of this research. Some of the most significant contributions made throughout this research are summarised shown in Figure 1.3:

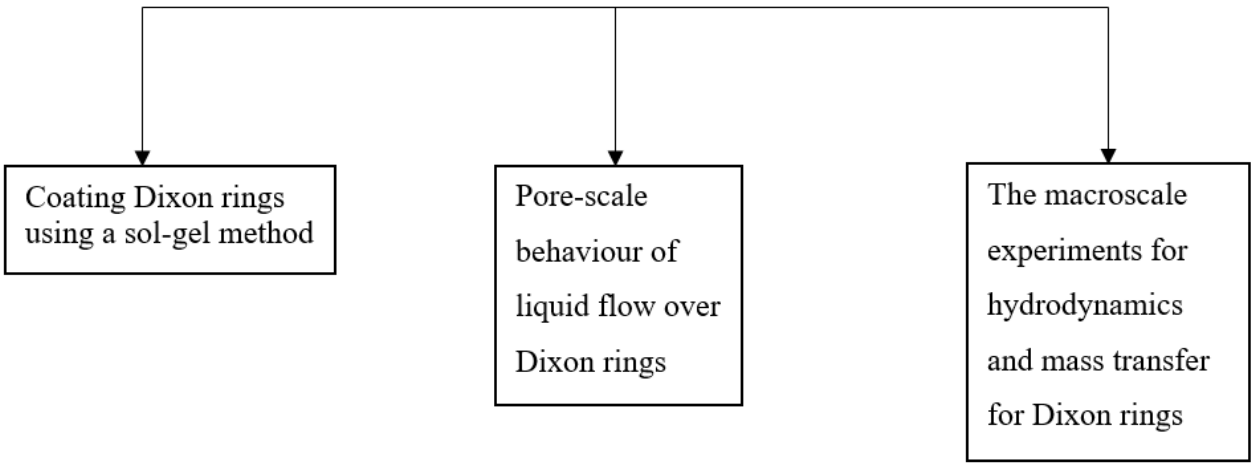

Figure 1.3: The contribution of this research

In this part of the research, the sol-gel deposition method of alumina coating ceramics is investigated for the first time on stainless steel wire mesh using Dixon rings as an example. The kinetics of deposition during the hydrolysis and polycondensation of sol-gel is followed for a range of initial composition of the coating. This included identifying the ratios of Al_2O_3 to water, acid content, polyethyleneimine binder content and the number of deposition cycles to reach a homogenous coating. Well-adhered alumina with a thickness of up to 20 μm was successfully deposited. The molar ratios of acid to alumina and alumina to water, the aging time, the mixing time, and the amount of polyethyleneimine binder are identified. A crack-free coating of controlled thickness alumina on the Dixon rings was produced.

The pore-scale behaviour of liquid flow over wire mesh stainless-steel packing of variable contact angle is relevant for mass and heat exchanges in multiphase chemical systems. Imaging

experiments and 3D VOF modelling investigated this behaviour. The droplet penetrated the mesh of the uncoated Dixon rings before dropping from the bottom section. On the other hand, the droplets are repelled when hitting the surface of the coated Dixon rings.

Hydrodynamic parameters have been investigated extensively for random packing in the literature. They are important to find the best operational conditions and reach the maximum capacity for any given operation. Unfortunately, these tests have been missing for Dixon rings which are a promising packing in terms of fluid mixing ability. The Dixon rings have a higher surface area and void fraction when compared to packing with the same size [3]. The hydrodynamics and mass transfer of a Dixon ring random packing are tested for a range of gas and liquid flowrate. The pressure-drop, liquid hold-up and $K_{G_a}a_v$have been investigated in an Armfield pilot plant.

1.5 Thesis outline

A sol-gel procedure is included in a parametric study on the effect of the starting amount on the coating properties. The gas-liquid flow over coated and uncoated Dixon rings packing is investigated on a pore-scale by CFD modelling and validated using a CCD camera. An experimental investigation on the hydrodynamic experiments such as pressure drop, liquid holdup and the $K_{G_a}a_v$is also included.

Chapter 2 includes a literature review on earlier research in this area. In this chapter, the coating methods used to coat metals are discussed. A review of the methods to characterise the flow in packed columns. It focuses on the wetting efficiency and its importance to characterise the packing. In addition, it deals with the flow on a large scale and hydrodynamic parameters such as pressure drop, liquid hold-up, and mass transfer.

Chapter 3 describes the methodologies that have been used in this thesis. The preparation setup for coating Dixon rings using sol-gel is discussed. Methods to conduct hydrodynamics experiments using a CCD camera and an absorption unit operation are included. The solution procedure of the phase-field model used for the multiphase flow is discussed.

Chapter 4 Includes the sol-gel method used to deposit alumina on Dixon rings. The kinetics of sol-gel reaction is studied through the initial composition of the coating, such as the ratios of

alumina to water, acid content, polyethyleneimine binder content and the number of deposition cycles.

Chapter 5 The liquid flow over uncoated and coated Dixon rings were investigated on a microscopic scale. This behaviour was investigated by imaging experiments and 3D volume-of fluid modelling. The surface of Dixon rings is modified by alumina coating, as described in Chapter 4, to achieve hydrophilic and hydrophobic properties. The results are validated against models in the literature that described the wetting area and liquid hold-up.

Chapter 6 Once the pore-scale level investigations were completed, tests on a larger scale took place. The fluid flow has been characterised in a pilot plant to measure important hydrodynamics parameters such as pressure drop, liquid hold-up, and mass transfer. To ensure the equipment is valid, results from Raschig rings were compared to models in the literature. Then the missing model constants for Dixon rings packing were estimated by the curve fitting method.

Chapter 7 Includes the conclusions of this research. Finally, recommendations for future works have been suggested.

1.6 Supervision, training, and publications

1.6.1 Supervision

1. Weekly based meetings with academic supervisors (Dr. Vesna Najdanovic, Dr. Farid Aiouache).
2. Meetings at the industrial partner premises (February 2018, May 2018, July 2019).

1.6.2 Trainings

1. Three days Bootcamp training at November 2018, part of the Global Eco-innovation (CGE) center to learn about the carbon footprint.
2. Faculty of Engineering Ph.D conference at July 2018, 2019 and 2020 included presentations from different engineering disciplines.
3. Self-training: Solidworks - Comsol Multi-Physics.

1.6.3 Publications

1. M. Abdelraouf, J. Hegarty, A. Rennie, R. Elizalde, N. Burns, Sol-gel alumina coating of wired mesh packing, Ceram. Int. (2020). https://doi.org/10.1016/j.ceramint.2020.05.043.

2. M. Abdelraouf, A. Rennie, N. Burns, L. Geekie, V. Najdanovic-Visak, F. Aiouache, Tuning the wettability of wire mesh column: pore-scale flow analysis, Chem. Eng. J. Adv. 8 (2021) 100181. https://doi.org/10.1016/j.ceja.2021.100181.

1.6.4 Conferences

1. Reactors, Scale-Up, and Separations: Process intensification, integration, and multifunctionality (IChemE). 09/2019 | London, UK.
2. 10th International Conference on Computational Methods and Experiments in Material and Contact Characterisation Multiphase Flow. 05/2019 | Lisbon, Portugal.

2 Chapter 2: Literature review

2.1 Packing

2.1.1 Introduction to packing

Several industrial columns are employed to provide continuous interface contacts, such as packed columns and tray columns [14]. Unlike tray-based columns, packed columns offer continuous interphase contact throughout the column [15]. Packed columns with filter media are commonly used in the chemical industry. Packed columns are filled with regular-shaped particles, which are called packing. Packing are vital to the industry and are used in reaction and separation applications such as catalytic cracking, hydrocracking, trickle-bed reactors, water treatment, and heat transfer operation [16]. The packing material interacts with the fluid through random or structured configurations, involving the solid materials, the void space, and creating pressure drop. Therefore, testing the hydrodynamic performance of packing has been studied exhaustively. The packings enhance the mixing between different phases but are evaluated based on their hydrodynamic performances and flooding points. Therefore, various these packings are available and are fundamentally classified into structured and random packings. The packings can be made of ceramics, metal, plastics or carbon materials. The structured packings are typically corrugated sheets, which are designed to ensure the liquid flows in uniform channels of movement for each phase [17]. They are designed to ensure equal channels for the moving gas phase as well. Compared to the random packing, this structure ensures a more uniform distribution of the two phases over the cross-section of the column. Moreover, the structured packing ensures generally lower pressure drops per mass transfer efficiency, thus is seen as a better choice from the operation point of view

2.1.2 Packing configuration.

2.1.2.1 Structured packing

Structured packings are preferred in gas-liquid applications due to their high mass and heat transfer capabilities. The corrugated sheets offer a uniform distribution of liquid and gas flows, leading to reduced pressure drops along the height of the column. The structured packing can be divided into four types, as shown in Figure 2.1 [18]**.** Panapak, Sulzer Bx and Goodloe are among the earlier generation packing, which resulted in lower pressure drop than the tray columns. The high

manufacturing cost made them not commonly used, and therefore, tray columns were preferred for many applications. The first-generation packing had higher efficiency than the tray columns and therefore was preferred for heat-sensitive applications which occur at lower pressure drops. The rise of metallic sheets made structured packing the preferred in gas-liquid applications due to the low cost of manufacturing. The third and fourth generations of packing manufacturing are generally of simple structure and result in packing, which accompanies low-pressure drop and high mixing capabilities. The geometry of the packing allows the gas to flow smoothly over the surface, thus resulting in less friction and lower pressure drop [2].

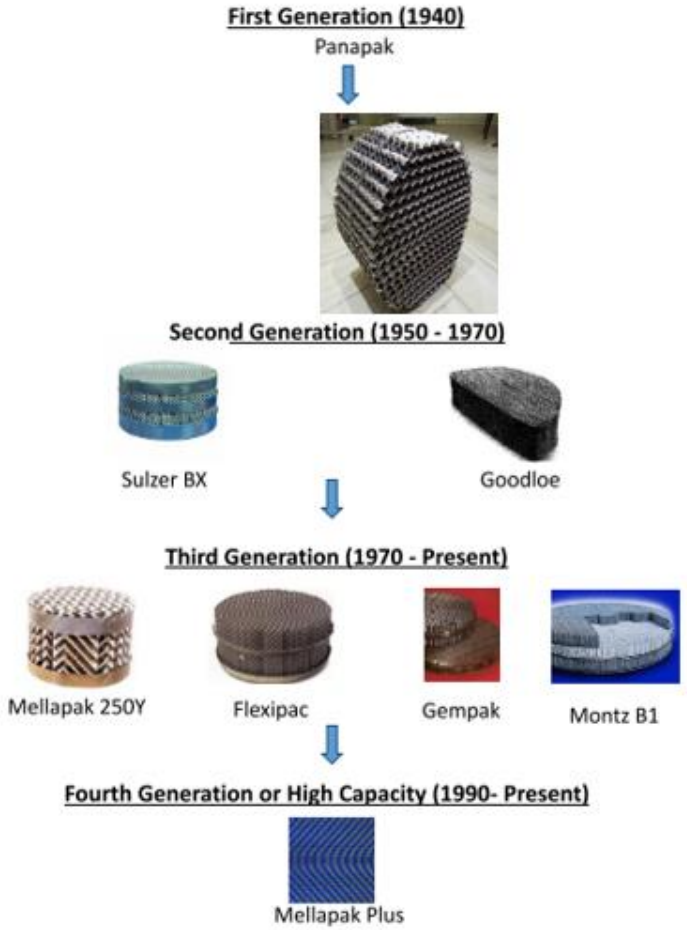

Figure 2.1: The evolution of structured packing from Jammula [19].

2.1.2.2 Random packing

Random packings consist of materials which are randomly dumped into a column in a disordered way. They are divided into saddles, cylinders, and any other shapes randomly distributed in the

column [20]. The advantages of random packings over structured ones include easy production, easy dumping into industrial columns, and effective applications to high liquid loads. The disadvantages include poor distribution of the phases over the cross-section of the column and often high-pressure drop. Since the flow paths are disordered, more turbulence is encouraged. Random packings are favourable compared to structured packings in some industrial applications, especially packing material made of metal, because they are significantly less expensive and more robust than structured packings [15]. Raschig rings and Intalox saddles are the oldest packings developed to fit the mass transfer specification for random packing. These specifications include the packing must form a connected surface and the packing surface and must form uniform lamellas. In addition, the width of the packing lamella should not exceed 5 mm. Pall rings were developed later and were found to follow the mass transfer specification more than other packing. That is because geometry and manufacturing fit the theory of mass transfer for designing random packing. Unfortunately, no patent designs fit the theory of mass transfer. Kolev and Razkazova-Velkova showed that the lamellas less than 5 mm resulted in a complete wetting and the liquid had moved on the surface with low velocity. Later packing that satisfies the mass transfer requirement was produced such as Hiflow rings, Top Pak, and Super Raschig rings, as shown in Figure 2.2. The theory of intensification of packed columns has specific criteria to the packing which are met when the packing allows the gas and liquid to operate at high velocity without the occurrence of flooding. In addition, it should have low-pressure drop and break the liquid film, jets, and droplet, to increase the mass and heat transfers. The packings are compared based on their price, corrosion resistance, pressure drop and their mass transfer efficiency.

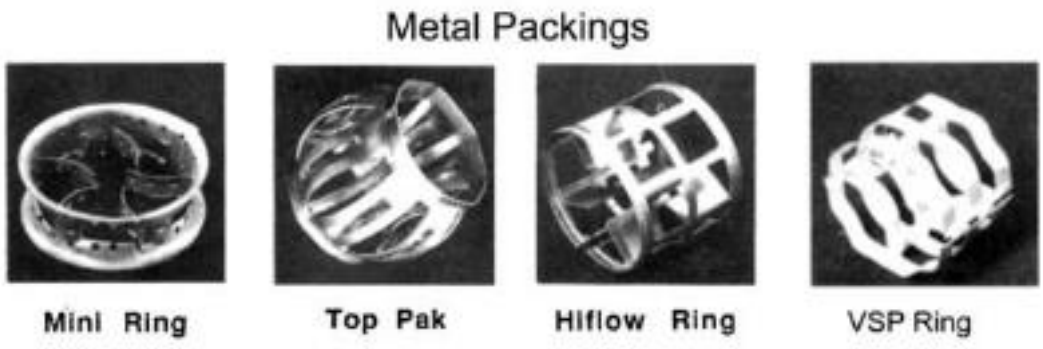

Figure 2.2: Common metallic random packing from Kolev [21].

Metal random packings (e.g. Raschig Rings) are produced commercially and are widely available. Good properties for packing include large surface area, open structure, good liquid distribution across the surface, and uniform gas flow distribution [1]. Since the operating costs are directly affected by the mass transfer processes in the packing, it is critical to find packing material that provides maximum efficiency; hence reducing the overall energy requirements. An example of such packing is Dixon rings. There have been many patented packing since Gay Lussac developed a column packed with coke in 1827, which was the first-ever packed column. Raschig packing originated from the design of the first ring to be used as packing and was patented in 1914. It was first used to produce sulphuric acid [19].

2.1.3 Effect of packing properties on mass transfer and hydrodynamics

The packing geometry affects the hydrodynamics, mass, and heat transfers in packed columns. The packing is usually characterized using its packing diameter (d_p), material, void fraction (ϵ), surface area (a) and the structure of the packing internal, as shown in Table 2.1.

Table 2.1: Physical characteristics of some commercial random packing from Billet and Maćkowia [22].

Packing type	**Material**	d_p **(mm)**	a **(m^2m^{-3})**	ϵ
Raschig ring	Metal	15	378	0.91
Intalox saddles	Plastic	50	114	0.76
Berl Saddle	Ceramic	38	164	0.7
IM Highflow ring	Metal	25	202	0.9
Ralu ring	Plastic	50	95	0.93
Top-Pak	Metal	50	106	0.95

When the pore size was reduced in foam packing, the pressure drop increased [23]. In general, the industry highly desires packing that accompanies low-pressure drop and high mass transfer. Therefore, efforts have been made to produce packing with good hydrodynamics properties such as low pressure drop and high mass transfer coefficient. For example, Super Mini Rings were developed with a curve from the inside, as shown in Figure 2.3. The empty volume/void allows the vapor to flow inside the packing with a low-pressure drop and the arc from inside increase the gas-liquid contact. Xinglei et al. [24] compared the effect of the packing type in CO_2 absorption application using potassium carbonate. They compared the hydrodynamics and mass transfer efficiency for three packings: Mellapak, Super mini rings and Pall Rings. Mellapak are corrgurated structured packing and Pall rings are metallic cylindrical packing It was found that the Super Mini Rings have the highest $K_{G_a}a_v$, 20% higher than MellaPak and 30% more than Pall rings. It can be concluded that the Super Mini Rings can be used to reduce the size of the column. The flooding velocity was investigated for liquid loads above 25 kg m^{-2} s^{-1} for the three packings; Super Mini Rings had the highest gas velocity to reach flooding. This study showed that the design of random packing plays an important role in the efficiency of the operation in packed columns. The geometry of the Super Mini Rings resulted in enhancing the wetting of the packing at the low-pressure drop and reaching high mass transfer. The cost of manufacturing Super Mini Rings is lower than structure packing Mellapak. However, Super Mini Rings had a higher mass transfer rate and lower

pressure drop. It can be concluded that the geometry of random packing can be upgraded and developed to compete with structured packing.

Figure 2.3: Super mini rings from Zhao et al.[24].

2.1.4 Wire mesh packing

There has been development in packing design to achieve a good distribution of gas and liquid while keeping the pressure drop low. Wire-mesh packing is among those that have shown promising applications, facilitated by unique properties. The wire mesh has a porous structure while maintaining a high surface area; thus, it has been extensively used in absorption and distillation applications. The recent design of the packing using 3D printing allows for avoiding the complex procedure of traditional manufacturing methods. In addition, the role of additive manufacturing using 3D printing has allowed altering the geometry without needing extra equipment. Neukaufer et al.[25] designed wire mesh packing using 3D printing through crystal lattice models on computer software. Their packing had a high surface area (422 $m^2.m^{-3}$) and a high void fraction (0.87). The packing's hydrodynamic performance was evaluated using CFD model to estimate parameters such as the pressure drop, the liquid holdup, and the wetting efficiency. The results from the CFD simulations agreed with the results of Billet and Schultes [26] for the dry pressure drop. However, there was a disagreement for the wet pressure drop, and the liquid holdup was high, with a deviation of 30% and 40%, respectively. Bolton et al. [27] developed 3D printed wire mesh packing for CO_2 capture using amine solvents. As shown in Figure 2.4, the packings had nominal cell sizes of 25.4, 12.7, and 6.35 mm, and their effective areas of 280, 564, and 1332 ($m^2.m^{-3}$). The pressure drop experiments were conducted on a dry and wet basis. The pressure drop was slightly overpredicted when capered to Mackowiak [28] model. The 3D printed packing was found to have a lower pressure drop when compared to commercial packing of the same size and material. However, there were major discrepancies between the model and the experiments in the loading region.

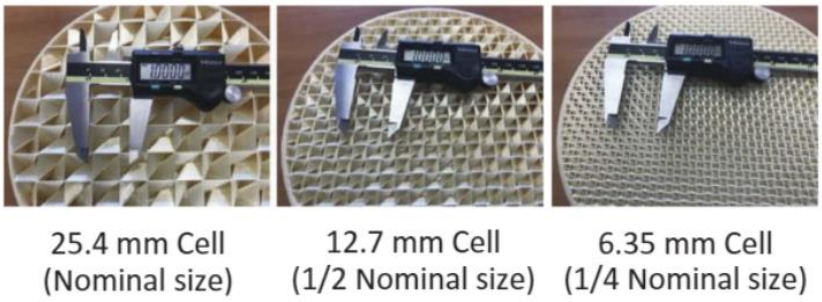

Figure 2.4: Packing produced using 3D printing from Bolton et al.[27].

2.1.5 Dixon rings

The packing in focus for this thesis is the Dixon Ring. This random packing has been around since 1946. However, it has not been sufficiently adopted into widespread due to the manufacturing costs. Dixon rings are a novel random packing, which offers a good mass transfer and a low-pressure drop. Croft-Filters Ltd. in Warrington, UK, manufactures it. It is made of a wire mesh grid of cylindrical shape that is extended to a flat grid along the longitudinal direction of the ring, as shown in Figure 2.5. Dixon rings are preferred for intensified processes. It is made from stainless steel which makes them useable for applications of high temperature such as tritium and water separation. Croft-Filters have developed a new and more economical manufacturing method to produce Dixon rings. Their properties are described in Table 2.2 . Due to its unique geometry, Dixon rings can provide a high-efficiency column when compared to other forms of random column packings. Packing with this geometry is preferred especially when space is limited. Surprisingly, a small number of studies focused on the hydrodynamics for Dixon ring packing [29]. A few studies focus on Dixon rings but are not related to the field of hydrodynamics [30][31]. The area of research is mainly on the chemical absorption of CO_2, which doesn't include any pressure drop studies.

Table 2.2. Dixon rings in structural data.

Size (inch)	**Wire diameter (µm)**	**Mesh (standard)**	**Length of mesh per Dixon ring (mm)**	**Aperture (µm)**
5/8	300	60 × 60	60	718
1/4	160	60 × 60	30	271

Figure 2.5: Stainless steel packing – Dixon ring $^{1}/_{4}$ in diameter

2.2 Coating

2.2.1 Coating metallic substrates

One of the oldest methods of coating is called the Silver plating. It was discovered in the 18th century to provide a cheaper alternative to replace the solid substrate. The method has been used to coat domestic appliances, including the washing of silver cutlery and many kinds of metal house vessels with a thin silver layer [32]. The application of coating metallic substrates has since grown and holds a significant role in several industries [37] nowadays, meeting two characteristics, uniform and adhesive coating layers. The relevance of coating metallic substrates is due to changes in surface physical and chemical properties, which can help with corrosion protection, thermal or optical radiations and reflections [33], and abrasion resistance [34]. The coating is also used in reactive processes to develop e solid catalyst carriers for conventional reactive design or hybrid reactive systems through process intensification strategies [35]. Alternatively, the coating can also be used for tuning the surface of the substrate of column packing internals to reach hydrophobic or hydrophilic properties for applications such as reactive distillation, absorption and adsorption processes. Many materials are being used to manufacture column packings, such as plastic, ceramic, and metal [12]. Ceramic substrates have high thermal resistance and are suited for coating due to adhesive qualities. Therefore, many studies have been focused on coating ceramic packing [36]. However, ceramics cannot be used in applications where high mechanical stress resistance is needed because they are brittle and costly. Metallic substrates can avoid having these problems because they are flexible for manufacturing and have a high mechanical resistance [6]. Truyen *et al.* [6], Masalski *et al.* [37], Sanz *et al.* [38] and Valentini *et al.* [39] investigated the deposition of ceramics on flat metallic substrates.

2.2.1.1 Metallic substrates

Metallic substrates are divided into flat and complex substrates. Foams and wire mesh are examples of three-dimensional metallic substrates with a complex geometry of microchannels, resulting in high surface area and good turbulent flow mixing while keeping the pressure drop relatively low [40]. Due to the complexity and high tortuosity of metallic foams, a turbulent flow is created, which improves the mass and heat transfer properties [41]. Not surprisingly, they have been used extensively in catalytic reactors [42]. In recent years, foams have become more favourable due to the advantages that they gained from their geometry. One disadvantage of the

turbulent flow is that it comes with an increase in the pressure drop. In addition, the manufacturing costs are high for metallic foams. Another option, which combines excellent mass and heat transfer properties, is the metallic wire mesh. The cost of metallic wire-mesh is 25% less than of foams [12]. Metallic weave wire meshes are available in different weave styles and mesh sizes. They are used as filters in the food industry [43], global chemical industry [44] and water treatments [45].

2.2.1.2 Flat substrates

Most of the flat metallic substrates are made of copper, iron, stainless steel or aluminium. The flat metallic substrates have been used in applications such as air conditioning. Xing et al. [46] coated a thin metallic substrate with a zeolite membrane. The coated substrate was tested for air dehumidification. The tests showed an increase of 50% in the dehumidification efficiency when compared to the traditional vapour compression system. M. Valentini et al. [39] deposited alumina by wash coating on a flat metallic substrate for NO_x reduction. They developed a homogenous coating by dip-coating aluminium and FeCrAlloy flat substrates. Overall, flat metallic substrates are not preferred in applications where the flow mixing is not effective due to their low porosity. Therefore, the metallic wire mesh has been used to provide high porosity for applications that require sufficient flow mixing [38].

2.2.1.3 Metallic wire-mesh

The metallic wire meshes are known to hold high porosity and surface area and build on many pores. They have been used in mass and heat transfer applications due to their ductility and rigidity. Their mass and heat-transfer coefficients are significantly higher than the parallel channel monoliths, which are considered among the major developments in packing design over the recent decades due to their high porosity and open structure [38]. The industrial companies that develop the wire mesh packing structures have recurrently reported low pressure. This is due to the pores in the mesh, which encourage the radial mixing of flow, which in turn encourages a uniform distribution of the fluid [5]. Therefore, there have been studies on the implementation of wire meshes for catalytic applications [47]. Wire mesh coated with catalysts is also used to produce nitric acid and formaldehyde [48]. It was shown that the catalytic performance of the wire mesh was higher than of conventional ceramic honeycomb catalyst due to the existence of the pore structure of the mesh. [41].

Coating metallic wire mesh is challenging due to its complex geometry thus, a novel coating method is required. In order to coat metallic wire mesh, it is important to plan the deposition of the coating material over the metal wire. The thermal expansion of the metallic mesh is usually different from the coating applied to its surface, which might hinder the efficiency of adherence of the coating. Methods for coating wire mesh include chemical vapour deposition (CVD) [47], physical vapor deposition (PVD) [49], plasma sputtering [50], electrophoretic deposition (EPD), spray coating, sol-gel and wash-coating [8,9].

2.2.2 Manufacturing of metallic wire mesh

The metallic wire meshes are typically originated from the sheets of the wired screens. A recent technique by T. Hwang et al. [52], who manufactured metallic packing, used the selective laser melting technique for stainless steel powder. A copper holder was used to conduct the layering of AISI 304 stainless steel powder due to its high thermal conductivity. The copper holder prevented the melted laser layer from getting attached and provided excellent heat transfer efficiency. The process parameters such as the laser temperature and powder thickness were evaluated to achieve a high-quality wire mesh in a single step.

Overall, however, the simple and cheap method to manufacture wire mesh packing is reported by John and Rehberg et al. [53], which used 60x60 and 80x80 mesh,. The fabrication method did require welding or grinding and each packing element was produced separately. The mesh sheet was placed in a Pyrex pipe and expanded under stress with the walls of the tube to reach the circular shapes. The mesh was made of stainless steel and bronze. The Pyrex pipe was selected due to its ability to handle the high stress of the metal. The metal was kept in firm contact with the walls due to its elasticity. A circular disk of the mesh was cut using a punch press. A circular shape was cut from the edge of the disk to a specific depth to create the packing and the cutting depth that determined the voids of the packing, as shown in Figure 2.6.

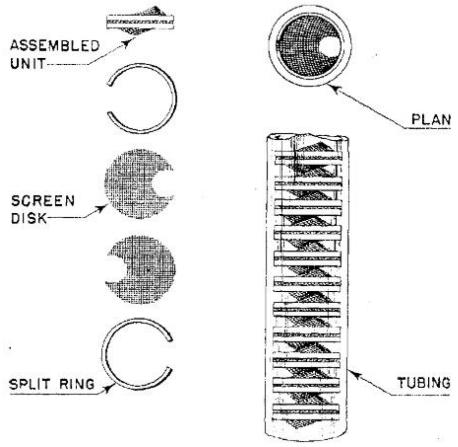

Figure 2.6: The manufacturing method of wire mesh packing from John and Rehberg [53].

2.2.3 Coating methods

Coating metallic wire mesh is a challenging procedure due to the complex geometry of the structure, and thus innovative coating methods remain required. To coat metallic wire mesh, planning the deposition of the coating material over the metal wire is critical. The thermal expansion of the metallic mesh is usually different from the coating applied to its surface, which might hinder the efficiency of adherence of the coating. Methods for coating wire mesh include chemical vapour deposition (CVD) [47], physical vapor deposition (PVD) [49], plasma sputtering [50], electrophoretic deposition (EPD), spray coating, sol-gel and wash-coating [8,9]. Some of these methods require expensive types of machinery, such as CVD. The CVD-based techniques are conducted under vacuum, and the precursor molecules break under high temperatures. Therefore, precursors are kept in a chamber under high temperature to help break the molecules to the desired coating on the surface [45].

These methods are required to produce films ranging from 5 nm to 100 nm. F. Zhang et al. [54] and F. Zhang et al. [45] developed a nano-sized layer of hexamethyldisilazane (HMDS) and SiO_2 on copper wire mesh by CVD. The coating was used to introduce superhydrophobic and superoleophilic wire mesh, which can be used for oil/water separation. The wire mesh surface was modified using HMDS to achieve a high separation efficiency. They concluded that the SiO_2 mesh is a cheap separator used in everyday life to separate oil from wastewater. M. Dvorakovaa et al. [55] developed cobalt oxide (Co_3O_4) catalysts on stainless steel wire mesh. They preferred stainless steel mesh due to its flexibility, making it easy to install in the reactor. It also ensures

maintaining a low-pressure drop and good heat transfer. They combined PVD and EPD methods to deposit thin films of coating. The samples were tested for the oxidation of ethanol. The samples with the highest catalyst loading were obtained by EPD and had the highest efficiency. However, this coating had poor adhesion that was improved by a thin layer of Co_3O_4 from the PVD. These methods are preferred when scale-up is not required due to the slow production. Each substrate is coated individually to ensure the precision of the operation.

EPD is carried out using dispersed or suspended particles in a liquid medium. It is based on the deposition of particles from the liquid phase by passing an electrical current. The EPD efficiency depends on the suspension properties like the powder sizes, dielectric constant, binders, and zeta potential. Also, parameters associated with the process like the operating voltage, the distance between the two electrodes, and depositions time are important to control the film thickness and homogeneity [56] [57]. The EPD is a well-known technique used extensively to coat metallic substrates using alumina layers. Yang et al. [52] coated woven stainless-steel mesh using aluminium powder.

Sun et al. [58] deposited γ −alumina powders on stainless steel wire meshes. They discovered that the coating loading of the wire mesh was affected by the zeta potential and the amount of binder in the suspension. The coating adhesion was increased by increasing calcination temperature to 500°C and by adding aluminium particles. Vorob'eva et al. [59] used EPD for alumina sol-gel coating. [58] The coating thickness was around 50 μm, which could be changed using the starting amounts. The surface area was 450 m^2/g when measured using BET.

Wash-coating is one of the most known coating methods to deposit metal oxides. It produces a layer by dipping the substrates into the slurry containing the desired coating material. The dipping is usually followed by drying, peptization, and calcination of the substrate. Meille *et al.* [42] showed that reproducing coating by combining several milling steps of coarse powders and wash-coating was not straightforward in achieving good surface adhesiveness. However, wash-coating methods have some disadvantages: poor adherence and the non-uniformity of the coating. The coating might not survive environments where mechanical stress is applied to them. A few studies reported coating adherence to wire-meshes using other coating methods. A combined method of spray coating and electrophoretic deposition has been used to coat wire mesh with alumina. The EPD was used to increase the surface roughness of the wire mesh to increase the adhesiveness of

the coating. The current coating methods of metallic substrates remain onerous, particularly when they are intended to be used for applications at an industrial scale under controlled surface properties [11]. Sol-gel has been investigated by Guglielmi [60], Truyen *et al.* [6], Masalski *et al.* [37], Sanz *et al.* [38] and Valentini *et al.* [39]. The sol-gel process is cheap, simple, and easy to implement due to the amount of equipment needed.

2.2.4 Sol-gel

2.2.4.1 Definition

The history of the sol-gel goes back to the 19th century when $SiCl_4$ produced a gel when it was exposed to air [61]. The gel was formed because of the hydrolysis of the moisture in the air with $SiCl_4$. Inorganic materials such as metal oxides and carbide serve a key role in the industry. They are used in manufacturing biosensors, optical devices, and catalysts and can be used for various protections. Initially, they were prepared by mixing powders of the reactants at high temperatures to achieve the required compounds [61]. The main disadvantages of mixing powders are inhomogeneity and conversion, which are limited to mass transfer rates. The large particle size of the powder blocks the diffusion of the reactants. Therefore, many areas remain unreacted and go to waste [62]. Methods to reduce the size of the powder became popular such as ball milling which increases the surface area. Unsurprisingly, sol-gel and coprecipitation were developed to replace the solid-state chemistry methods. Sol-gel has been used for 40 years to prepare glasses, ceramics and coating at lower temperatures. Such methods avoid the high-temperature operation, which takes place as part of the solid-state reactions. The sol-gel coating provides excellent adhesion using strong bonds between the coating and substrate [63].

The Sol-gel can produce solid material by ensuring an atomic scale mixing of the reactant. It overcomes the randomness of the solution by using homogeneous precursors. Therefore, complex compounds can be achieved at low temperatures. The sol-gel controls particle size, morphology, and phase segregation [61]. The sol-gel process is well-known for coating glass and ceramics used in manufacturing optical devices, chemical sensors, and more. The Sol-gel is a powderless technology which is based on wet chemistry and involves several reactions. It includes a precursor mixed with other materials to produce organic and inorganic compounds [64].

Several precursors, such as chlorides and metal alkoxides (i.e., aluminium, titanium, and caesium) are used in the sol-gel preparation [50]. The metal chlorides produce metal alkoxide by a reaction

with an alcohol. Ammonia is usually added to react with the undesired HCl formed in the reaction with alcohol. Metal alkoxides ($M(OR)_x$) are usually synthesized by the addition of an alcohol to a metal chloride and a metal cation replaces ROH. Metal alkoxides usually act as Lewis acid due to their high coordination expansion [65]. The coordination expansion shows how rapidly a molecule reacts and is defined as the difference between the coordination number and valence number. Therefore, metal alkoxides have high sensitivity to the presence of water and they form metal hydroxides. Hydroxyl ligand compounds such as ($(RO)_{x-1}M-OH$) are formed due to the presence of water. The ligand exchange products are usually related to the type of metal to water ratio, pH, type of metal and operating temperature.

Sol–gel process can be summarized as the preparation of inorganic polymers/ceramics from liquid precursors to form a liquid solution which solidifies to make a 'gel'. Hydrolysis and condensation of the precursors form the sol, which is a colloidal suspension [66]. The sol-gel procedure is typically carried out by acid hydrolysis and polycondensation of diluted metal alkoxide (i.e. isopropoxide, butoxide) [3]. The resulting colloidal particles reach specific surface energy of adsorption tendency that could alleviate metal complex geometries. The hydrolysis of alkoxides ($M(OR)_x$) produces metal hydroxyl bonds ($M-OH$), as part of hydroxyl lingand compounds ($(RO)_{x-1}M-OH$), by a nucleophilic substitution mechanism, as described by equation (2.1) [65]. This reaction is identical to Lewis base attacking a Lewis acid, and proton transfers from the H_2O molecules to ($M(OR)_x$), leaving the molecule in a transition state until the alcohol is released [58].

$$-M-(OR_x)+H_2O \leftrightarrow (OR_x)-M-OH+ROH \qquad (2.1)$$

The condensation is also a nucleophilic attack that follows hydrolysis and is described by equation (2.2). A lone pair of oxygen molecules of the metal hydroxide $(RO)_{x-1}M-OH$ attacks the partially positive metal (M), leaving the hydroxide of the metal in a transition state, $(RO)_{x-1}M-OH$ molecules linked together or with $M(OR)_x$, and producing $(RO)_{x-1}\ M-O-M\ (RO)_{x-1}$. These are the metal and oxygen bridges which are responsible for forming 3D networks [67].

$$(OR_{x-1})-M-OH+(OR_{x-1})-M-OH \leftrightarrow (OR_{x-1})-M-O-M-(OR_{x-1})+H_2O \qquad (2.2)$$

Several precursors can be used to synthesize the sol-gel, including metal alkoxide precursors. After the sol, the gel is formed, which might have several structures based on the experimental

procedure. Several gels are reported in the literature, such as covalent polymer networks, ordered gel, and disordered gel [68].

2.2.4.2 Process parameters

If the hydrolysis or the condensation reaction is not carried out as desired, metal oxide and hydroxide precipitation could occur. The reactions aim to obtain oligomers that have good solubility in the solvent. The factors affecting the efficiency of the hydrolysis and condensation reaction are the type of precursor, molar ratio of precursor to water, pH, mixing time and aging. [69]

2.2.4.2.1 Water/alkoxide ratio

The type and concentration of the precursor are considered important parameters that affect the quality of the sol-gel. The type of the alkyl group in the precursor affects the hydrolysis reaction. The length of the alkyl chain affects the solubility and bonding occurring with water molecules [61]. The water amount in the sol-gel formation is another important parameter that should be considered. A low water ratio causes a reduction of the particle size while increasing the water content increases the particle size [70]. If the water amount is low, hydrolysis reaction occurs much slower than condensation. The excess metal alkoxide in the water will form big particles of M-O-M groups. If the right water to precursor ratio is used, the hydrolysis reaction is completed, and big particles are formed. Fahrenholtz et al. [71] prepared silica sol-gel using tetraethylorthosilicate (TEOS) and methyltriethoxysilane (MTEOS). When the TEOS molar ratio was more than 0.5, the surface area and the pore volume were reduced.

The partial charge of the atom, the coordination number, and the molecular structure of the metal alkoxide reflect how fast the reactions progress. An acid or a base catalyst is usually added to accelerate the reaction rate, which is measured by the coordinative unsaturation, which in turn is the difference between the valence number and the coordination number of the metal [65].

2.2.4.2.2 Aging

Aging is a crucial step in the success of a sol-gel process. During the aging, sol networks grow, and the viscosity of the sol increases. Aging is usually carried out in an open flask allowing alcohol to evaporate and the water amount to reach the same amount under ambient conditions. The viscosity of the sol increases because the condensation reaction keeps taking place and produces sol monomers with low concentration and strong molecular interactions [33]. The aging step is

carried out at a normal temperature and can be extended from a few hours to several weeks. The sol-gel aging is highly affected by the flask's time, temperature and size. Each parameter of these conditions can alter the viscosity of the sol and the gelation. Sakka et al. [61] showed that temperature change could profoundly influence gel viscosity. They have adjusted the temperature to reach a drawing range of viscosity for several hours with an increase of 4 % per hour. The gels obtained for fiberazation were crack-free.

Studying the effect of aging is challenging because it requires *in situ* method and other imaging observation techniques at a nanoscale. Nuclear magnetic resonance (NMR) technique-based methods can be used to study the aging effects on sol-gel by measuring pore size by using relaxation measurements. The spin-lattice is measured and then the relaxation time is related to pore size. It was concluded that the pore size is directly affected by temperature, pH and aging time. D A. Ward and E I. Ko [72] prepared thin films of zinc oxide (ZnO) and investigated the optical properties. They showed that the optical properties of the gel improved with a prolonged aging of 24 hours. The sol aged in ethanol and KOH mixture had higher surface area that the sol aged in ethanol only.

2.2.4.2.3 pH

The addition of acid is a crucial step in manufacturing the sol-gel coating. When the addition of acid takes place, the acid does not participate in the sol-gel reaction but acts like catalyst, which affects the hydrolysis reaction rate. The addition of acid affects the oxidation activity of the corresponding anions. The pH value influences the zeta potential of the sol after adding a certain amount of acid; the zeta potential is shifted to the neutral region known as the isoelectric point. The zeta potential is used to measure the activity and stability of the sol. Moreover, the stability of the sol is related to the attraction and repulsive forces [73]. If the electrostatic or repulsive forces are low compared to Van der Walls forces, particles tend to coagulate. During the deposition process, particles will also coagulate if the attraction forces are much higher than the repulsive forces. [20] A stable sol is formed when the zeta potential is shifted from the isoelectric point. The formation of large agglomerates occurs at low zeta potential values. The addition of the acid is known as “peptization” which produces smaller particles in the sol, it is important for a controlled coating. [74]

2.2.4.2.4 Mixing time

The mixing time of the reactants in the sol-gel reactor has an impact on the hydrolysis and condensation reactions [70]. The hydrolysis and condensation occur rapidly before a complete mixing is achieved. The effect of mixing time can be observed when the reactor molecules should be mixed faster than the reaction rate. The mixing time will directly affect the particle characteristics. The design of some reactors includes a mixing element such as a rotating disk reactor and stirrer tanks. It is crucial to determine the mixing time, especially in the industry, to avoid the extra operating cost and to reach high-quality coating [66].

2.2.4.2.5 Temperature

The operating temperature influences the rate of the hydrolysis and condensation reactions and thus the characteristics of the sol. The temperature affects the rate at which the solvent evaporates and the concentration of the particles in the sol. Controlling the evaporation rate is important as it affects the quality of the sol-gel and, in turn, controls the agglomeration of the particles. If evaporation occurs rapidly, the obtained gel will have many cracks and will not be homogenous. B. Yoldas [75] is the first to manufacture thin alumina coating using the sol-gel method. He showed that if cold water is used for hydrolysis and condensation reactions, the resulting sol will contain amorphous monohydroxide. On the other hand, the hydroxide is converted to crystalline boehmite when the reaction iss conducted at 80°C.

2.2.4.2.6 Calcination temperature

Calcination, as a final step, is considered crucial in the sol-gel process. During calcination, the solvent is removed at a certain rate, enabling the particles to agglomerate and crystallise [76]. The calcination temperature has an effect on the crystal structure and the surface area of the coating. In addition, the calcination temperature has an effect on the adhesive properties. Giani et al. [77] studied the effect of calcination of alumina on metallic substrates using XRD analysis. They showed when the calcination temperature was at 700°C, a small number of alumina particles appeared on the surface. When the calcination temperature was increased to 900°C, desert rose alumina was formed, which had better adhesive properties. When the temperature was increased to 1000°C, bigger agglomerates were formed, which led to cracks. The occurrence of micropores during calcination leads to the formation of capillary stress thus cracks develop. The micropores are usually eliminated by adding a binder or by supercritical drying. Sarwani et al. [78] showed that alumina and nickel coating surface roughness increases with the calcination temperature for

steam reforming. The surface roughness increased from 55 to 274 nm for calcination temperature from300 to 600°C. XRD tests showed that more alumina and nickel particles are formed at 600°C. In addition, 600°C resulted in the highest conversion for steam reforming. S. Adegbite [79] studied the effect of calcination on the adhesive properties of alumina on FeCr substrates. When ultrasonic adhesive tests were conducted, the weight losses were 1.5%, 0.8% and 0.08% for the calcination temperatures 400, 700 and 900°C, respectively.

2.2.4.2.7 Dipping velocity

The withdrawal velocity is a crucial factor in the dip-coating process as it controls the thickness of the coating. The draining and entraining forces occur when a substrate is withdrawn from a coating bath. The difference between these two forces determines the coating thickness. [46] Faustini et al. [71] discovered two flow regimes are present during the dipping process. They showed that at low dipping speed, the thickness of the coating is controlled by the rate of evaporation of any excess alcohol and the capillary forces. On the other hand, the viscous drag forces control the coating thickness at a high dipping speed. Suppose the dipping velocity is in between all the previous factors intertwin. Usually, the dipping bath contains a highly diluted solution to maintain the homogeneity of the coating. Several dipping cycles are used to increase the thickness of the coating. Low dipping speeds are also used to increase the thickness of the coating. More capillary forces appear when the dipping speed is low.

2.2.4.3 Preparation method

The sol-gel preparation consists of some fundamental steps to achieve a uniform coating using the sol-gel dipping method. First, the substrate is pre-treated and cleaned from dirt, and the precursor is hydrolyzed in excess water under vigorous stirring to minimize the mass transfer limitations. Then acid is added dropwise for the peptization of the hydroxide. Once the mixing is completed, the substrates are constantly withdrawn in the coating bath. The coated samples are dried in air for a few hours and calcinated to achieve good adhesive properties. [61]

Lee et al. [80] prepared alumina coating on stainless steel substrates by sol-gel and dip-coating methods. As shown in Figure 2.7, the substrates were cleaned by a vapour degreaser. Aluminum alkoxide or aluminum secondary butoxide were mixed with excess water, allowing hydrolysis and condensation reactions. Acid was added with a molar ratio of 0.07 mole acid per mole of alkoxide. The sol was allowed to increase by aging the sol for 24 h and the substrates were dipped at a

constant speed of 15 cm/min in the coating bath, then dried at 95°C for 1 hr. The final step was the calcination at 500°C for 3 h until transparent alumina films were obtained.

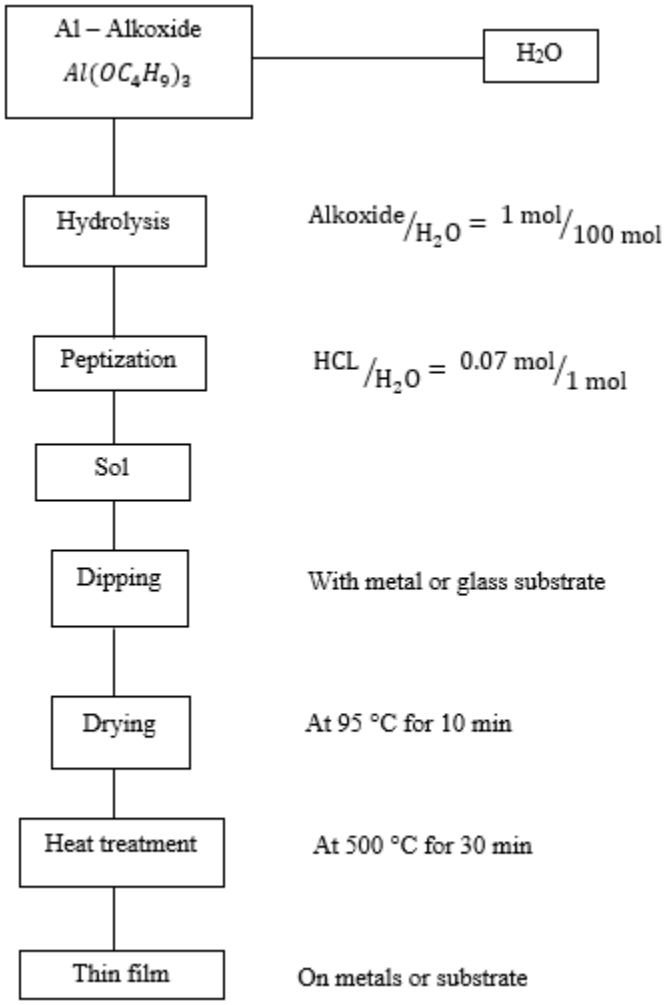

Figure 2.7: Sol-gel coatings preparation diagram from Lee et al.[80].

Hosseini et al. [81] used a sol-gel method to prepare hydroxyapatite powders. First, water was added with a low flow rate of 6ml/min to a 4 molar solution of Triethyl phosphate (TEP) ($(C_2H_5)_3PO_4$), which was mixed with excess water, as shown in Figure 2.8. Then three molar $Ca(NO_3)_2 \cdot 4H_2O$ was mixed with water and added to the TEP solution. The mixture was stirred vigorously for 24 h. The mixed sol solution was continuously agitated for 60 min at 80°C. The sol was dried at 95°C for 1 hr and then calcinated at 600°C for 3 h. The sol was aged up to 24 h, and the viscosity measurements were conducted.

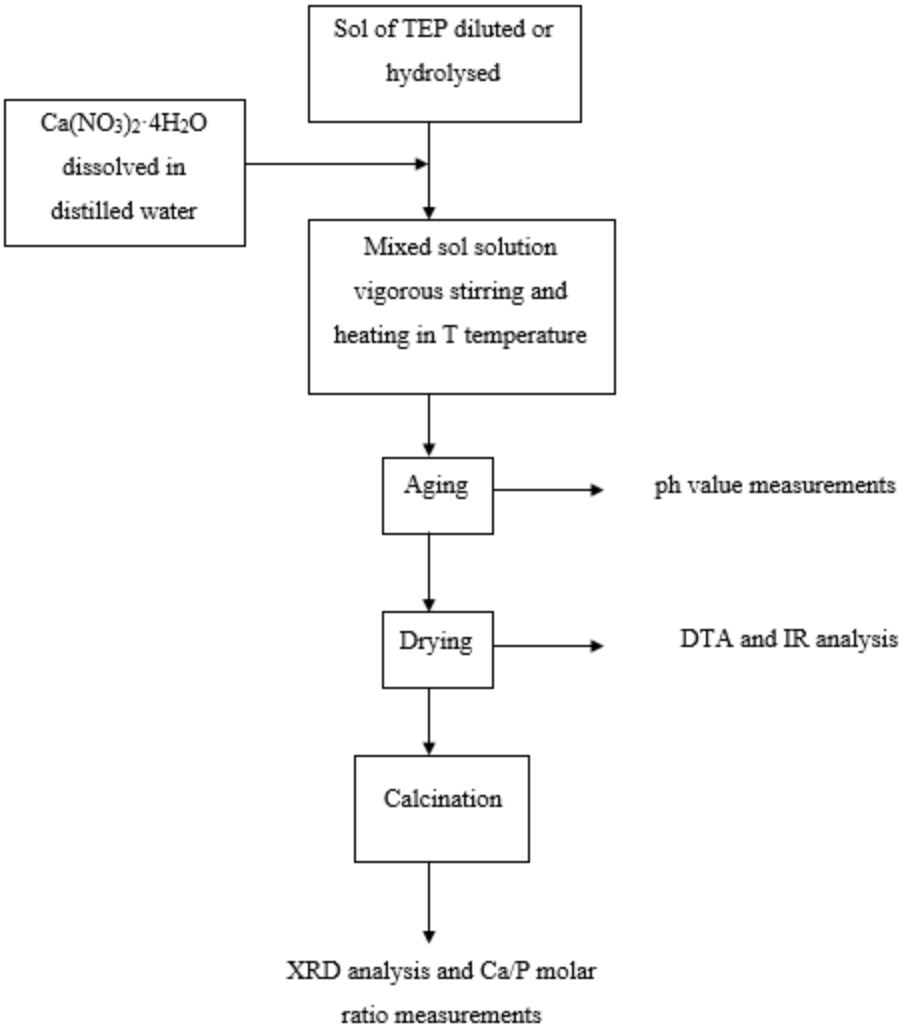

Figure 2.8:Sol-gel coating preparation steps from E.Hosseini et al.[81].

2.2.5 Characterization methods

2.2.5.1 Microscopy and surface analysis

Several methods are used to characterise the efficiency of the sol-gel coating, including microscopy, surface analysis tests, and adhesive tests [82]. The microscopic methods include the optical microscope, SEM, and Transmission electron microscopes (TEM). Surface analysis methods such as EDS, BET, and X-ray diffraction (XRD) give a detailed analysis of the coating composition, surface area, and crystal structure [83]. Microscopy methods give an overall picture of the coating but do not provide quantitative results about the surface composition [84]. The optical microscope is not precise equipment to visualize the coating because the resolution limits

the wavelength of visible light. SEM uses a beam of electrons instead of light beams. The electrons hit the sample where the absorption of electrons occurs. Then the beams of electrons are converted to a high-quality image. The EDS is another tool which works by electron beam scattering. The EDS can be used independently or in parallel with the SEM [85]. When the electrons hit the target atom, an X-ray is emitted from the surface, and the element can be identified from the emitted X-ray energy.

The surface composition is calculated [86]. The BET technique measures the surface area by the physical absorption of gas molecules on the surface. The BET relates the number of absorbed gas molecules on the material surface to the effective surface area. Usually, nitrogen (N_2) is used to conduct the BET analysis. Therefore, most of the BET tests are conducted at 77 K, the boiling point of N_2. Ran et al. [86] used a BET surface analyzer (Coulter 100CX, USA) to measure the surface area of catalysts obtained by sol-gel. The samples were first desorbed under vacuum for 2 h and were dried at 100 C for 1 h. They have used N_2 to calculate the surface area, therefore the measurements were conducted at 77 K. The morphology of the coating was determined using SEM (JEM-5600LV) accompanied by an EDS (Oxford ISIS-300) to determine the surface composition.

2.2.5.2 Adhesive tests

Coatings must have good adhesive properties in applications conducted at elevated temperatures and high operational flow rates. Therefore, adhesive tests are key in determining the efficiency of the coating. The coating quality is assessed based on the amount of weight loss during this test. Small weight loss would indicate that the coating has good adhesive properties and vice versa is also true. Several tests are used to determine the adhesive properties of the coating on metallic substrates, such as shear forces, scratch tests, ultrasonic tests, and thermal tests. Shear forces tests are simple; the coated substrate is dipped in water and subjected to mechanical stirring to test the adhesiveness of the coating. The substrate is placed in a beaker on a stirring plate and stirred for a certain time and stirring rate, measured by the rotations per minute (rpm). The stirring rate is typically set to 750 rpm to create turbulence. The shear forces are increased when the magnet stirrer hits the substrate during the test. In the ultrasonic test, the coated substrate is dipped inside a liquid, and sound waves create strong vibration forces. Vasconcelos et al. [74] used RS Pro 100W ultrasonic bath for 5 mins for sol-gel silica coating at 100 watts. The tested samples were dried using nitrogen and weighted to measure the weight loss percentage. Oxidation resistance tests of

the coated substrates are conducted at high temperatures in a furnace. Figueira et al. [34] described a simple heat test for corrosion protection systems. They placed the coated samples in a tube furnace at 800°C for1 h with ramp of 5°C per minute, and the weight changes were recorded.

2.2.6 Pre-treatment

The adhesiveness of the coating and metallic substrates represents the biggest obstacle for all coating methods [87]. For a sol-gel process, it is dependent on parameters such as type of precursor, operation temperature, viscosity of the sol, etc. One way to improve the adhesiveness is to apply treatments to the substrate before the deposition of any material on the surface [68]. The treatment aims to remove any dirt or contamination and to create a rough surface. The roughness is a property which quantifies the surface is evaluated by measuring the difference between the normal vector of the actual and the ideal surface. When the difference between the actual and the ideal surfaces are large, the surface is considered rough [88]. The surface roughness is usually measured with Atomic force microscopy (AFM) and SEM [82]. Degreasing removes any dirt or impurities that block the formation of bonds between the sol and substrate surface, reducing the substrate's available surface area. In addition, it increases the coating load by making more areas available for bonds between the substrate and the coating [89]. Roughening of the surface increases the tendency of adhesion between the substrate and coating by changing the wetting efficiency, contact angle, and the surface energy of the substrate. Chemical bonds are highly required to achieve excellent adhesiveness properties. Heat treatment methods of metals such stainless steel develop passive layers of chromium oxide (Cr_2O_3) [78]. The heat treatment oxide the substrate's surface, creating oxide whiskers. These whiskers increase the surface area available for the coating and motivate covalent bonds to occur.

Pre-treatments were considered and evaluated in previous studies conducted on metallic wire mesh. Beibei et al. [90] degreased the wire mesh from impurities and dirt by dipping it in acetone in an ultrasonic bath for 30 mins. This step was followed by drying the substrate at 100°C to remove excess moisture. Another study by Vasconcelos et al. [74] used several pre-treatment methods on a stainless-steel substrate for alumina coating via sol-gel. First, the substrate was ground with sandpaper and then dipped in acetone. Galliano et al. [91] used electropolished stainless-steel to achieve a cleaner and smoother surface. One disadvantage of this method is that it reduces the wetting efficiency of the substrate, thus the adhesion. They also conducted a heat

treatment at 350^{o}C to develop oxide whiskers to improve the adhesiveness and the coating load. Finally, the substrates were rinsed with ethanol for further cleaning. Valentini et al. [39] used hydrochloric acid to increase the roughness of FeCrAlloy substrates.

There are other methods for the pre-treatment of a substrate, such as acid pickling and degreasing via vapour deposition. However, no optimal pre-treatment method works for all cases to reach the maximum coating efficiency. The effectiveness of each pre-treatment method is relevant to the preparation method of the sol-gel. Therefore, it is critical to investigate the effect of several pre-treatment methods.

2.2.7 Dip-coating

Once the sol-gel is prepared, the coating can be applied using dip coating, spin coating or spray coating. Spin coating is carried out by adding the sol on the substrate, then spinning the substrate at high RPM to remove the excess liquid and a thin film remains. On the other hand, the spray coating is conducted by having the coating as an aerosol, allowing a thin film coating [92]. The dip coating is a simple and affordable process used to coat substrates and is easy to scale up. It can be used for any substrate, even with complex geometry such as the wire mesh. This process includes dipping, dwelling, withdrawing, and drying [93]. The substrates are immersed into the sol at a specific speed before being withdrawn at the same speed. This procedure is usually carried out using a dip coating machine. In this process, the coating bath (i.e. sol) must remain in the liquid phase, allowing a homogenous dispersion of the particles of the desired coating[94]. Early gelation in the coating bath makes regions to have higher concentrations, this phenomenon deteriorates the uniformity of the coating and results in crack formation. The wetting efficiency of the coating depends on the contact angle and the sol viscosity. This is followed by particle aggregation by drying to remove excess solvent and only leaving a thin film on the substrate. This develops stronger bonds between the coating particles and the substrate [95].

2.2.8 Coating of metallic substrates

A study by Guglielmi [60] reviewed the values of metal coating via sol-gel techniques. The sol-gel method, which manufactures high purity thin films at moderate temperature, is waste-free and eliminates the use of coarse powders, favouring the potential for coating complex geometries. The method is recurrently cited as promising to produce cost-effective coatings of a controlled thickness by judicious use of composition of the liquid precursors, facilitating the scale-up to

industrially relevant applications. Sol-gel methods are known for developing cracks inside the thick coating, particularly in complex geometries of the substrate [13]. Truyen *et al.* [6], Masalski *et al.* [37], Sanz *et al.* [38] and Valentini *et al.* [39] investigated the deposition of γ-Al_2O_3 by sol-gel on flat metallic substrates. They prepared the sol-gel by following Yoldas' method [75] with various adjustments (i.e. starting composition and operating conditions of temperature and pressure). The method consisted of mixing aluminium alkoxide (isopropoxide or tri-sec-butoxide) with an excess of water at approximately 80-85°C under vigorous stirring. The sol was clarified using a peptization process by adding an acid, which reduced the level of heterogeneity by breaking the large particles for better control of the hydrolysis kinetics.

The coating was characterised by thickness gauge, surface morphology analysis, ultrasonic adherence, thermal resistance, rheological and porosity distribution tests. Truyen *et al.* [6] allowed the sol to age until thixotropic properties began to emerge, which was the key step to develop a thin and uniformly spread coating of 0.1-10 μm thickness. Valentini *et al.* [18] investigated the effect of the acid and water content on sol viscosity. They reported a range of optimal compositions for a uniformly spread coating of an approximate thickness of 30 μm. Alumina powder was recommended to be added to the sol using multiple depositions of diluted solutions to achieve a controlled adhesiveness. Unlike the samples with low loads (i.e. 1 or 2 deposition cycles) which demonstrated almost no mass loss under ultrasound tests, those of large loads (i.e. 3 or 4 deposition cycles) demonstrated mass losses of over 70%. Guglielmi [60] reported similar results, who emphasized that the coating above a certain thickness would exhibit poor protective capabilities owing to the development of cracks and malformations in the coating structure. Sanz *et al.* [38] investigated a method of coating metallic wire-mesh for the catalytic combustion of soot by varying acid concentration, water content, solid content and polyvinyl alcohol (PVA) as a polymeric binder. The role of the PVA was pertinent to reduce the cracks and improve the adhesiveness of the metallic substrates. Giani *et al.* [35] achieved a 20 μm layer of alumina coating on metallic foams. The role of viscosity of the gel was investigated through rheological tests by varying the sol-gel parameters such as water content, pH and ageing. By increasing the solid content and the acid content, the viscosity of the sol-gel was almost constant, until it increased after 48 h. In addition, the formation of intertwined networks of polymers, as a result of ageing for 72 h, increased the viscosity of the sol-gel, resulting in good reproducibility. The coating showed

good adhesiveness when tested in an ultrasonic bath and only 4 mass% of the original loading was lost.

2.2.9 Sol-gel coating on Dixon rings

With the emphasis on smaller, cleaner, and more energy-efficient process units, implementing a packing that promotes the transfer of mass and heat while keeping a low-pressure drop is necessary [96]. Metallic packing with a three-dimensional structure such as a mesh-based structure would deliver promising phase contacts in multiphase process applications (i.e., distillation, absorption, adsorption, catalytic systems, etc.), reducing capital and operating costs. Tuning the surface of the Dixon rings with uniform coating can have many benefits, such as developing hydrophobic and hydrophilic packing [97], such as in the trickle bed reactor [98]. As demonstrated in Table 2.3, when compared with similar packings, Dixon rings offer a larger surface area. [99]. The specific surface area is also known as the area per unit volume which indicated the rate of mass and heat transfer. The void percentage is defined as the ratio of pores to the total volume of the packing.

Table 2.3. Physical properties for random packings.

	Berl saddles $^1/_4$ in [26]	Raschig ring $^1/_4$ in [26]	Dixon Rings $^1/_4$ in [100]	Dixon Rings $^5/_8$ in [100]
Specific Area (m^2/m^3)	352	610	900	500
Void (%)	62	72	90	87

2.3 Hydrodynamics

The packed column is filled with packing material, creating a void due to the contact points between the packing. There has been an interest in studying how the physical packing properties affect flow patterns in single and multiphase applications such as gas-liquid and gas-liquid-solid applications. The packing size, material, void fraction, and surface area highly affect the flow pattern [101]. Therefore, packing is characterized by various operating conditions such as the liquid and gas flow rates to test their hydrodynamic performance. Dixon rings are made of a metallic wire mesh grid and a section in a longitudinal direction of the ring [66]. Improving flow inside the packed columns requires understanding the flow pattern at microscopic and macroscopic scales. The flow regime and several hydrodynamic parameters such as liquid holdup, effective surface area, and pressure drop highly affect the mass transfer capabilities. The next chapter in the literature review section discusses macroscopic studies [102]. Understanding the relevant flow characteristics on a microscale, such as dispersion of the liquid phase and wetting efficiency of the packing has been extensively investigated, owing to the impacts of these characteristics on process design from economic and environmental perspectives. The wetting efficiency of the packing is a critical design parameter as it affects the gas-liquid interface where the chemical process takes place and the flow patterns of multiphase systems. It shapes liquid flow variations under various regimes (i.e., droplets, rivulets, bubbles, or trickle types), directly influencing mass and heat transfer phenomena [5].

2.3.1 Flow regimes

Gas and liquid interactions with the packing result in a different flow regime [103]. The flow regimes in the packed column are divided into film flow, trickle flow, spray flow, and pulse flow, as shown in Figure 2.9. The flow regime depends on the operational parameters such as the gas and liquid flowrate and the physical properties of the packing [104]. At low operational conditions for gas and liquid flow, the liquid forms a film over the packing material; this is called film flow. The movement of the liquid in this flow regime provides a high wetting area, which increases with the increase in liquid flow rate. When the gas flow rate is increased while the liquid flow rate is unchanged, some of the liquid is transformed into droplets, known as the trickle flow regime. When the gas and liquid flow rate are increased, all the liquid will form droplets, known as the

spray regime. When gas flow rates are very low compared to liquid flow rates, bubbles are formed in a continuous liquid phase. The dispersion of bubbles in liquid is known as the bubble flow regime.

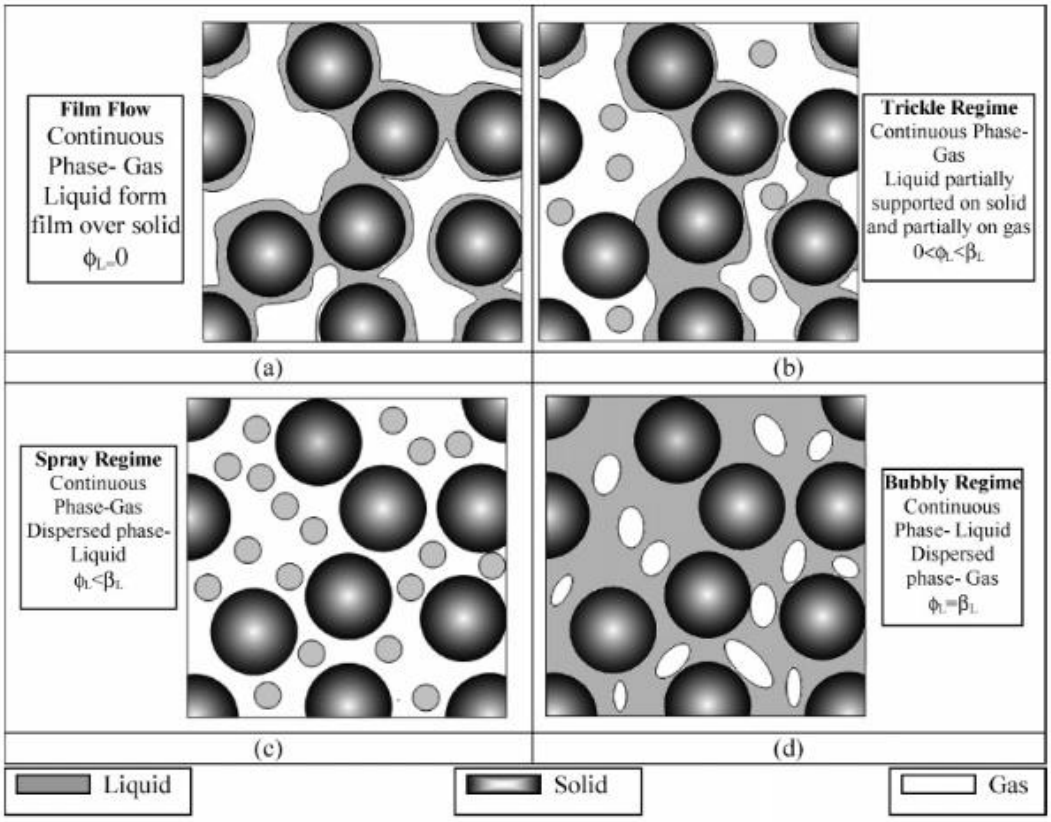

Figure 2.9: Flow regimes in packed columns taken from Gunjal et al. [105].

Methods to capture the flow regime include signal analysis using non-linear time data points [106] [107] and pressure fluctuation methods [108] [109]. It was concluded that the signal methods could not capture the flow regime accurately. On the other hand, the pressure fluctuations methods were found to be capable of capturing the flow regime. However, these methods could not capture the transition between the flow regime. Since experimental techniques fail to capture sharp transitions between phases, the flow regime is usually identified using CFD methods. Gunjal et al. [105] implemented a wall fluctuations model for the gas and liquid flow using CFD to predict the nature of the flow regime. Tong et al. [110] studied the flow regime on structured triangular packing using 2D and 3D CFD models using VOF method. They measured the velocity profiles of the liquid from the CFD simulation were validated using scientific Complementary Metal–Oxide–Semiconductor (SCMOS) camera. The liquid flow pattern showed the film flow regime at low gas

and liquid velocities. It can be concluded that 3D packing studies are highly required but still lacking for packed columns [111]**.** The opportunity to apply CFD as a tool to model the flow distribution in packed columns has enabled significant progress in understanding the flow regime for fluid-solid interactions of various geometries and solid types [112]. The spatial resolution of these methods helped link the complex geometrical configuration of the packing and operational parameters to patterns of the flow and thus assess interactions of the gas, liquid and solid phases of multiphase systems [113] [114].

2.3.2 Liquid maldistribution

The applications to randomly packed columns have been limited due to scale-up difficulties because the flow distribution is not clearly understood. Sometimes it is assumed that the gas flow has a uniform distribution all over the length of the column. The liquid flow distribution is complex and non-uniform due to the distribution of the voids and the bad distribution of liquid from the nozzle [115]. Therefore, understanding the fluid-fluid and fluid-packing interaction is essential because of the stagnation zones and the dead-zones, which impact the operation's efficiency. A major disadvantage of the liquid mal-distribution in packed columns is poor mixing, resulting in low mass and heat transfers. In addition, the liquid mal-distribution keeps increasing along the tower's length, especially when the column diameter is above 0.5 m [116]. Designing and scaling up packed columns has been fraught with difficulties due to the uncertainty of the flow pattern because of the mal-distribution. Tray columns can be the preferred engineering design in some cases because the mal-distribution does not add up along the tower's height. Each tray is independent.

The liquid mal-distribution has been understood since 1935 by a study conducted by Garner et al. [117]. This early study was conducted on spheres and saddles that were randomly packed without gas flow. It was shown that the liquid distribution is non-uniform, and the type of nozzle used highly affected the liquid flow pattern. Another investigation conducted by Porter et al. [118] showed that the liquid had a uniform pattern for Ranching rings. A model to describe the liquid flow distribution for Raschig rings and Intalox saddles was developed by Yin et al. [119]. The model was based on the diffusion theory for several different nozzle geometries. They found that the surface tension is not related to the changes in the flow distribution. Zhang et al. [120] showed similar results on the effect of the liquid physical properties on the uniform distribution of liquid.

Their results showed that the liquid pattern is not a function of the liquid surface tension. These claims were debunked by the investigation conducted by Onda et al. [121] showed that the liquid distribution varies significantly with the type of liquid and the surface tension.

A more recent study on the mal-distribution of liquid was developed by Souadnia and Lati [122] without the gas phase. The study was conducted for several types of random packing: ceramic and metallic Pall rings and metallic Raschig rings. The study was conducted on large and small scales. It was demonstrated that the radial mixing of liquid highly affects the rate of mass and heat transfers. They showed that the mal-distribution magnifies at a larger diameter due to the wall effects and the non-uniformity in the liquid distribution, which can lead to a significant decrease in unit efficiency. Harriott [123] conducted an experimental investigation in a 0.5 m diameter column packed with stainless steel saddles and ceramic Pall rings. The study was conducted for various parameters such as the liquid flow rates, packing volume, type of nozzle, and liquid properties. It was found that the liquid distribution becomes more uniform at higher gas velocity. Equivalent results were obtained by Dutkai and Ruckenstein [124] in an investigation conducted in 0.15 m diameter column which was packed with spheres.

Several experimental techniques measure the mal-distribution and visualize the gas-liquid flow in the packed tower. The tracer method is considered one of the classical and simplest methods to measure liquid distribution. This method injects an electrolyte into the top of the column and removed from the bottom. The tracer concentration profile is measured during the operation along with the height of the column, which determines the liquid distribution [125]. Tomography is a non-invasive method that can be employed to visualize the fluid flow distribution. In X-ray tomography, the scanning device is placed with a moving arm on a table, allowing it to rotate around the packed column. One main disadvantage of X-ray tomography is the minimum scannable column diameter is 0.5 m. Gamma tomography visualizes a 3D flow pattern in the packed column. The main advantage of tomography is the precision to accurately detect any changes in the uniformity of the flow pattern on a local scale. The biggest disadvantages of tomography are the elevated level of safety required to conduct the operation due to the radiation and the expensive machinery [126].

CFD links the complex geometrical configuration of the packing and operational parameters to the flow patterns. It assesses interactions of the gas-liquid-solid phases of multiphase systems.

Applying CFD to model the flow distribution in packed columns has enabled quick progress in studying fluid-solid interactions of various geometries and solid types. The spatial resolution of the CFD methods allows capturing the interphase of surfaces between the liquid and the solid packing. Unfortunately, CFD simulations must be conducted for a small number of packing elements due to the computational cost of the fluid flow models. Therefore, simulations on an entire packed column are unrealistic nowadays [127].

2.3.3 Hydrophobic and hydrophilic packing

Hydrophobicc packing are used for Volatile Organic Compounds (VOCs) in multiphase system gas water PolyDiMethylSiloxane (PDMS). They are also used in hydrogen isotopic exchange applications. H_2O-H_2S exchange reaction happens fast and does not need catalyst while other exchange reactions need catalyst to increase the reaction rate. Potassium methylamide catalyst (CH_3NHK) is an effective catalyst for CH_3NH_2-H_2 exchange reaction while a hydrophobic catalyst is needed for H_2O-H_2 exchange reaction..

The contact angle is calculated using Young's equation which is based on the thermodynamic equilibrium between two or three phases. It is a function of the interfacial energy and surface tension as shown in equation (2.3). When the contact angle is higher than 90°, a hydrophobic non-wetted surface is obtained, whilst a hydrophilic wetted surface is reached when it is less than 90°.

$$\gamma_{S.G} - \gamma_{S.L} - \gamma_{L.G}\cos(\theta) = 0 \qquad (2.3)$$

Where γ is the interfacial energy, S is solid, L is liquid, and G is gas.

The droplet's adhesion to the solid surface determines the value of the contact angle. The attraction forces for a hydrophilic surface are higher than the hydrophobic ones. In a hydrophilic surface, the droplet will spread over the surface until reaching equilibrium due to internal flow inside the droplet, which results from the collision. The viscous forces are developed at the three-phase contact lines due to eddies. The increase in viscous forces interacts with the capillary forces, thus, it can control the spreading rate and the wetting properties. If the droplet adhesion to the surface is higher than its cohesion, the droplet will spread over the surface at a contact angle of less than 90°. When the cohesion forces are higher than adhesion forces, the contact angle is higher than 90°. Young's work describes the droplet cohesion, adhesion, and contact angles [44]. Grewal et al.

[129] developed a model to measure the spreading rate and droplet profile. The model was based on viscous, capillary, and contact angles for hydrophobic and hydrophilic surfaces. The viscous forces are calculated using equation (2.4) which is a function of u (velocity), h (height), d (droplet diameter), p (length of capillary pillars), and μ (viscosity).

$$F_{texture} = \frac{\mu u h}{p^2 \ln(^{p}/_{d})^{r}} \qquad (2.4)$$

The capillary forces are function of the equilibrium contact angle (θ_{eq}) surface roughness factor (r_f) and the potential interface of the solid-liquid and gas interface (γ) as shown in equation (2.5)

$$F_{cap} = \gamma\,(r_f \cos\theta_{eq} - \cos\theta(t)) \qquad (2.5)$$

Zhang et al. [130] developed an empirical model based on the droplets splashing and spreading as a function. The effect of impact velocity on the spreading was evaluated based on the contact angle and the dimensionless numbers, such as Weber number (W_e) and Reynolds number (R_e), as shown in equations (2.6) and (2.7), respectively. W_e is used in describing the flow in multiphase systems which have a fluid interface [131]. R_e describes the ratio between the viscous and interatrial forces, which helps predict the flow pattern [132].

$$W_e = \frac{\rho u^2 l}{\sigma} \qquad (2.6)$$

$$R_e = \frac{\rho u l}{\mu} \qquad (2.7)$$

where ρ is density (kg.m^{-3}), u is velocity m.s^{-1}, l is droplet diameter (m), σ is surface tension (N.m^{-2}) and μ is the dynamic viscosity (Pa.s).

The spreading speed for the hydrophobic surfaces was higher than the hydrophilic surface due to less viscous dissipation. The wetting efficiency is entangled by the liquid distribution over a surface, the operating flow, and the packing (i.e., materials and geometries). Small droplets form a higher surface area in gas/liquid, solid /liquid, and solid/gas/liquid flows in packed columns. Hydrophobic packing results in poor liquid mixing, which limits the packing mixing capabilities. On the other hand, hydrophilic packing results in higher mass transfer rates but is accompanied by

high-pressure drop. Depending on the application of interest, hydrophobic, hydrophilic, or both are selected. Ma et al. [133] studied the flow characteristics for hydrophilic metal packing. Linek et al. [134] and Kumar [135] gathered data on the characteristics of hydrophobic plastic packings. Hydrophobic packing are commonly used in hydrogen isotopic exchange. Kumar *et al.* [136] compared the mass transfer and dispersion in packed beds of hydrophobic and hydrophilic Raschig rings using the radiotracer technique. They confirmed the anticipated high dispersion in the case of hydrophobic packing and the mass transfer in the case of hydrophilic packing.

Yan and Gao [137] investigated the effect of the contact angle on the interfacial wettability for a packing coated by the spray and dipping methods. It proved that the lower the contact angle is, the less pressure drop occurs, resulting in high weeping rates. The hydrodynamics and mass transfer performances in a rotating packed column with a hydrophobic mesh were investigated by Zhang *et al.* [138] using a high-speed camera. They evaluated the dispersion by observing the cone angle generated from the splashes of droplets-solid packing interactions. The results showed that a hydrophobic mesh was more capable of spreading the liquid and thus improving the liquid dispersion. They noted that the liquid dispersion increases due to an increase in the shear forces between the water and the solid surface. Parameters such as the macrostructure and surface energy of the substrate highly affect the dispersion. The droplet can pass through the wire mesh grid if the surface is superhydrophobic due to the low friction. Ma *et al.* [133] studied the wetting efficiency in a rotating packed bed of alumina-coated stainless-steel mesh. Compared to the uncoated stainless-steel mesh, the coated wire showed a higher wetting ratio, leading to an increase in mass transfer efficiency by 45.7 %. Su *et al.* [139] used a series of stainless-steel substrates to study the wetting efficiency in a rotating bed reactor. The wetting efficiency was related to the surface hardness and surface free energy, which allowed an understanding of the role of the coating material on the wetting efficiency behaviour.

Wire mesh has been employed in multiphase applications that generate fine liquid elements to increase the contact area between the gas, liquid, and solid [140]. Song [43]broke a liquid jet using a wire mesh to create finer droplets. They showed a conical area was formed after the liquid contacted the wire mesh. Kooij et al. [141] also studied the liquid dispersion for spray application. Using a metallic wire mesh, they created finer droplets by breaking a liquid jet. One method that can be used to adjust the wetting efficiency is applying a surface modification of the packing using

a uniform coating of hydrophobic or hydrophilic nature, depending on the application of interest. A uniform coating can change the structure of the surface composition; therefore, it reflects a change in the surface energy and the contact angles. With all the above mentioned, there is a need for a packing that provides excellent mixing ability with a tunable wetting efficiency, which can be used in RPB and PBR.

2.3.4 Multiphase models

CFD is a computerized tool used to study fluid flow by solving the Navier-Stokes equations. With the high cost of experimental techniques to analyze the flow, CFD is becoming a better option due to the fast development in computer technology [142]. In a CFD simulation, boundary conditions must be defined, along with selecting the numerical solver used to compute the model equations. As shown in Figure 2.10, the fluid domain is divided into very small elements called mesh, and the initial solutions are defined based on the problem. There are several approaches to model hydrodynamics in the packed column using CFD [143]. The first is macroscale analysis, which focuses on modeling the packed column. This approach is not realistic because it is computationally demanding. Thus, assumptions are made to simplify the model. In addition, this approach would not give a clear and detailed understanding of the flow pattern. A better approach is to focus on a few packing elements or a small section less computationally demanding than the entire packed column. This approach is used to obtain a detailed analysis of fluid flow and fluid-solid interactions. The wetted area, liquid holdup, and pressure drop can be calculated using this approach [144].

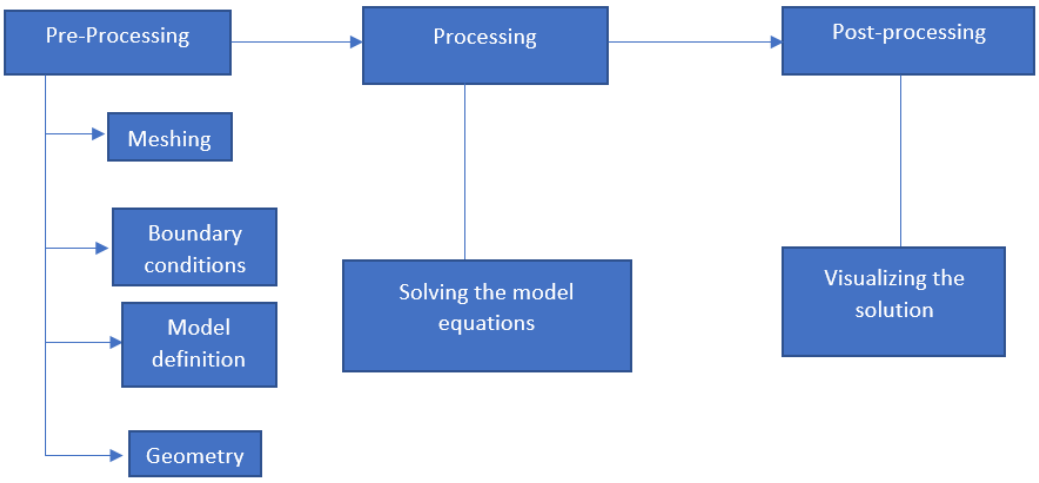

Figure 2.10: The procedure for solving a CFD problem

The study at the microscale level of packing is a promising approach to understanding the phenomena that take place and predicting those that occur at large scales. Since the wetting performance and liquid dispersion are critical information to anticipate, developing surface characteristics of a packing that would be tuneable is essential for multiphase flow. In addition, the visualisation of the dynamics of the wetting at the macroscale level is still not sufficiently mature since existing methods that allow observations of time-integrated data. In contrast, the flow dynamics, particularly at low velocities, where the time resolution of observation is critical, are not straightforward [145] [146].

2.3.4.1 Lagrangian- Lagrangian method

Lagrangian approach is a discretized phase approach based on a moving mesh method. In Lagrangian method, the particles flow under the Newtonian rules of motions. This approach has advantages over Finite Element Method (FEM) and Finite Volume Methods (FVM). The mesh created is less complex than the ones created by FEM and FVM, thus less computationally demanding. Therefore, Lagrangian methods became popular in modelling randomly distributed particles [147]. The fluid domain is divided into arbitrary points based on the particle's position, which tracks the movement. The local information such as the fluid velocity can be extracted for each particle from time t=0 to time "t". A complete picture of the fluid flow can be obtained by gathering the local information for all the local points. In addition, particles interactions are

considered as in real life scenario, the mass, momentum, and energy equations of Navier-Stokes are solved by Lagrangian method [148].

2.3.4.2 Lagrangian- Euler method

Combining Lagrangian and Euler method has been used extensively for modelling multiphase flow in packed column. This method combines both continuum and discretized approaches for modeling the flow. For the phase with large volume fraction, the Euler method is used for a continuous phase, most commonly the gas phase. However, this approach fails to model the flow when the volume fraction the fluid is high [150]. On the other hand, the Lagrangian method tracks discretized phases such as gas, bubbles, solid particles, liquid droplets, etc [149]. Therefore, particle tracking has become common for modelling spray towers and fluidized bed reactors.

2.3.4.3 Euler-Euler methods

The Euler approach is commonly used to model gas-liquid flow in packed columns. In the Euler-Euler method, the fluid is considered as a continuous and the volume fraction of the fluid is high. The volume fraction method is used in the Euler methods since the volume of one phase cannot be occupied by another phase at a given space and time. In addition, the summation of the volume fractions at a given space and time is one [151]. Several models are based on the Euler methods: mixture model, Eulerian model, and VOF model [150].

2.3.4.3.1 VOF method

The VOF method is based on tracking and locating the interphase between two or more fluids. The VOF belongs to the Eulerian approach for modelling multiphase systems where the mesh is either fixed or moving to form a sharp interface. The VOF model contains equations to track the fluid interface [152]. In addition, the momentum balance equations must be solved for each phase and the volume fraction must be computed for each cell in the fluid domain. The VOF model is commonly used when the volume fraction for each phase is large such as in the motion of big particles in water and the jet flow. More details about the VOF model can be found in Lou and Zhu [150] work.

2.3.5 Wetting efficiency

2.3.5.1 Purpose

The wetting efficiency is entangled by the hysteresis of the liquid distribution over a surface, the flow regime, the operating flow and the type of packing (i.e. materials and geometries) [5]. The wetting efficiency of the packing is a critical design parameter as it affects the gas-liquid interface where the chemical process takes place as well as the patterns of flow of multiphase systems. It shapes variations of the liquid flow under various regimes (i.e. droplets, rivulets, channelled or trickle types), directly influencing mass and heat transfer phenomena [1]. The wetting efficiency is defined by the contact angle, which is the angle between the tangent to the interface of a droplet and the solid walls. When the contact angle is higher than 90°, a hydrophobic non-wetted surface is obtained, whilst a hydrophilic wetted surface is reached when it is less than 90°. The wetting efficiency is entangled by the hysteresis of the liquid distribution over a surface, the operating flow and the type of packing (i.e. materials and geometries).

2.3.5.2 Previous studies

Early efforts were made by Billet and Schultes [26] on modelling the wetting efficiency of a randomly distributed packing using a large experimental database to derive correlations on the liquid holdup, effective surface area and $K_{G_a}a_v$. Rocha et al. later developed an improved model for multichannel flow through structured packing. The relevance of properties such as the contact angle (θ) and the size of the corrugations was reported. A flow model at microscale was highlighted based on correlations of the liquid holdup, the partial wetting, and the liquid film thickness. Lambert and Gonzalez [154] used a bouncing droplet over a super-hydrophobic surface to demonstrate that the characteristics of a solid surface affect the shape and flow pattern. Dong *et al.* [155] developed an effective strategy to control liquid overflow on a micro-nano structured super-hydrophilic surface. Haroun *et al.* [156] and Ataki and Bart [157] investigated the wetting efficiency of structured packing, namely Mellapak 250.X and Rombopak-4M, respectively. The flow characteristics were reported by 3D simulation that captured the motion variations of the gas-liquid interface. They combined the VOF model and the Eulerian-Eulerian model to investigate the effects of operating flow and properties of the liquid on the behaviour of flow variations and reported modifications of existing correlations on the liquid holdup and the effective surface area for the structured packing. They emphasised the relevance of the θ on the flow regime. The higher

the θ is, the more responsible it is for changing the flow from a trickle to bubble flow. Other works showed the feasibility of this modelling approach. The surface wetting ratio of a single catalyst particle was studied by Du *et al.* [158] and Augier *et al.* [159]. The former studied the effect of different operating flow rates, liquid viscosities, and contact angle on the liquid film thickness, and the latter investigated the reactive efficiency of different catalyst shapes. Overall, few studies investigated the wetting efficiency of gas-liquid flow in packed columns using a combination of spatially resolved experimental imaging and 3D modelling. Such an approach would demonstrate the relevance of conducting evaluations at the microscale level and help understand the changes in flow-packing interactions.

2.3.5.3 Effect of coating

One method that can be used to adjust the wetting efficiency is by applying a surface modification of the packing using a uniform coating of hydrophobic or hydrophilic nature, depending on the application of interest. Kumar *et al.* [136] compared the liquid hold up and the axial dispersion in packed beds of hydrophobic and hydrophilic types using the radiotracer technique and confirmed the anticipated high dispersion in the case of hydrophobic packing and the high holdup in the case of hydrophilic packing. Yan and Gao [137] investigated the effect of the hysteresis of the contact angles on the interfacial wettability for a packing that was coated by the spray and dipping methods. It proved that the lower the contact angle is, the less pressure drop occurs, resulting in high weeping rates. The hydrodynamics and mass transfer performances in a rotating packed column with a hydrophobic mesh were investigated by Zhang *et al.* [138] using a high-speed camera. They evaluated the dispersion by observing the cone angle generated from the splashes of droplets-solid packing interactions. The results showed that a hydrophobic mesh was more capable of spreading the liquid and thus improving the mixing capabilities. Ma *et al.* [133] studied the wetting efficiency in a rotating packed bed of alumina coated stainless steel mesh. Compared to the uncoated stainless-steel mesh, the coated wire showed a higher wetting ratio, leading to an increase in mass transfer efficiency by 45.7 %. Su *et al.* [139] used a series of stainless-steel substrates to study the wetting efficiency in a rotating bed reactor. The wetting efficiency was related to the surface hardness and surface free energy which allowed an understanding of the role of the coating material on the wetting efficiency.

2.3.6 Opportunity

The opportunity to apply CFD as a tool to model the flow distribution in packed columns has enabled significant progress in studying the wetting efficiency for fluid-solid interactions of various geometries and solid types. The VOF approach has principally been used and was conducted in combination with the Eulerian-Eulerian model, allowing capture of the interphase of surfaces between the liquid and the solid packing [112]. The spatial resolution of these methods helped link the complex geometrical configuration of the packing and operational parameters to patterns of the flow and thus assess interactions of the gas, liquid and solid phases of multiphase systems [114].

Since the wetting performance and liquid dispersion are critical information to anticipate, the development of surface characteristics of a packing that would be tuneable is essential for multiphase flow. The study at the microscale level of packing is a promising approach to understand the phenomena that take place and predict those that occur at large scales. In addition, the visualisation of the dynamics of the wetting at the macroscale level is still not sufficiently mature since existing methods that allow observations of time-integrated data while the dynamics of the flow occurs, particularly at low velocities, where the time resolution of observation is critical, are not straightforward [146].

2.4 Fluid and mass transfer theory

The hydraulic capacity should be identified to calculate the requirements for the height and inner diameter of the packed column. Studies have shown that increased hydraulic capacity reduces mass transfer performance due to flooding [160]. Therefore, parameters like pressure drop, liquid holdup and $K_{G_a}a_v$have been widely studied. Packing that offers lower pressure drops has the highest hydraulic capacity and mass transfer efficiency, thus is demanded [100]. For application in the industry, it is critical to assess and characterise the packing material [102]. Packing with low-pressure drop are demanded to save the energy needed to power the pumps. Random packings such as Pall rings, Raschig rings, and Intalox saddles have been investigated [161].

Dixon rings offer a large surface area, which envisages higher mixing capabilities. In addition, a higher void percentage allows the gas to flow with a lower pressure drop [26]. Random packings usually force the liquid to flow near the outer walls of the column, which results in bad mixing and low efficiency. Therefore, most random packing in gas-liquid applications requires redistributors for the liquid. Unlike all random packing, experiments have shown that Dixon Rings encourage the liquid flow through the center of the column. This phenomenon is known as the funneling effect, which is beneficial due to the low dynamic liquid holdup of liquid, which results in a lower pressure drop [162].

Moreover, the liquid and gas operational flow rates were low because the column's dimensions were small in these studies. Kaba et al. [163] studied the pressure drop for several Dixon ring sizes and porcelain packing. Pressure drop was measured for an isotope separation distillation process, which is different from other applications such as absorption. In this study, the variation in the gas was limited, a few data points were tested for each packing size, and only one liquid flowrate was tested. Moreover, the Dixon rings were made in China. It may differ from the Dixon rings evaluated in this thesis. Therefore, measurements of hydrodynamic factors such as pressure drop, liquid holdup and $K_{G_a}a_v$are needed for Dixon rings packing.

2.4.1 Pressure drop

The pressure drop is an essential parameter in the design of packed columns. The pressure drop is affected by the gas and liquid flow rate, density, viscosity, packing type, and height. In gas-liquid applications, pressure drops occur due to the collision of the liquid and gas in the column. In a

counter-current regime, the liquid flows down the column due to gravitational forces while the gas flows upwards. The liquid flowing downwards is resisted by gas rising in the opposite direction. When the operational flow rates are increased, the area free of flow decreases, and the friction force increases. The liquid holdup and pressure drop increase until reaching the flooding region since the liquid holdup increases the pressure drop. Therefore, the liquid holdup is an important hydrodynamic parameter that should be investigated. The liquid holdup is divided into static and dynamic. The static liquid holdup is the amount of liquid held in the column after complete draining. The dynamic liquid holdup is the amount of liquid held in the column at a single point due to friction forces initiated by the fluid flow [164]. The liquid holdup is linked to many hydrodynamics properties such as pressure drop, effective surface area, and the flooding boundary. Normally, it is calculated by stopping the flow at the inlets and outlets.

As shown in Figure 2.11, the pressure drop increases with the gas velocity and can be described using two cases. The first case is when the pressure drop is measured in a column without a continuous flow of liquid, dry or drained packing, as shown in Line A and B. The second case is when liquid flows down in the column, where three distinct regions are observed, as shown in XYC and XYD in Figure 2.11. The pre-loading is from 0 to X, the loading region is XY, and the flooding zone is YC and YD, as shown in Figure 2.11. Each region shows variation in pressure drop with the velocity of the gas. A linear relationship is found in the pre-loading region. The liquid holdup is constant in this region. The liquid holdup starts increasing at the loading region. Thus, the slope gets steeper at XY. This region is the best for operations since the mass transfer is optimal. Once point Y is reached, the flooding boundary occurs where pressure drop increases to infinity since the liquid holdup approaches infinity [165].

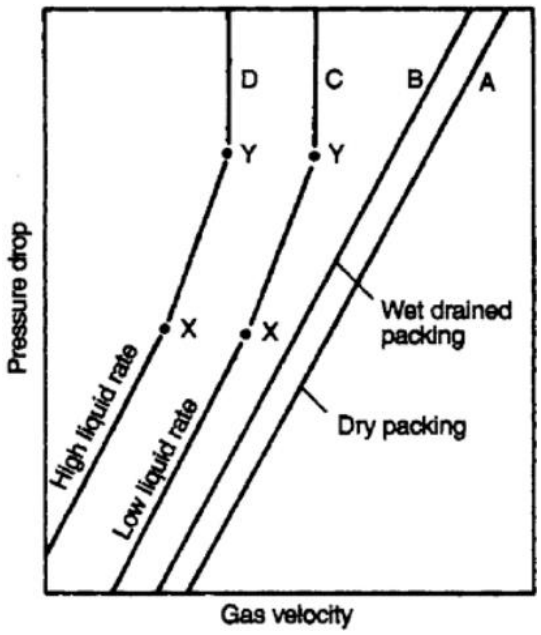

Figure 2.11: Variation of pressure drop with gas flow velocity Coulson et al.[165].

The pressure drop and liquid holdup were studied for Raschig ring and Berl Saddles by Mersmann [22]. This study was conducted under high pressure using supercritical CO_2 fluid and water. The dry pressure drop and liquid holdup were also estimated for the normal pressure of the operation using empirical models, and a model was developed to predict the flooding point. Bolles and Fair [166], Reichelt [167], and Molzahn, and Wolf [168] measured the pressure drop up to the flooding point for air-water systems for Intalox saddles, Pall rings, metal Pall, and Raschig rings. Zakerie et al. [169] investigated the pressure drop, liquid holdup, and mass transfer for Sulzer packing. The column used was 5m in height and 0.5 m in diameter. This investigation was conducted for a range of operational conditions and viscosity. The results agreed with correlations in the literature.

2.4.2 Liquid holdup

The liquid holdup is an essential hydrodynamic parameter that affects the pressure drop and the rate of mass and heat transfer. Like the pressure drop, the liquid holdup is a critical parameter in design, sizing, and identifying the optimal operating conditions in packed columns. The liquid holdup changes by changing the gas and liquid flowrates, the type of packing, and the physical properties (density viscosity, temperature, etc). Higher liquid holdup emphasizes higher heat and mass transfer performances [170]. The liquid holdup is the sum of the static and dynamic holdups. The static holdup is not responsible for changes in the pressure drop, it occurs when the liquid

occupies the dead zones. The static liquid holdup doesn't change by changing the gas and liquid flowrate thus, it doesn't affect the rates of heat and mass transfer. On the other hand, the dynamic liquid holdup is affected by changing gas and liquid operating conditions. The dynamic holdup affects the pressure drop and the rates of mass and heat transfer [171].

Many researchers studied the liquid holdup for one phase flow in packed column such as Saez et al. [171], Raynal and Haroun et al. [156] and others used CFD simulations in order to estimate the liquid holdup for co-current flow. The multiphase flow of gas and liquid was studied by Maćkowiak [28], Aferkaa et al. [172] and Schildhauer et al. [173] in a trickle bed Reactor of monosized particles. The liquid holdup for a small element of structure packing was studied by Shu et al. using CFD simulations. They implemented correlations of Bornhiitter and Mersmann [174] to predict the liquid holdup for the liquid rivulet for a single packing element. However, the geometry of the packing was simple which doesn't describe accurately what occurs on larger scales. Iliuta et al. [175] conducted a 1D CFD simulation for gas-liquid flow over a packing element in a counter current operation. Unfortunately, this study was conducted using 1D which makes it difficult to compare to actual flow [176].

The liquid holdup models developed by Billet and Mackowiak [22] are based on constants specific for each type of packing. However, the model constants are not available for all types of random packing. These models are based on fitting the experimental data to estimate the model constants. Olujic [18] developed the well-known Delft model to estimate the liquid the holdup for random packing. One of the model assumptions is that the packing is completely covered with liquid. The liquid holdup is a function of the liquid film thickness, the effective area and the packing dimensions [19]. Valenz et al. [177] developed models based on the Delft model to predict the liquid holdup for several random packing as a function of the packing dimensions. Unfortunately, the packing dimensions are not provided by all manufacturers due to commercial purposes. Many researchers have conducted studies to predict the liquid holdup, however several types packing are yet to be investigated such as Dixon rings.

2.4.3 Mass transfer

The mass transfer rate of any packing emphasizes the mixing abilities and the efficiency of the packing. Packing with a high mass transfer coefficient is required in the industry. Many studies have focused on measuring the mass transfer coefficient which relates the mass transfer rate to the

concentration gradient of species [178]. There are two approaches to model the mass transfer in packed columns. The first approach is simple and called the equilibrium stage model, which assumes the column is divided into several stages. In each stage, the gas and liquid reach equilibrium [179]. The theoretical stages are converted to equivalent height by calculating the height equivalent to a theoretical plate (HETP). The equilibrium approach is suitable to use for binary systems.

On the other hand, the second approach, known as the rate-based or non-equilibrium approach, is more realistic to use in a multi-component system in packed columns. The rate-based model is based on Henry's constant and is valid by assuming the gas and liquid reach equilibrium at the interface. In this approach, the mass and heat transfer rate are calculated through the concentration of species in the bulk phase. Chung et al. [180] developed an empirical model to describe the mass transfer rate for random packing. They have fitted experimental data conducted in a desorption column for air and water systems. The model is valid for saddle and ring packing and solvents near the water viscosity. A well-known study of the mass transfer in random packing was conducted by Shulman et al. [181]. This study was conducted using aqueous and non-aqueous solvents where the mass transfer factor (j_D) and liquid mass transfer coefficient (k_L) were calculated using equations (2.8) and (2.9), respectively. This study was conducted for a range of operating conditions such as temperature and gas and liquid velocity and physical properties such as viscosity and density. Kaiyun et al. [182] investigated CO_2 chemical absorption for Dixon rings packing using monoethanolamine (MEA) solvent.

$$j_D = 1.195 \left[\frac{D_P G}{\mu_G (1-\epsilon)}\right]^{-0.36} \qquad (2.8)$$

$$\frac{k_L D_P}{D_L} = 25.1 \left[\frac{D_P L}{\mu_L}\right]^{0.45} \left[\frac{\mu_L}{D_L \rho_L}\right]^{0.5} \qquad (2.9)$$

Where D_L is the diffusivity of solute in liquid, sq.f t./h., D_P diameter of sphere possessing the same surface area as a piece of packing, ft, μ_G is gas viscosity, lb/ h.ft, μ_l is liquid viscosity, lb/h.ft, ρ_L is gas density, lb/cu.ft, G is superficial gas rate, 1b.l (h)sq.f t /h.(sq.ft), L is superficial liquid rate, 1b.l (h)sq.f t / h.(sq.ft), j_D is mass transfer factor, ϵ= bed porosity

Onda et al. [121] developed correlations to describe the mass transfer coefficient as a function of the gas-liquid interface. They were the first to assume that the wetting percentage is the same as the effective surface area and thus they related the mass transfer coefficient to the wetting percentage. Wagner et al. [183] evaluated the mass transfer coefficient on a large scale in a 2 m distillation column. The study was conducted for a range of operating conditions of gas and liquid as a function of the liquid flow, and the packing properties. Billet and Schultes [26] developed correlation to describe the mass transfer coefficient as a function of hydrodynamic parameters such as liquid holdup and pressure drop, packing size and material. They have conducted experiments in a semi-pilot plant for the gas and liquid flowing in a counter current mode of operations. They assumed that the free volume is equal to the length of the liquid channels flowing in the columns. The mass transfer correlations were based on the diffusion model of Higibie.

3 Chapter 3: Methodology

This chapter includes a procedure for computational methods and experiments conducted in this research. This chapter include three parts:

1. Sol-gel coating
2. Fluid flow simulations and experiments on a microscale
3. Fluid flow experiments on a macroscale

The first part focuses on coating Dixon rings with ceramics. A sol-gel method was implemented to deposit alumina on the Dixon rings surface. Several sol-gel parameters were tuned until they reached a consistent coating of uniform thickness. The coating was evaluated using several characterisation methods including SEM, EDS, optical microscopy and BET. The second part tests the fluid flow at a porescale for the coated and the uncoated Dixon rings via CFD and experiments. The CFD model was validated using experiments for a packing element and a mesh independence study was conducted. A parametric study was conducted by varying the liquid flow rate and the contact angle relevant to hydrophobic and hydrophilic types of packing surfaces. The wetting efficiency of Dixon rings was evaluated, and the liquid holdup and the effective surface area from CFD were compared to models from the literature. The third part focuses on studying the hydrodynamic parameters on a larger scale. A semi-pilot plant was used to examine Dixon rings' liquid holdup, pressure drop and mass transfer coefficient. The 95_{th} centile method as described in Chapter 6.4 was applied to the experimental data of the hydrodynamics to develop models that describe the dry pressure drop and loading point.

3.1 Coating Dixon rings

Coating metals is a very challenging task as described in Chapter 2.1. Therefore, several methods were initially tested until coating with uniform thickness and good adhesiveness was produced. The washcoating method was employed for some initial tests to produce alumina coating on Dixon rings. In this method, alumina powder of 50 µm with ethanol to make a suspension, then the Dixon rings were dipped and dried. The resulting coating blocked the openings of the Dixon rings as shown in Figure 3.1. However, once the coating was dipped in water, it disappeared, making it unsuitable for gas and liquid applications.

Figure 3.1: Alumina coated Dixon rings by washcoating method

As described in the literature review in chapter 2.2.4, the sol-gel offers coating with good adhesiveness. Therefore, α-Al_2O_3 deposition on stainless steel mesh Dixon rings was investigated under controlled coatings to produce more adhesive coating. The resulting surface properties (thickness, morphology, and elemental composition) and mechanical properties (i.e., viscosity and adhesiveness) were discussed when the sol-gel coating parameters (i.e., the metal amount, the acid concentration, the mixing time, and the aging time) were varied.

3.1.1 Materials

Dixon rings $^1/_4$ in (stainless steel 316) were used as a substrate for the coating. The data on the structural size were provided by the supplier and are illustrated in Table 3.1. Aluminium isopropoxide (AIP, Aldrich) was the metal alkoxide precursor. Hydrochloric acid (ACS reagent, Aldrich) was used as a catalyst for the peptisation of the sol, while Polyethylenimine (PEI, Aldrich) was used as a binder. Deionised and distilled water was obtained by Milli-Q water filtration system (Merck). Names, molecular formulas, stated purity and source of all chemicals used in this section are presented in Table 3.1.

Table 3.1: Chemicals used in this section.

Compound	Molecular Formula	Purity (mass %)	CAS no.	Source
Aluminum isopropoxide	$Al[OCH(CH_3)_2]_3$	≥ 98.0	555-31-7	Sigma Aldrich
Hydrochloric acid	HCl	37	7647-01-0	Sigma Aldrich
Polyethylenimine	$H(NHCH_2CH_2)_nNH_2$	≥ 99.0	9002-98-6	Sigma Aldrich

3.1.2 Coating methods

AIP powder was hydrolysed into isopropanol and aluminium hydroxide by using an excess of H_2O at 353 K for at least 15 minutes under vigorous stirring (750 rpm) to reduce mass transfer limitation. Hydrochloric acid (HCl) was then added dropwise to catalyse the peptisation of aluminium hydroxide. The mixture was agitated while heating at 353 K until it became a transparent solution and then aged to establish an intertwined network of alumina. Dixon rings were degreased in an alkaline cleaner by using an ultrasonic bath for 30 mins at 348 K, dip-coated in the prepared mixture using an in-house dip-coater due to cost limitations of the project. The dip-coater was made of a syringe pump (Aladdin Programmable Syringe Pump, 1000-220) and a metallic rod, as shown in Figure 3.2.

Figure 3.2: In-house dip-coater

The dipping was conducted at a constant speed of 2.64 cm/min and calcined at 773 K for 1 h to eliminate the PEI and reach a continuous film of α-Al_2O_3. The range of different parameters that have been tested is presented in Table 3.2. The mixing time is the hydrolysis and condensation reaction time to give alumina as a product.

Table 3.2: Sol-gel parameters.

Parameter	**Range**
Al:H_2O (mol/mol)	0.005 – 0.02
HCl:Al (mol/mol)	0.13 – 0.33
Mixing time (h)	1 – 168
Aging time (h)	1 – 96
Binder concentration (g/L)	0.52 – 2.59
Number of deposition (cycle)	1 – 4
Calcination temperature (K)	773- 1273

3.1.3 Sample characterisation

The thickness and morphology of the coatings were characterised by optical microscopy (Zeiss, magnification: 10X, 0.20 HD) and SEM (JEOL JSM-7800F) operated at 20 kV. The viscosity of the coating solution was assessed by a capillary glass viscometer (Viscometer U Tube, BS/U BS188, Type C, VT/92056) with the nominal constants of 0.03 calibrated using distilled water, which met the ISO 17025 requirements. The chemical composition of the surface of the coating was analysed by electron-dispersive spectroscopy (EDS Shimadzu EDX 8000). The alumina powder (weighing 0.28 g) was pre-treated at 473 K in a vacuum oven for 4 h. The powders were then calcined at temperatures ranging from 773-1073 K and milled. The surface area and porosity were characterised by nitrogen adsorption using a Micromeritics 3Flex Surface Characterisation Analyser which was operated with a relative pressure between $1.3x10^{-9}$ to 1. The surface area was determined using the BET method operated with no degassing and a bath temperature of 77 K. The porevolume and the pore distribution were obtained using the Harkins and Jura adsorption isotherm method.

The coating load was evaluated by weighing the samples before and after coating using an analytical balance (Sartorius 2001 MP2, resolution: 0.1 mg). The coating adhesiveness was investigated by subjecting the coating to thermal oxidation at temperatures up to 1273 K for 3 h and ultrasound tests at 100 W for 10 mins. The validity of the coating method was confirmed by carrying out replicas of the assays. All results are presented as the average of at least two replicates along with the standard deviation shown on the error bars in the figures.

3.2 Pore-scale studies

In this section, spatially resolved procedures based on imaging using a CCD camera and 3D modelling, that combines the VOF and Eulerian-Eulerian models, were used to investigate the wetting behaviour of the Dixon ring subject to the multiphase flow under a trickle flow regime. The trickle flow exhibits partial wetting due to preferential channelling, leading to mal-distribution and uneven mixing. The local flows around an element of coated and uncoated Dixon rings were visualised by experimental imaging and compared with those obtained by 3D CFD simulation. The wetting efficiency of the Dixon rings and the liquid holdup, which impact the solid-liquid interfacial area and the dispersion of the liquid, were investigated through a parametric study by varying the liquid flow rate and the contact angle relevant to hydrophobic and hydrophilic types of packing surfaces.

3.2.1 3D modelling by VOF

3.2.2 Model setup

The initial values and the boundary conditions have to be defined for all the domains and the boundaries to solve the governing differential equations for gas and liquid phases. The initial values were specified by assuming that only the gas phase was present in the column, while the liquid phase was precluded from entering the column (i.e., at $t = 0$: $V_{f_2} = 1$ and $V_{f_1} = 0$). The inlet boundary was defined through the inlet velocity (u_o), and the outlet boundary was defined through atmospheric outlet pressure. Details about the model characteristics are given in Table 3.3.

A range of contact angles, from 60 to 120°, covering both hydrophobic and hydrophilic properties are given in Table 3.3. These values were selected as they reflect interactions of typical solvents with modified or unmodified surface structures [184].

Table 3.3: Parameters of the VOF model.

Multiphase model	**Volume of fluid**
Fluid	Air-water
Contact angle	60°, 90°, 105° and 120°
Surface tension (N/m)	0.0729
Operating pressure (atm)	1
Operating temperature (K)	293
u_o *(m/s)*	0.15, 0.25, 0.35 and 0.5
Gas inlet velocity (ms)	0.011
Thickness of the Dixon ring (m)	0.003 m

The boundary condition required the calculation of the frictional forces ($F_{friction}$) using the slip length (β). As shown in Figure 3.3, the interactions of the liquid with the solid surface were considered using the adhesive condition, which is known as the wetted wall boundary condition. This boundary condition allowed the definition of the constant static contact angle (θ). The wetted wall boundary condition was calculated by equation (3.1). The geometry, as shown in Figure 3.4 (a), included the column (i.e. height and diameter were set to 18 and 4.8 mm respectively) and the inlet nozzle (i.e. size of 1.5 mm). The Dixon ring was cut to have a diameter of 3 mm and a length of 2 mm, then placed at the centre of the column, as shown in Figure 3.4(a). Frictional force $F_{friction}$ was calculated according to equation (3.1):

$$F_{friction} = -\frac{\mu}{\beta}u \tag{3.1}$$

where β and μ are slip length (m) and viscosity (kg/(m. s)), respectively.

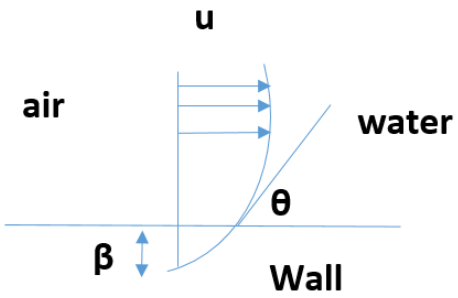

Figure 3.3: Constant contact angle "θ" at the wall boundary condition.

.

a) b)

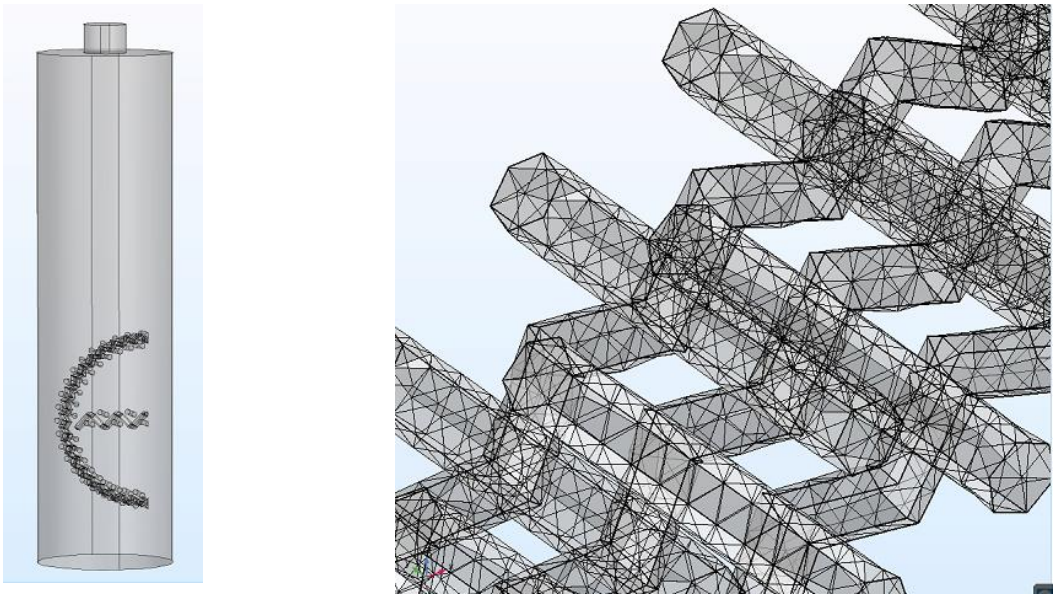

Figure 3.4. a) Illustration of the geometry of the 3D model; b) GR2 mesh distribution at the intersection of the wires, pore to mesh size ratio is 3.

A computer-aided design (CAD) drawing of the Dixon ring geometry was provided by Croft Filters Ltd (Risley, UK). The CAD drawing required some modification in order to reduce the

skewed elements occurring due to the intersections of the wires. Simulating the entire volume of the Dixon rings is computationally expensive due to its complex geometry

The intersections between the wires of Dixon rings had to be relaxed by 0.01 mm to avoid skewed meshing in both domain and boundary zones, as shown in Figure 3.4(b).

3.2.3 Solution procedure

The phase-field model included a phase initialisation step and a quick step. The phase initialisation study started with the phase field variable (ϕ). It ensured that it was smoothly varying throughout the domain, while the transient step solved the momentum conservation and Cahn-Hilliard equations. Moreover, the time-dependent study iteratively solved several non-linear equations for every time step using Newton's approach. This approach evaluated the Jacobian function and its computationally expensive derivative. The default settings in COMSOL minimised the computational power by calculating the Jacobian derivative using a constant damping factor. However, this model was associated with a high degree of non-linearity due to the complex geometry of the Dixon rings, which generated skewed mesh elements. The initial simulations diverged when a constant damping factor was used in the calculation. It was then replaced by the dynamic damping factor, which was computationally more expensive [185] [186].

The simulation started by discretising the fluid domain into many cells and the governing equations were then integrated for each cell. The differential equations were computed using an iterative solver (i.e., the generalised minimal residual solver) which was found to be effective and was then coupled with the geometric multigrid preconditioner to find numerical solutions for the non-symmetric matrices [187]. The preconditioner was used to coarsen the mesh using a multigrid, reducing the shape functions' order [188]. Other iterative solvers such as Flexible Generalised Minimal Residual method (FGMRES) and Biconjugate gradient stabilised method (BiCgStab) have been tested and provided similar results to the generalised minimal residual solver. The transient simulation was conducted using a time step of 0.005 s and relative tolerance convergence of 0.01%. The simulation was conducted for a co-current gas-liquid flow configuration, and the flow pattern results were described by the isosurface VOF value of 0.5.

3.2.3.1 Governing equations

The flow of the gas and liquid phases in the packed column are simulated by coupling the Navier-Stokes fluid flow model with the VOF method and solving by the Finite element method. The fundamentals of the phase-field model are described as follows, and more details about the model can be found elsewhere [189].

The VOF captures the diffuse interface between the two immiscible fluids (i.e., water and air) and uses the mixing and the storage energies at the interface by decomposing the Cahn-Hilliard second-order partial differential equations. The model is set to be controlled by the phase-field variable (ϕ), considering the synergies of mixing and storing energies at the interfacial region and ensuring minimization of the total energy correctly [190].

The phase-field model is simplified by assuming incompressible Newtonian liquid, constant viscosity, isothermal environment and laminar flow (i.e. negligible turbulence effects due to low velocity). The continuity and momentum equations are expressed by equations (3.2) and (3.3), respectively.

$$\nabla . u = 0 \tag{3.2}$$

$$\frac{\partial u}{\partial t}\,\rho + \rho(u.\nabla)u = [-pI + \mu(\nabla u + \nabla u^T) + F_g + F_s] \tag{3.3}$$

where p represents the pressure (Pa), ρ is the density (kg/m^3), u is the velocity vector (m/s), F_g and F_s are the gravitational and surface tension forces (N), respectively, and μ is the dynamic viscosity (kg/m.hr).

The phase-field model incorporates the effects of the volumetric forces, such as gravity and surface tension. The mixing energy represents the surface tension. The surface tension forces, which are distributed over the interface, are calculated using the phase-field variable (ϕ), as shown in equations (3.5) and (3.6), respectively. Therefore, this computation avoids complex terms such as the surface curvature and the surface normal, typically required in other multiphase models (i.e. the level set model) [191].

$$F_g = \rho g \tag{3.4}$$

$$F_s = \mathrm{G}\nabla\phi \tag{3.5}$$

$$G = -\nabla^2 \varphi\lambda + \frac{\lambda(\varphi^3 - \varphi)}{c^2} \quad (3.6)$$

where G is the chemical potential density (J/m^3), ϕ is the phase field variable (-), c is the capillary width (m) and λ is the mixing energy density (N).

Two additional equations are included in this model to capture the fluid interface. These equations calculate the phase field variable (ϕ) and phase-field help variable (ψ), as shown in equations (3.7) and (3.8), respectively.

$$\frac{\partial \phi}{\partial t} + \nabla . u\phi = \nabla . \frac{\gamma\lambda}{c^2} \nabla\psi \quad (3.7)$$

$$\psi = -\nabla . c^2 \nabla\phi + (\phi^3 - \phi) + \frac{c^2}{\lambda}\frac{\partial f}{\partial \phi} \quad (3.8)$$

where $\frac{\partial f}{\partial \phi}$ is the phi-derivative of external free energy (-) and γ is the mobility parameter (m^3.s . kg^{-1}).

The latter determined Cahn-Hilliard's diffusion time scale. It must be selected carefully to maintain a constant interfacial thickness and prevent overdamping the convective terms [192].

In the regions where fluids are segregated, i.e., no mixing, one fluid is set to take the element ϕ = 1 and the other fluid to take the element ϕ = -1. Conversely, the interface or the phase-field region is set in the range of these two boundary values, as expressed by using equation (3.8)

$$-1 \leq \phi \leq 1 \quad (3.9)$$

The phase-field model consider the discrepancies in the physical properties, i.e. density and viscosity, in regions where gas and liquid are in contact. The volume for each element should remain constant for incompressible fluids. Therefore, if one fluid would leave a tiny volume element due to the interfacial diffusion, the other fluid would occupy the same volume element and vice versa. The local density and dynamic viscosity or the mixture are calculated from local volume fraction values inside each cell of the calculation domain and areas described by equations (3.10) and (3.11):

$$\rho = \rho_1 V_{f_1} + \rho_2 (1 - V_{f_1}) \quad (3.10)$$

$$\mu = \mu_1 V_{f_1} + \mu_2 (1 - V_{f_1}) \quad (3.11)$$

The subscripts 1 and 2 in equations (3.10) and (3.11) refer to water and air, which are considered as Fluid 1 and Fluid 2, respectively. The volume fraction (V_f) is computed by equations (3.12) and (3.13):

$$V_{f_1} = \frac{\phi + 1}{2} \quad (3.12)$$

$$0 \leq V_{f_1} \leq 1 \quad (3.13)$$

3.2.4 Material and methods of experimental visualisation

3.2.4.1 Preparation and characterisation

The wettabiliies for coated and uncoated Dixon rings were evaluated. A sol-gel alumina coating of uniform thickness of approximately 20 µm was applied to the Dixon rings. The same method was used to prepare the hydrophobic Dixon rings. Dixon rings $^1/_4$ in made of stainless steel 316L were supplied by Croft Filters Ltd (Risley, UK) and were used as a coating substrate. The data on the structural size were provided by the supplier and are illustrated in Table 3.4. The choice of temperature was selected based on the adhesiveness. Temperature higher than selected range resulted in cracks formation and the ones in the lower range resulted in poor adhesiveness. The heating element was controlled and measured using a high-temperature ceramic chamber furnaces controlled using a ramp cycle.

Table 3.4: Uncoated and coated Dixon rings $^1/_4$ in structural data.

Wire mesh	**Diameter (µm)**	**Mesh (standard)**	**Length (mm)**	**Aperture (µm)**	**Calcination temperature (K)**	**Dipping cycles**
Uncoated	165	60 × 60	30	258	-	-
Coated	205	60 × 60	30	218	773	3

3.2.5 Experimental flow analysis over Dixon rings

The experiments were carried out to validate the VOF model and capture realistic wetting efficiency data for the coated and uncoated configuration. The uncoated Dixon rings were

degreased in an ultrasonic bath at 100 W for 10 mins and then dried at 373 K for 1 h. The coating was deposited by dipping Dixon rings in alumina sol-gel suspensions. AIP was selected as a precursor and was hydrolysed with the ratio of 1:100 (mol AIP:mol H_2O) at 353 K.

The experimental setup included a CCD camera (IMETRUM, video gauge) with 60 frames per second (fps) and resolution (640 x 480), flashlight, and image processing software (ImageJ). The experiments were operated at atmospheric pressure and ambient room temperature and were designed to reproduce the VOF model environment, as shown in Figure 3.5. A syringe pump (Aladdin Programmable Syringe Pump, 1000-220) with a precision of 1.2×10^{-5} ml/min and a needle orifice of 2 mm were used to provide the desired flow, capillary droplets and liquid filaments. The liquid injection was held 12 mm apart from the Dixon ring and the injection speed was changed based on the desired flow. The experiments were repeated three times to enhance the qualitative comparison of the liquid flow direction over Dixon rings with the model results. Both distilled water and black dye were used, which helped discriminate the droplets from the rings using the image processing Image J package. The Dixon rings were cleaned with acetone and dried before each experiment to remove any potential surface impurities. The time resolution of the camera was improved by capturing repetitive collisions of the droplets and capturing fine details of the collision and further dispersion of flow. A cycle of capillary droplet flow started when the droplet fell from the needle, impacted the Dixon ring and then left it.

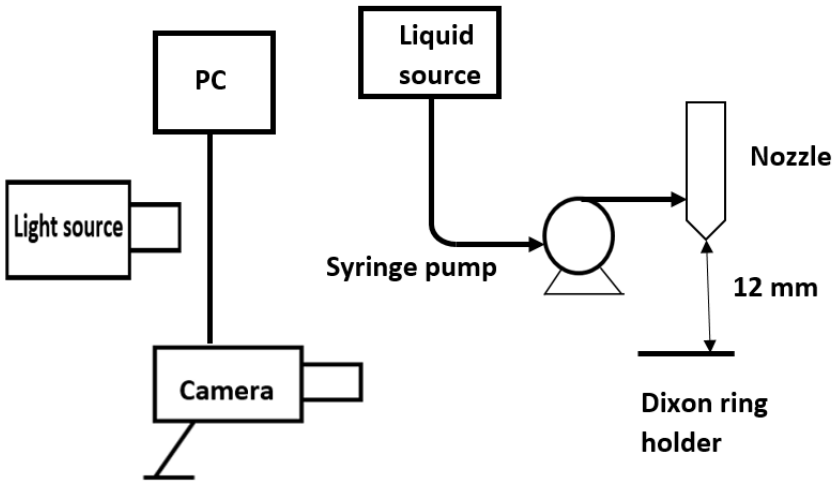

Figure 3.5: A schematic representation of the experimental setup for flow imaging over Dixon rings: PC – personal computer, camera – (IMETRUM, video gauge), syringe pump (Aladdin Programmable Syringe Pump, 1000-220), liquid source – water 500 mL tank, nozzle (20 mm ID).

3.3 Macroscale experiments for hydrodynamics and mass transfer of Dixon rings

This section deals with measuring and modelling the hydrodynamic properties of the Dixon ring. This includes measuring the pressure drop and the mass transfer coefficient at gas and liquid flow rates. Mass transfer testing using water and CO_2 as the target gas was also conducted to determine the mass transfer coefficient.

3.3.1 Equipment

Armfield manufactured the column, UK, as shown in Figure 3.6, was made of Poly-methyl methacrylate, with a diameter and height of 8 cm and 1.2 m, respectively. The column was packed separately with Dixon rings $^1/_4$ in and Dixon rings $^5/_8$ in. The packed column flow arrangements for pressure drop and mass transfer are described in Figure 3.7 and Figure 3.8, respectively. Alterations have been done to the semi-pilot plant to conduct the mass transfer experiments for CO_2. Two septum valves replaced the pressure measuring points to collect the gas for analysis, therefore the overall configuration was different. The list of symbols is described in Table 3.5. The gas outlet and valves (V-3), (V-4) and (V-5) gas were connected to the manometer for pressure measurements (P1) and are found at the top of the column. A liquid nozzle (10 mm Ø) and a mesh distributer (A-1) is also placed at the top of the column, as shown in Figure 3.7. In the middle part

of the column lies another mesh (A-2) to redistribute the discharged liquid and a valve (V-4) for pressure measurement. This allows measuring the pressure drop across the top and middle parts of the column. At the bottom lies the gas inlet and liquid outlet. U-tube was placed at the bottom to stop the gas from escaping from the liquid outlet. The gas and liquid flowrate were controlled using rotameters and mass flow controllers (MFCs) with solenoid-actuated control valves. A summary of the flow controllers is given in Table 3.6.

Figure 3.6: Experimental apparatus for the hydrodynamics studies.

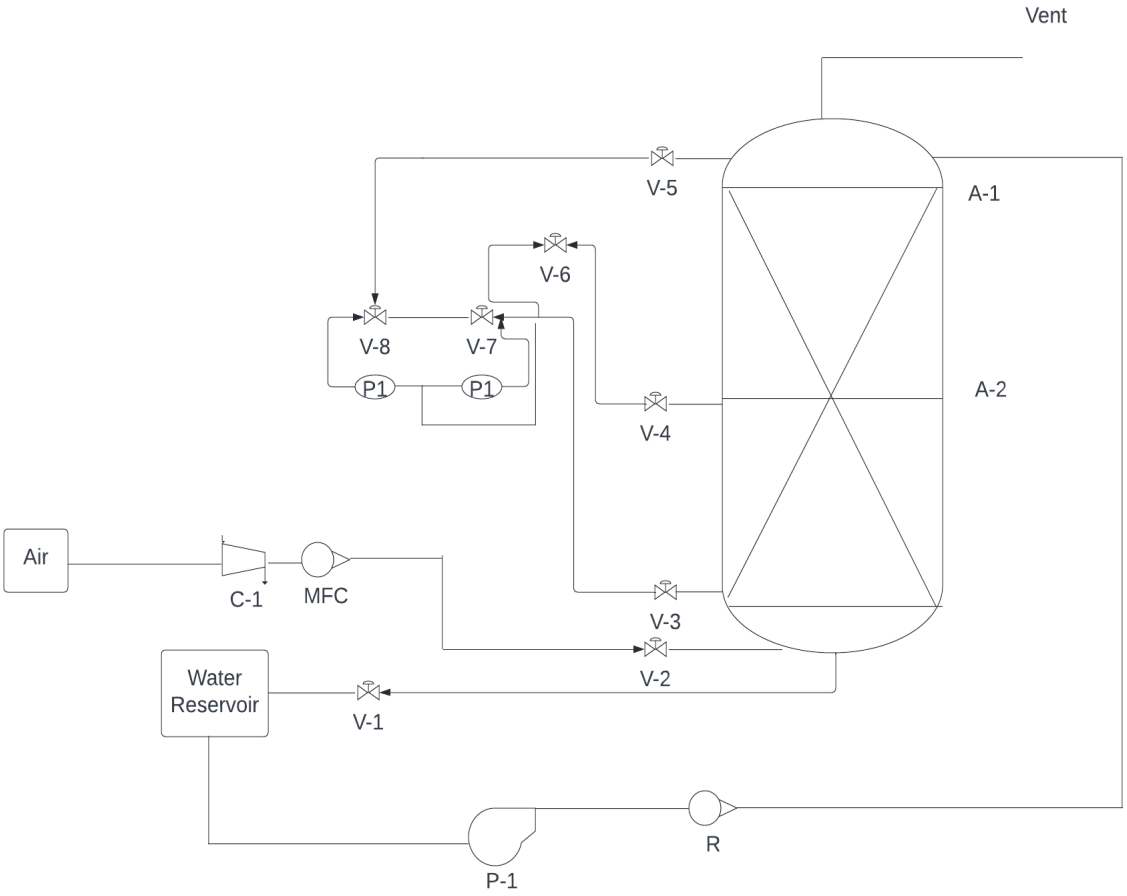

Figure 3.7: Packed column arrangement for hydrodynamics tests

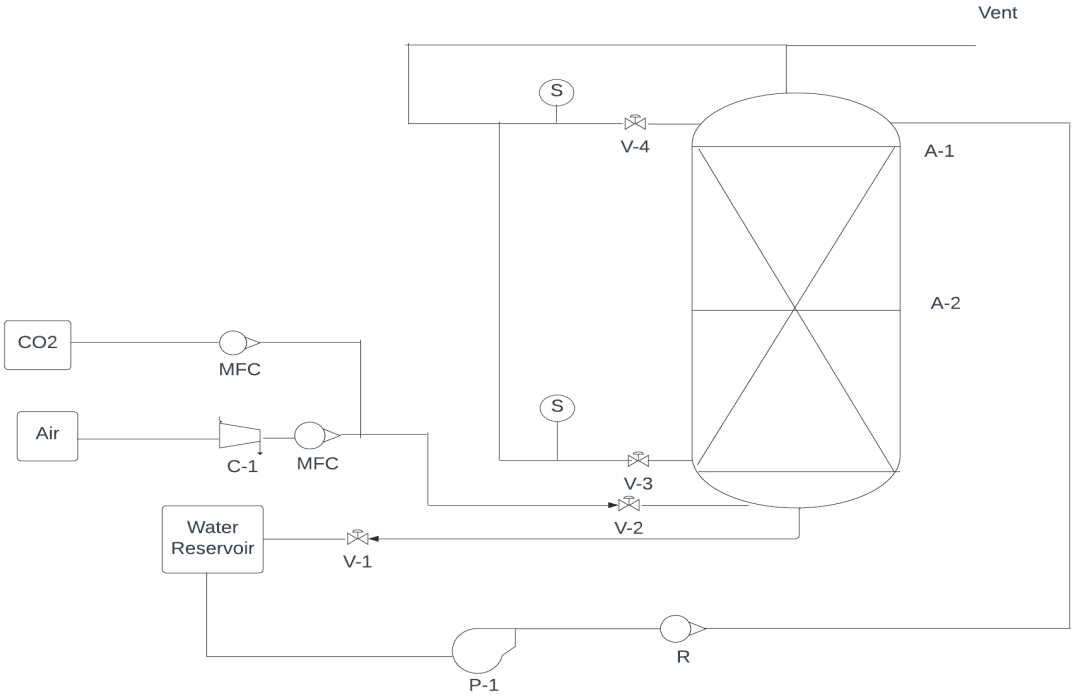

Figure 3.8: Packed column arrangement for mass transfer tests

Table 3.5: List of symbols

Symbol	V- (1-8)	P1	P-1	C-1	A- (1-2)	R	S
Value	Valve	Pressure	Pump	Compressor	Auxiliary	Rotameter	Sample point

Table 3.6: Flow controllers used in hydrodynamics test

Equipment	**Brand**	**Range (l/min)**	**Accuracy (l/min)**
Gas rotameter	Armfield	30 to 200	± 5
Liquid rotameter	Armfield	1 to 10	± 0.25
MFC (air)	Aera FC-7720CD	1 to 60	± 0.005
MFC (CO_2)	Aera FC-7720CD	1 to 60	± 0.005

In the mass transfer experiments, two sampling points were used to collect gas samples (S), as shown in Figure 3.8. Gas Chromatograph (GC, Thermo Fischer Trace 1300) was used to analyse CO_2 concentration at the inlet and the outlet. The thermal conductivity detector (TCD) and Micropacked Column (Restek ShinCarbon ST). The column properties and the GC setup are given in Table 3.7 and Table 3.8, respectively. The samples were injected using a gas-tight syringe (Thermo Fischer, 22G, 100 µL, removable needle) into the back SSL port, and Chromeleon 7 software was used to analyse CO_2 concentration data.

Table 3.7: GC column properties

Column type	Length (m)	ID (m)	OD (m)	Mesh type (standard)
ST Micropacked	2	0.00053	0.00074	80/100

Table 3.8: GC setup

Reference gas	Injection port	Split flow (ml/min)	Split ratio	Purge flow (ml/min)	Oven Temperature	Reference gas flow (ml/min)
Helium	Back SSL	20	5	1	165°C	1

3.3.2 Materials

The materials used for the hydrodynamics and mass transfer experiments are listed in Table 3.9.

Table 3.9.: Materials used in this section

Material	Supplier
CO_2 vapour withdrawal cylinder (>99.97)	BOC
Nitrogen cylinder (>99.9)	BOC
Water	United Utilities

3.3.3 Procedure

3.3.3.1 Pressure drop studies

For dry packing pressure drop, the liquid flowrate was set to zero for this experiment. The packing was dried by switching the gas flow at a maximum rate of 2 h. The liquid was set to a fixed value of 1, 2, 3, 4,5 or 6 l/min using P-1. The air flowrate was set to 10 l/min by V-2 and C-1, as shown in Figure 3.7. After 30 seconds, the pressure drop value was reported and the gas flowrate was increased by an increment of 5 l/min using V-2. After waiting 30 seconds the pressure drop value was captured. These steps were repeated until flooding was reached. All the experiments were repeated four times to ensure the validity of the data.

3.3.3.2 Mass transfer studies

The liquid flow rate for the CO2 absorption study was set to a fixed value of 1, 2 or 3 l/min using P-1. The MFCs were set to achieve a gas mixture CO_2/air ratio 0.2 (kg/kg). Samples (S), as shown in Figure 3.8 were collected every 10 minutes for at least 40 minutes to ensure that the steady state was reached. The flooding velocities were estimated in the pressure drop and were used to identify the gas flowrate, which were set to 60, 70 and 80% flooding velocity using MFCs. All the experiments were repeated three times to ensure the validity of the data. The effect of several parameters such as the solvent concentration, liquid flowrate, gas flowrate and CO_2 percentage was studied and $K_{G_a}a_v$. The mass transfer coefficient was calculated using equation (3.14).

$$K_{G_a}a_v = \left(\frac{G}{P(y_{A,G} - y_A{}^*}\right)\left(\frac{dY_{A,G}}{dZ}\right) \qquad (3.14)$$

where $y_{A,G}$ is the mole fraction of CO_2 in the gas phase (mol/mol), y_A^* is the equilibrium mole fraction of CO_2, Z is column height (m), G is the gas flowrate (cm^3/s), and P is system pressure (Pa).

3.3.3.3 Liquid holdup

The liquid holdup was measured for Dixon rings $^1/_4$ and $^5/_8$ in using the tracer method. The method was conducted using a sodium chloride (NaCl) tracer and a conductivity meter (RS Pro Conductivity Meter, 1238777). The average residence time (τ) was calculated as a function of the conductivity values as shown in equations (3.15) and (3.16). Finally, the average liquid holdup was calculated as a function of τ, as shown in equation (3.17).

$$E(t) = \frac{C(t)}{\int_0^\infty C(t)dt} \quad (3.15)$$

$$\tau = \int_0^\infty t.\,E(t)\,dt \quad (3.16)$$

$$h_l = \frac{\tau.\,L}{V} \quad (3.17)$$

where C is the conductivity ($mS.cm^{-1}$), E(t) residence time distribution (-), τ average residence time (s), V volume (m^3), h_l is the average liquid holdup (-), and L is the liquid flowrate ($m^3.s^{-1}$).

4 Chapter 4: Sol-gel alumina coating of wired mesh packing

In this part, a sol-gel method was studied for coating Dixon rings. A parametric study was investigated to determine the effect of the starting ratios of water and Al on the coating thickness and adhesiveness. It was essential to allow the hydrolysis and the condensation to work in tandem during the mixing, affecting the production of hydroxides, molecular mass and thus the sol-gel solution viscosity. Aged solutions are anticipated to encounter an increase in viscosity owing to a change in the morphology of the cross-linking polymers, leading the boundary conditions that reduce the gelation to be investigated [67]. Herein, the peptization and ageing kinetics were first investigated, and the results helped characterize the coating properties when the starting solution contents (i.e., acid, water, alumina and the binder) were varied.

4.1 Sol-gel kinetics

The peptization and ageing processes are competitive since the kinetics of changes in surface charges are strongly affected by the initial coating parameters. Herein, effects of coating parameters (i.e. HCl content, water content, and ageing time) on the kinetics of peptization were investigated for an extended mixing time of one week.

4.1.1 HCl content

Figure 4.1 shows that the coating load per surface area increased initially for both Al/HCl ratios (0.17 and 0.25 (mol/mol)) until it reached a maximum value of approximately 1.301 mg/cm^2 after 96 h. Further increase of mixing produces the similar coating load.

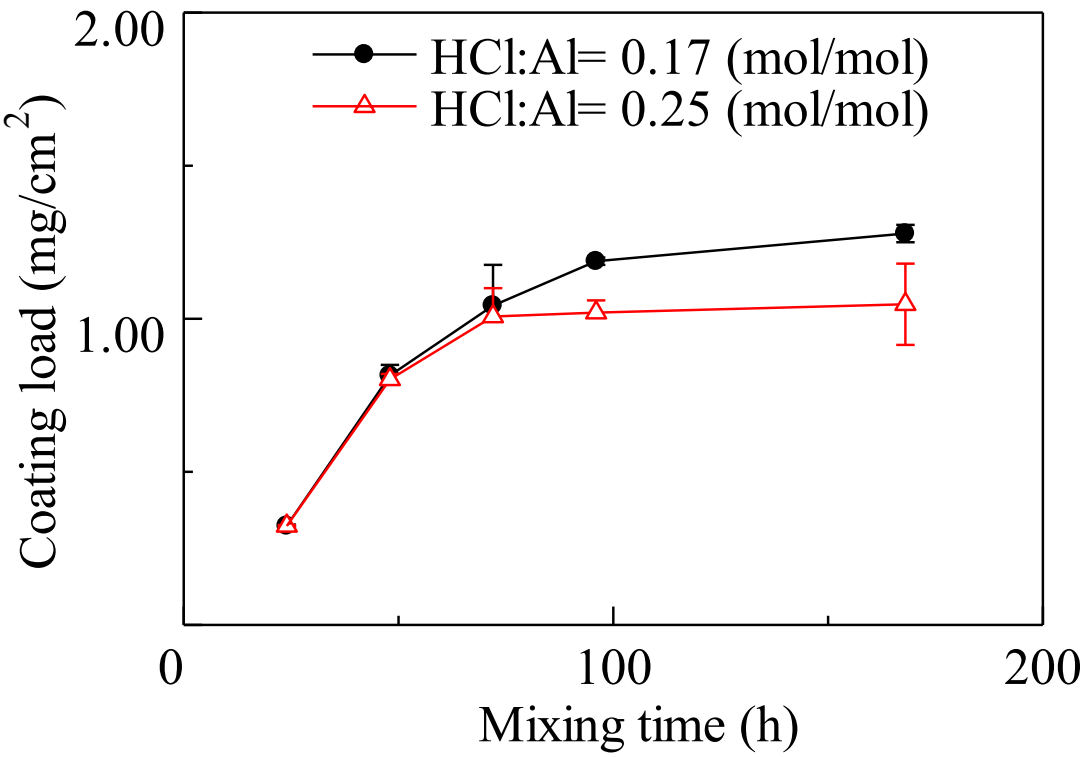

Figure 4.1: Effect of mixing time on the coating load. Coating parameters: Al/H_2O = 0.01 (mol/mol), aging time = 168 h, calcination temperature = 773 K

The increase in the load is explained by the deflocculation of alumina particles, as a result of an increase in the surface charge, moving away from the isoelectric point of the hydrolysed alumina colloid reducing the agglomeration kinetic rate of particles [193]. The load stabilised due to the pacification of changes of the particle charges under the effect of the shear forces. Therefore, a fine coating was produced when the mixing took place for 24 h, as shown in Figure 4.2. After 96 h, the mixtures were transparent, and no particulates were visually observed. The image by optical microscope **(**Figure 4.2**)** depicted uniformly spread films over Dixon rings with a thickness of around 20 µm.

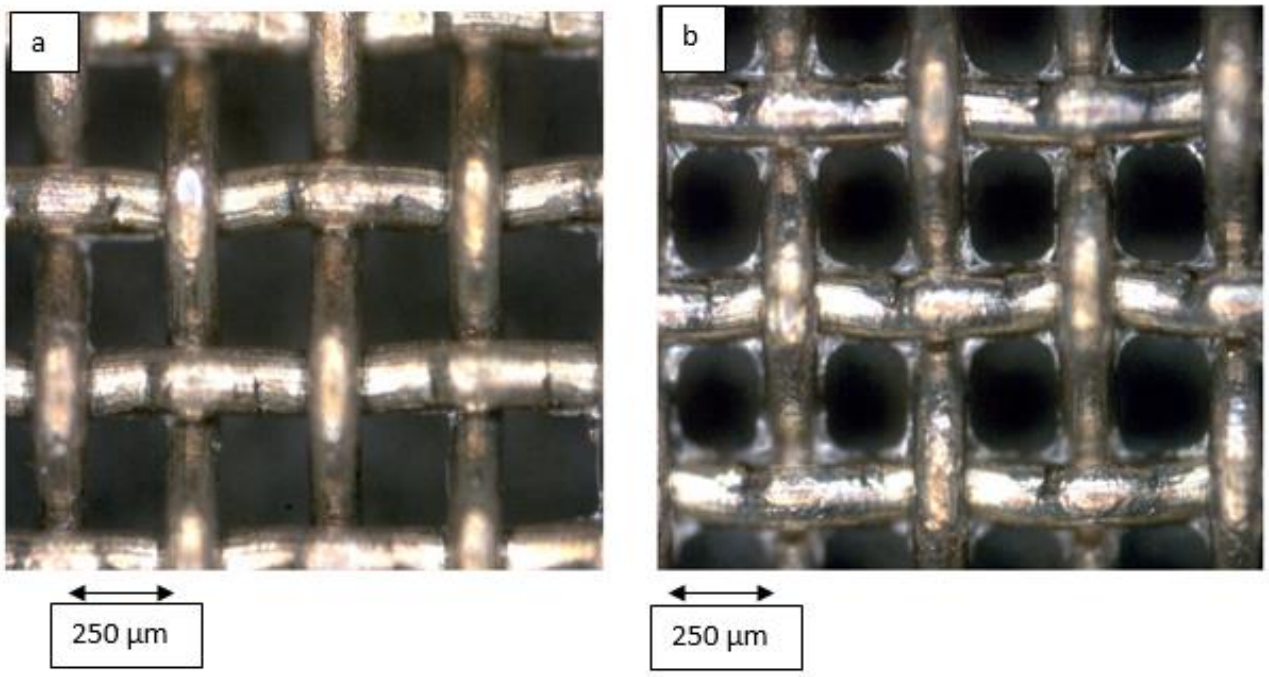

Figure 4.2: Optical micrograph (10X) of coated Dixon ring with: (a) mixing time = 24 h and (b) mixing time = 96 h. Coating parameters: HCl/Al = 0.25 (mol/mol), Al/H_2O = 0.01 (mol/mol), aging time = 168 h and calcination temperature = 773 K

4.1.2 Water content

The coating loading for Al/H_2O = 0.01 and 0.013 (mol/mol) is shown for a range of mixing time, as shown in Figure 4.3. The trends of the coating loading is similar for Al/H_2O = 0.01 and 0.013 (mol/mol). The load kept increasing with the mixing time, until it became constant after 96 h. The ratio of Al/H_2O of 0.01 (mol/mol) demonstrated a steady increase in the load after 48 h and stabilization after 96 h. The ratio of Al/H_2O of 0.013 however demonstrated a significant increase in the load after 48 h (load of 1.41 mg/cm^2) and stabilisation after 96 h. These results reflect the level of dispersion of hydroxyl bonds, the randomness in the surface charges and thus mobility of the particles in the solution [58].

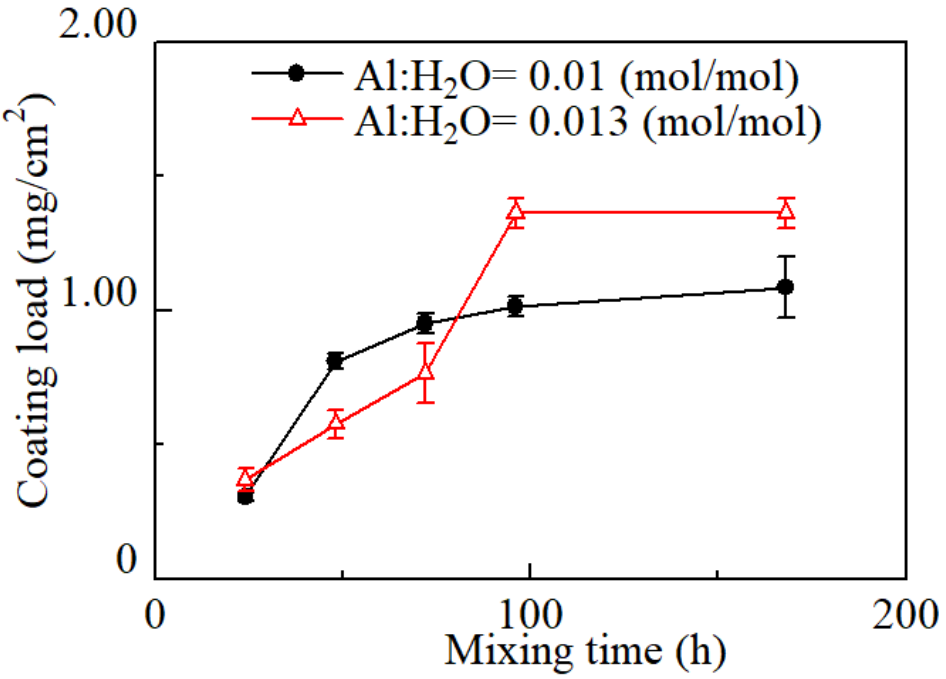

Figure 4.3: Effect of mixing time on the coating load. Coating parameters: HCl/Al = 0.25 (mol/mol) aging time = 168 h and calcination temperature = 773 K

4.1.3 Ageing time

The previous investigations showed that 96 h of mixing was enough to stabilise the coating load (section 3.1), and therefore this time was used to understand the effect of time on ageing. As expected, the general trends in Figure 4.4 and Figure 4.5 show that the coating load increased with the ageing time, confirming the development of an intertwined polymeric network. The measurements were extended to the course of 96 h, where no difference in load change was found. A uniformly spread and adhesive coating was achieved at HCl/Al = 0.25 (mol/mol) and Al/H_2O = 0.01 (mol/mol) after 48 h of ageing.

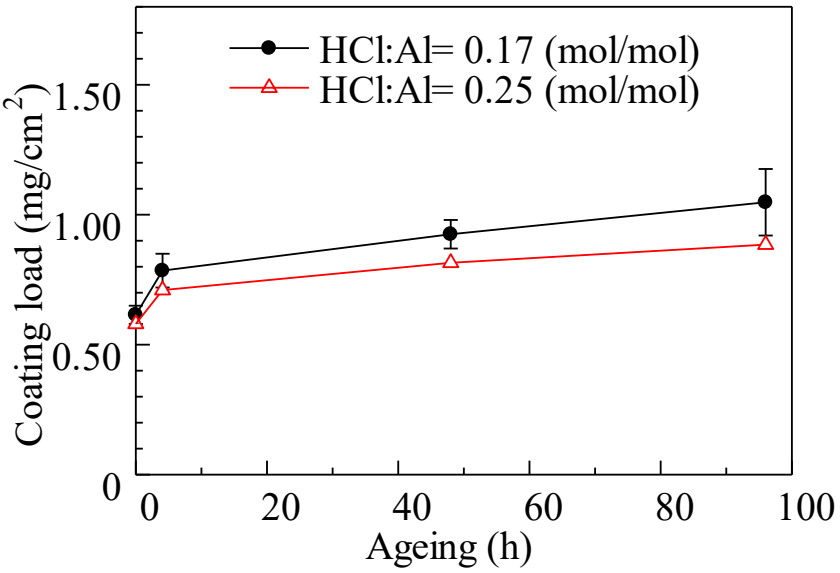

Figure 4.4: Effect of ageing time on the coating load. Coating parameters: Al/H_2O = 0.01 (mol/mol), mixing time = 93 h and calcination temperature = 773 K

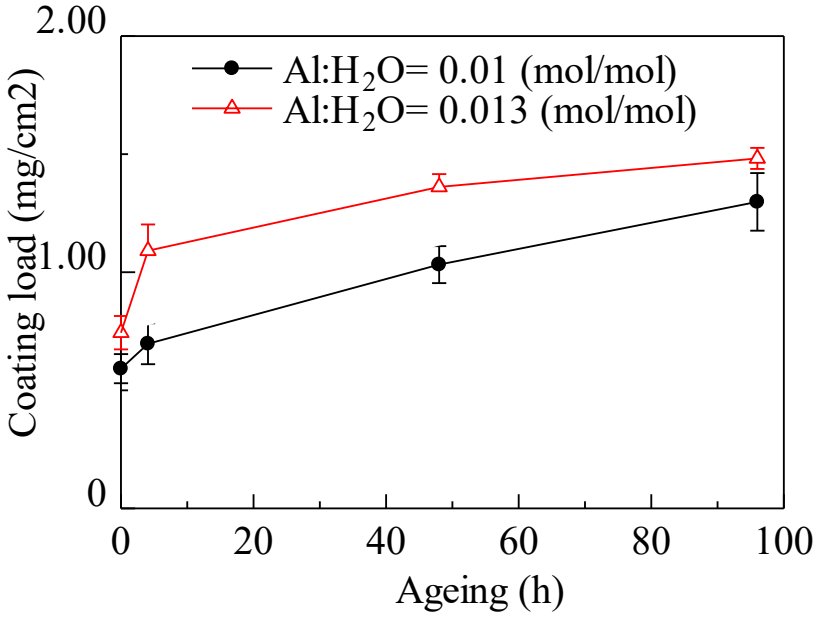

Figure 4.5: Effect of ageing time on the coating load. Coating parameters: HCl/Al = 0.25 (mol/mol) and mixing time = 96 h and calcination temperature = 773 K

4.2 Effect of the starting composition on coating properties

The steady properties of the coating after 96 h of perpetization time and 48 h of ageing were investigated by varying the starting composition of the coating. Finding the adequate starting composition is pertinent to the morphology of the coating because the rate and extent of the hydrolysis and condensation reactions are essentially driven by these ratios [67]. The stability of the prepared sol-gel solutions was determined based on its opacity to transparency range and the formation of agglomerates after drying the coated Dixon rings.

4.2.1 Effect of HCl content in the starting mixture

Strong acid (HCl) was added in order to reduce the heterogeneity level in the mixtures and give better control of the sol formation. The acid itself did not take part in the reaction but modified the properties of the mixture, by promoting changes in particles charges and thus the relevant particle sizes. Figure 4.6 shows the coating load and viscosity of the sol mixture as a function of the acid concentration in the starting mixture. The coating load was constant until it mounted at HCl/Al = 0.33 (mol/mol) in a similar way to the trends described in Yoldas [194]. At the HCl/Al range from 0.13 to 0.25 (mol/mol), transparent mixtures were produced, indicating a good dispersion. The viscosity was almost constant at 0.0035 Pa.s until it increased to a significant value of 0.025 Pa.s for HCl/Al = 0.33 (mol/mol), confirming the development of the gelation process, led by the formation of hydrogen bonding between the surface hydroxyl groups as well as the building of the loose polymeric 3D networks between the particles [39].

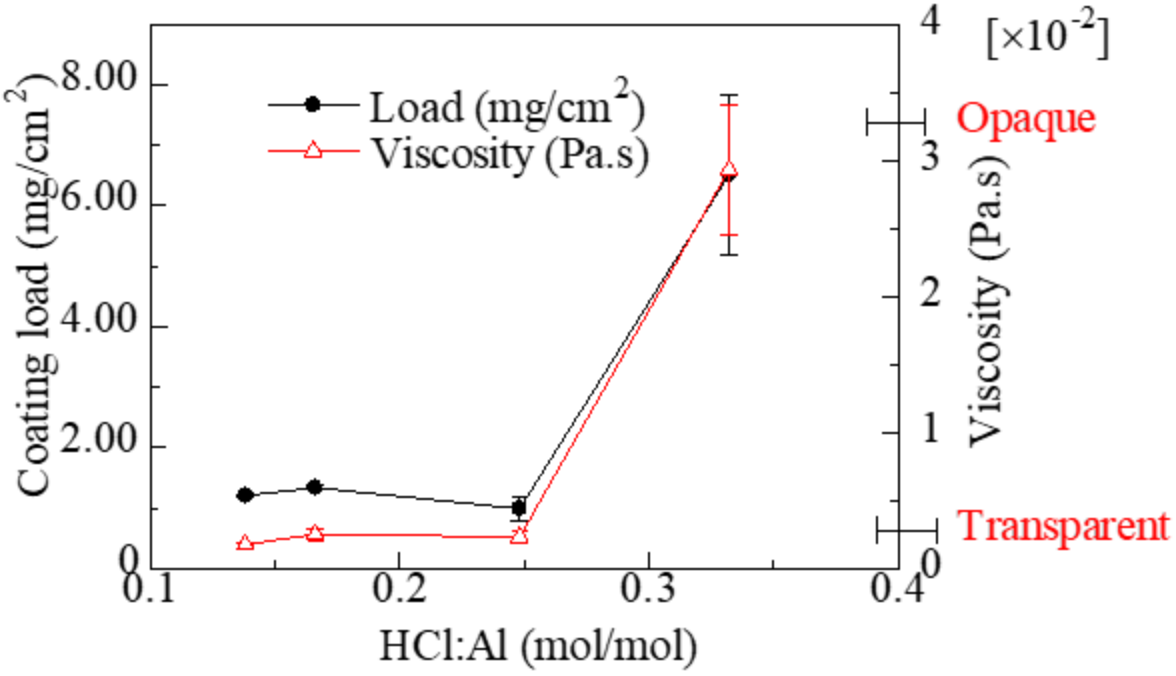

Figure 4.6: The influence of HCl/Al ratio in the starting mixture on: coating load and viscosity. Coating parameters: Al/H_2O = 0.01 (mol/mol), mixing time = 96 h, aging time = 48 h and calcination temperature = 773 K.

The correlation between the viscosity of the solution and the coating load pointed out the key role of the flow behaviour of the solution in development of the coating on Dixon substrate. The results of the rheologic measurements are useful to explain the profiles of coating adhesiveness when the coated Dixon rings were assessed by the ultrasonic adhesion test for a period of 10 min, as shown in Figure 4.7. A HCl/Al ratio of 0.25 (mol/mol) provided a load drop that was ranging from 19-30%. A HCl/Al ratio of 0.33 (mol/mol) however demonstrated a major drop (ca. 90%) of the original load. The ratio of HCl/Al was then considered for the rest of the work as it demonstrated a good adhesiveness of the coating.

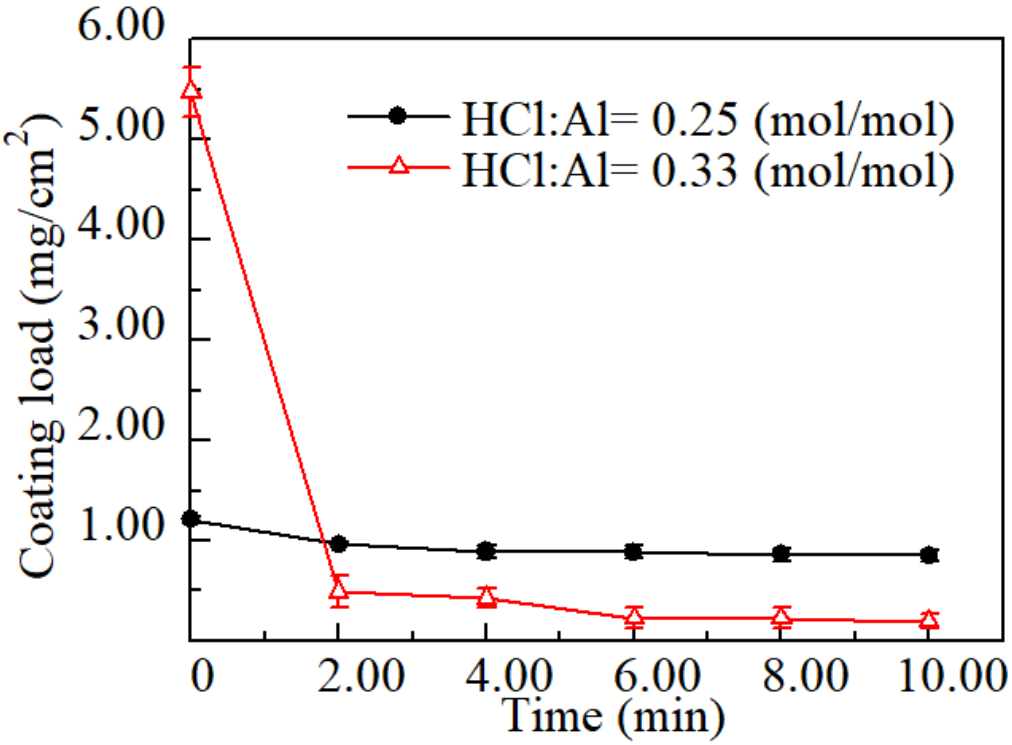

Figure 4.7: Ultrasonic adhesiveness test – influence of ultrasound bath time on the coating load. Coating parameters: Al/H_2O = 0.01 (mol/mol), mixing time = 96 h, aging time = 48 h and calcination temperature = 773 K.

4.2.2 Effect of Al content in the starting mixture

As shown in Figure 4.8, the coating load and the sol-gel viscosity increased monotonically by increasing the alkoxide concentration, stabilized at Al/H_2O = 0.017 (mol/mol), and then increased at Al/H_2O = 0.02 (mol/mol). A similar trend was observed by Valentini *et al.* [39] and was discussed by the wetting potential of the substrate. This is confirmed by the viscosity profiles, which followed similar trend to those of the coating load (i.e. an increase from 0.0035 to 0.018 Pa.s when Al/H_2O ratio was increased from 0.014 to 0.02 (mol/mol), demonstrating role of water in the hydrolysis and polycondensation process.

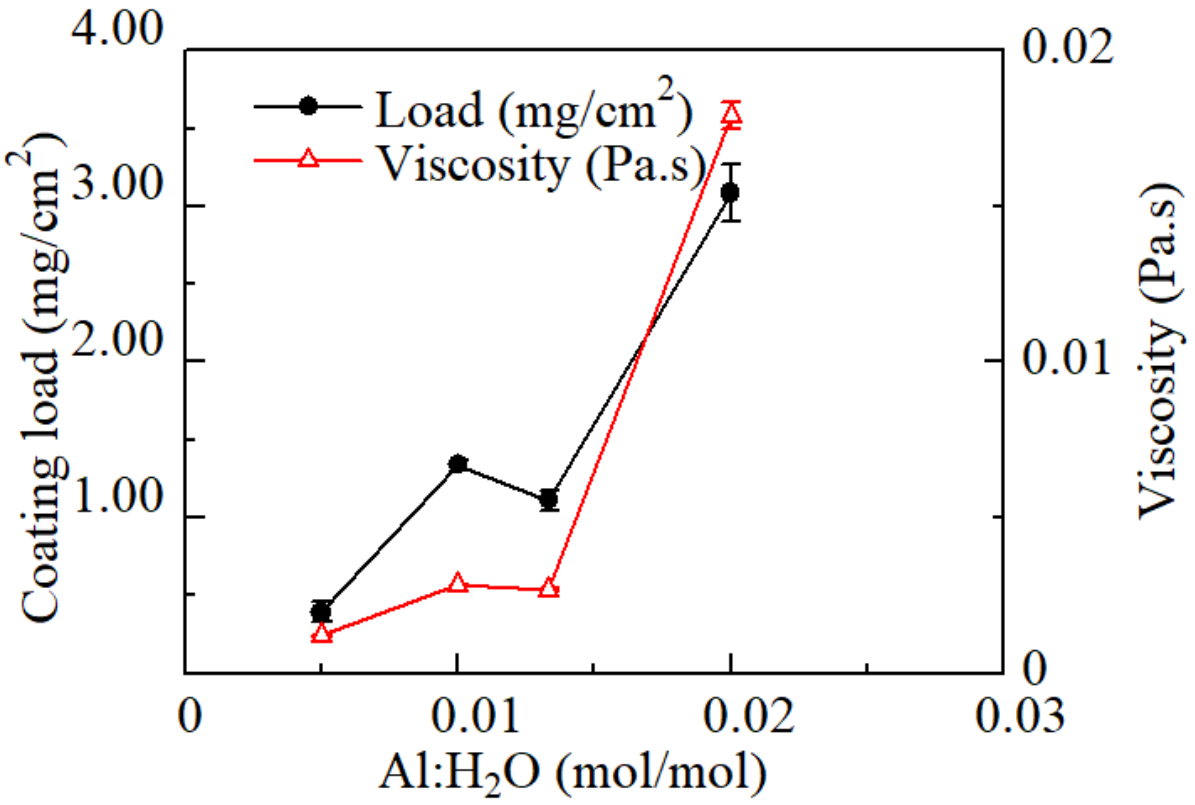

Figure 4.8: Influence of Al/H_2O ratio in the starting mixture on: the coating load and viscosity. Coating parameters: HCl/Al = 0.021 (mol/mol), mixing time = 96 h, aging time = 48 h and calcination temperature = 773 K.

Figure 4.9 shows the profiles of the coating load under ultrasound tests for 0.02 and 0.01 mol/mol water content, respectively. The former water content provided poor adhesiveness since about 80% of the coating load was lost after 10 min. The lack of dispersion in water limited the formation of OH groups. The formation of soluble oxo-ligands in water was then inhibited by the development of repulsive forces, reducing of the electric double layer and leading to the agglomeration of the particles, and thus a poor adhesion to the substrate. When the Al/H_2O ratio was reduced to 0.01 (mol/mol), only 18-23% of the load was lost under the ultrasonic test, showing a relatively good dispersion of alumina particles, which was an indication of arranged particles in the 3D polymeric network. The ratio of Al/H_2O = 0.01 (mol/mol) was then chosen for the following study.

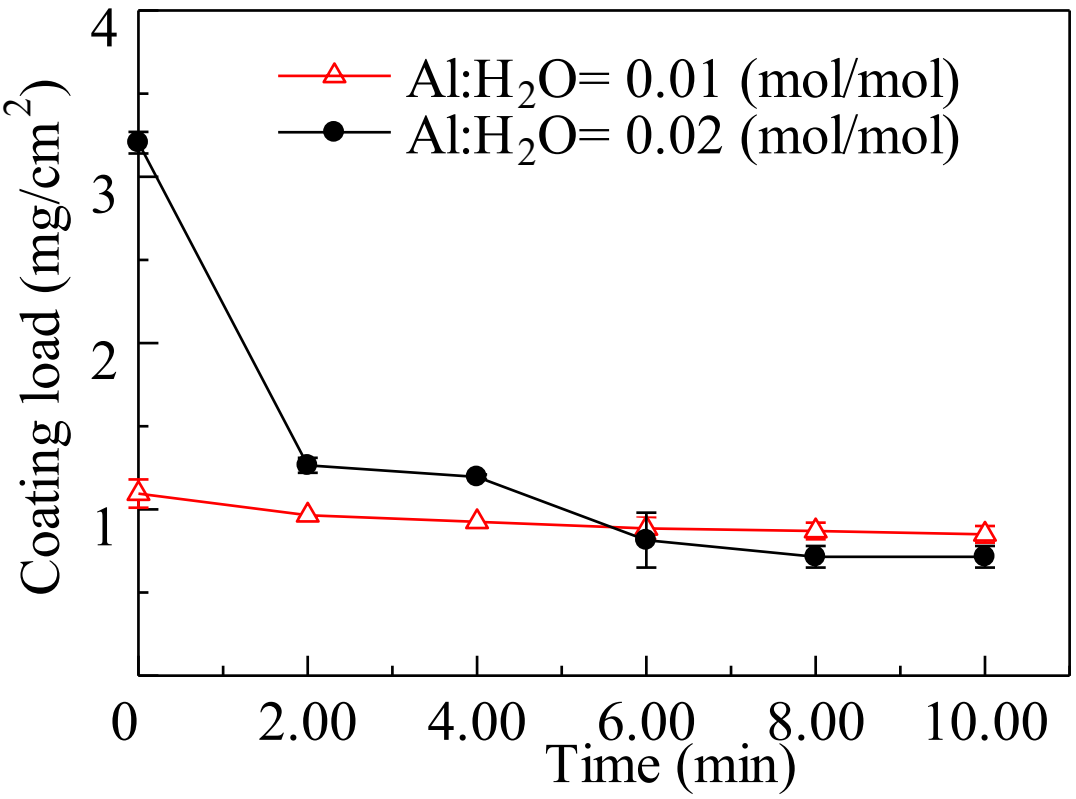

Figure 4.9: Ultrasonic adhesiveness test – influence of ultrasound bath time on the coating load. Coating parameters: HCl/Al = 0.25 (mol/mol), mixing time = 96 h, aging time = 48 h and calcination temperature = 773 K.

4.3 Effect of the PEI as binder

Polymeric binders are known for improving adhesion and reducing the cracks during the deposition process [25]. Figure 4.10 shows the effect of PEI as binder on the coating load. The addition of binder did not have any effect on the coating load for concentrations below 1.05 g/L. Conversely, the deposition was enhanced steadily from 1.05 g/L to 2.1 g/L, whilst the further increase of the binder concentration (more than 2.1 g/L) resulted in a sharp increase of the coating load.

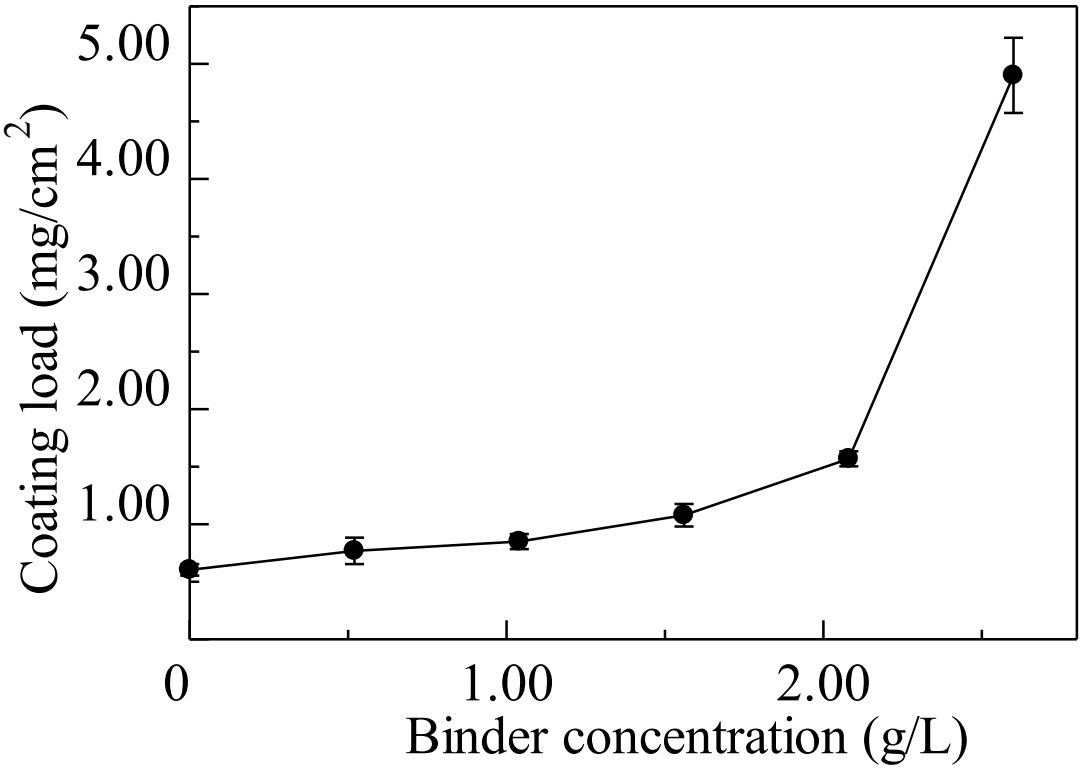

Figure 4.10: Effect of binder concentration on the coating load. Coating parameters: Al/H_2O = 0.01 (mol/mol), HCl/Al = 0.25 (mol/mol), mixing time = 96 h, ageing time = 48 h and calcination temperature = 773 K.

Optical micrographs presented in Figure 4.11 revealed cracks in the coating and filled openings of the Dixon rings for concentration of the PEI higher than 2.6 g/L. This could be explained by the high surface positive charge that would have promoted the flocculation of alumina particles and reduced its stability [26]. Conversely, the binder concentration of 2.1 g/L resulted in the highest load whilst it kept a good surface uniformity as shown in the micrographs of Figure 4.11.

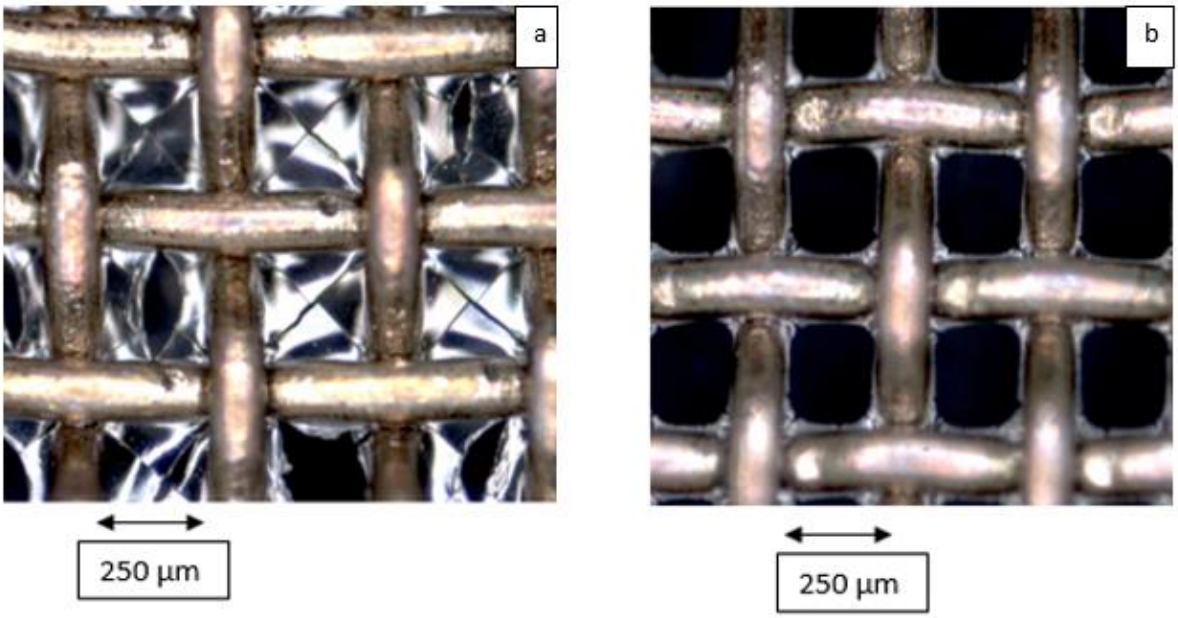

Figure 4.11: Optical micrograph (10X) of coated Dixon ring with using PEI concentration of: (a) 2.6 g/L and (b) 2.08 g/L. Coating parameters: HCl/Al = 0.25 (mol/mol), Al/H_2O = 0.01 (mol/mol), mixing time = 96 h, aging time = 48 h and calcination temperature = 773 K.

The binder was then effective in reducing the surface charges (i.e. particularly relevant to hydroxyl functional groups that are responsible for the attachment of the film to the substrate) and thus absorbing the effect of capillary forces onto the surfaces of the alumina particles. The adhesion was improved compared to Dixon rings coated with no binder (i.e. the 12-15% of the initial mass was lost when subjected for 10 mins in the ultrasound adhesive test, as shown in Figure 4.12, whilst the samples prepared without PEI lost 19-30%).

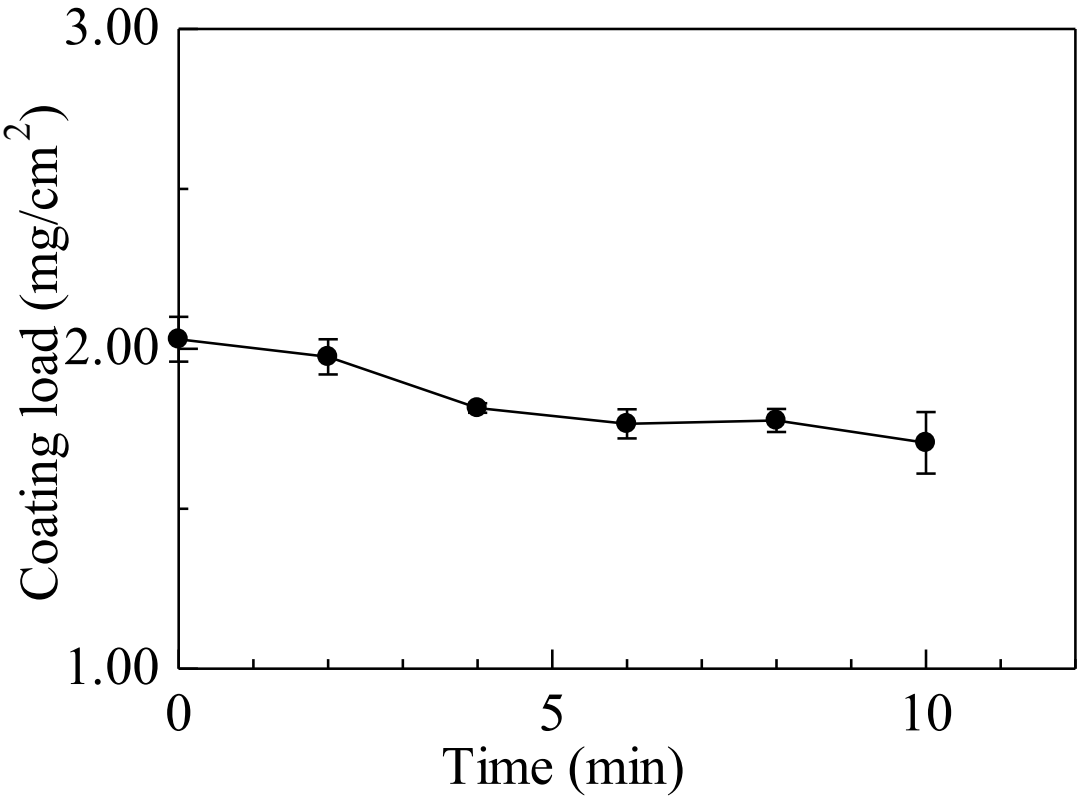

Figure 4.12: The coating adhesion in ultrasound bath tests with the addition of PEI concentration = 2.1 (g/L). Coating parameters: Al/H_2O = 0.01 (mol/mol), HCl/Al = 0.25 (mol/mol), mixing time = 96 h, ageing time = 48 h and calcination temperature = 773 K.

4.4 Effect of the coating cycles

A multiple cycle deposition procedure for Dixon rings was probed in order to prepare a coating of controlled thickness and loading properties. When the same procedure was followed for each deposition, a positive correlation between the alumina coating properties and the number of depositions was obtained as demonstrated in Figure 4.13 and depicted in Figure 4.14. The coating load increased from 1.13 mg/cm^2 to 1.84 mg/cm^2 after four depositions. The error bands shown in Figure 4.13 the standard deviation of the coating thickness.

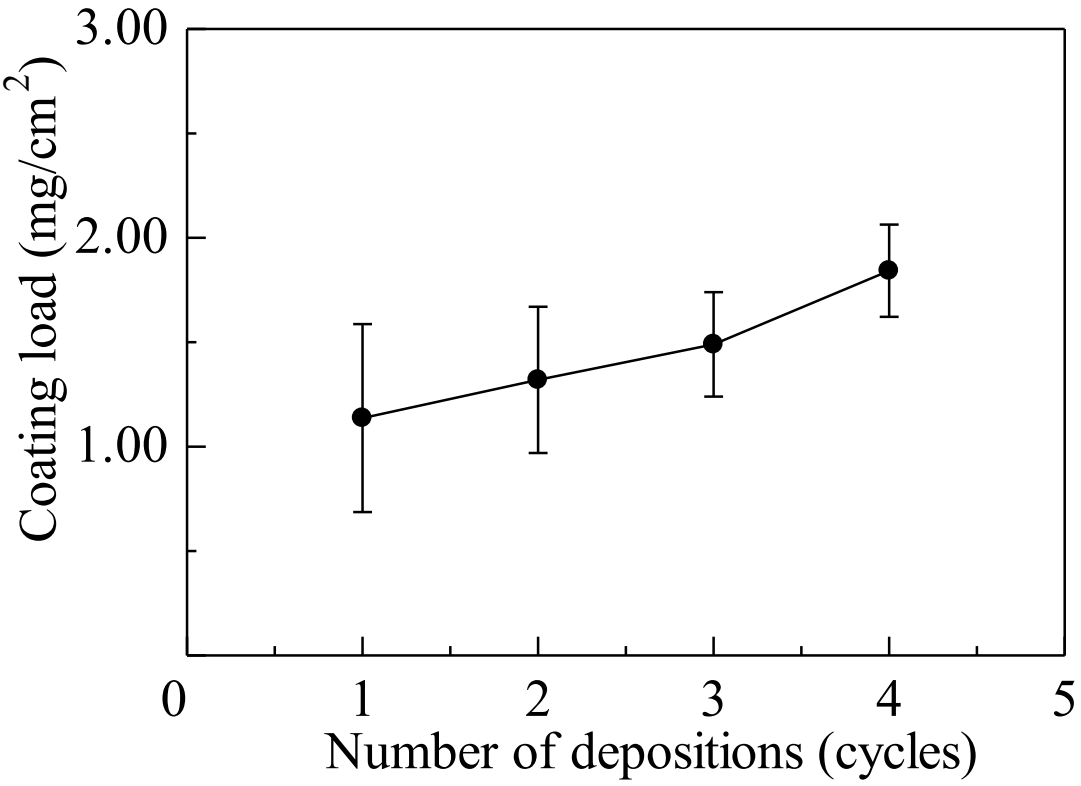

Figure 4.13: Coating load vs deposition cycles for Dixon rings. Coating parameters: Al/H_2O = 0.01 (mol/mol), HCl/Al = 0.25 (mol/mol), mixing time = 96 h, ageing time = 48 h and calcination temperature = 773 K.

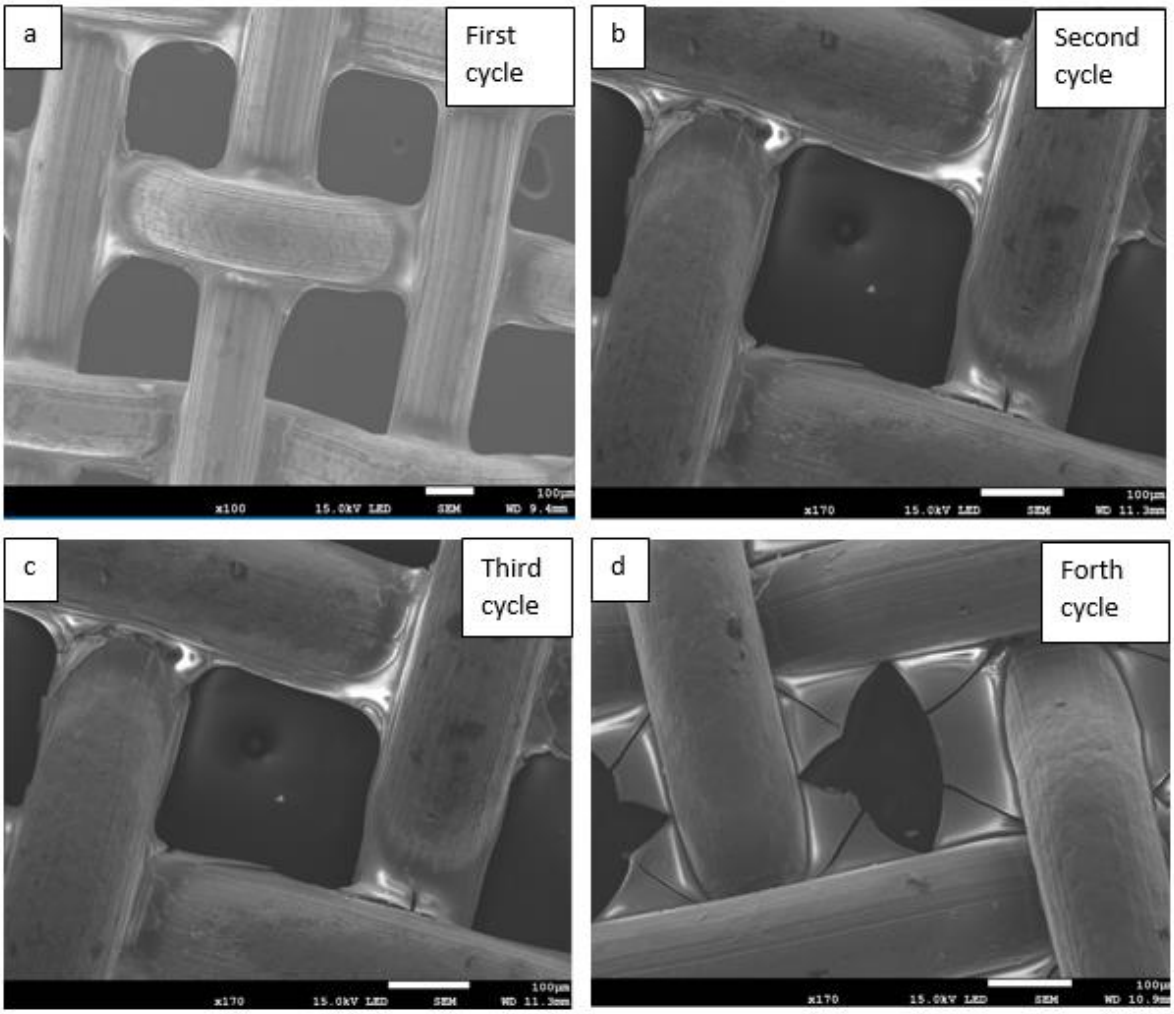

Figure 4.14. Coupled SEM-EDS results on Dixon ring coated with: (a) one, (b) two, c) three, and d) four deposition cycles. Coating parameters: Al/H_2O = 0.01 (mol/mol), HCl/Al = 0.25 (mol/mol), mixing time = 96 h, ageing time = 48 h and calcination temperature = 773 K.

Ultrasonic adhesive tests, as shown in Figure 4.15, demonstrated that the multiple depositions reduced the adhesion of the coating to the substrate.

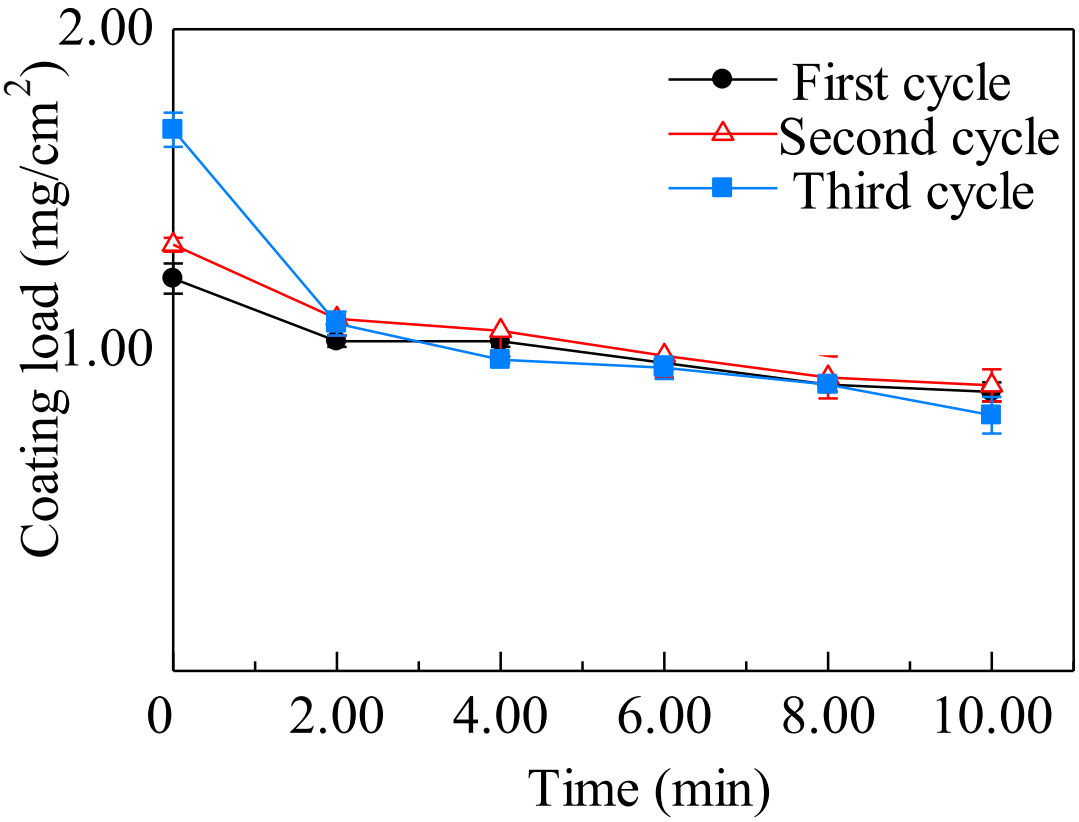

Figure 4.15: The coating adhesion in ultrasound bath tests for multiple depositions. Coating parameters: Al/H_2O = 0.01 (mol/mol), HCl/Al = 0.25 (mol/mol), mixing time = 96 h, ageing time = 48 h and calcination temperature = 773 K.

For the first, second and third deposition cycles, the coating mass decreased by 19.8%, 31.7% and 61.4%, respectively. After the fourth deposition cycle, the coating lost its homogeneity and multiple cracks were formed (Figure 4.14), whilst the first three cycles had similar morphology and a slight increase in the load (Figure 4.13). The drastic increase in the coating load reflects a change in the surface roughness. Such behaviour could be explained by the effects of thermo-mechanical stresses that could be developed during the thermal treatment of the coating, whilst a potential chemical effect of hydroxyl groups should not be ignored.

4.5 The morphology of the coating

4.5.1 Coating distribution over Dixon rings

The images from the SEM for Dixon rings (Figure 4.16) showed that the coating was more effective around the interstitial area in the vicinity of the pore openings and intersections of the wires but was less effective on the convex area of the wires. This can be explained by the wetting behaviour of the Dixon rings by the liquid precursor, which favoured the opening pore area by capillary wetting.

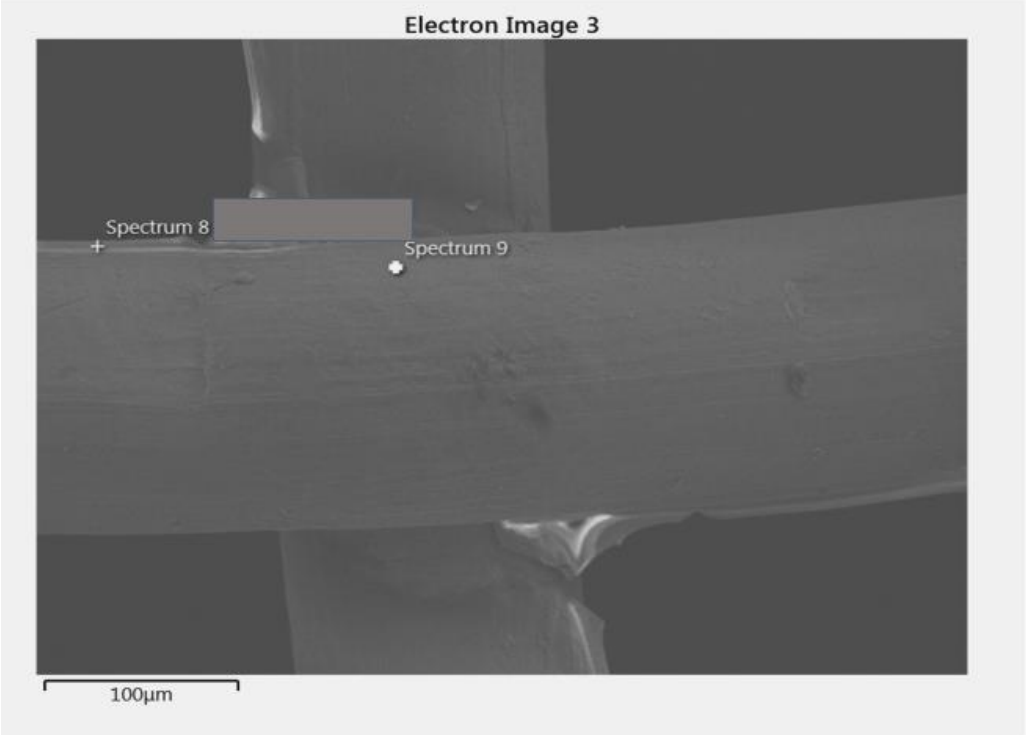

Figure 4.16: SEM-image of a coated Dixon ring, coating parameters: Al/H_2O = 0.01 (mol/mol), HCl/Al = 0.25 (mol/mol), mixing time = 96 h, ageing time = 48 h and calcination temperature = 773 K.

EDS tests were conducted on the same sample by selecting two arbitrary points, one near the opening vicinity, where the coating is concentrated, and the other on the wire, where the coating is sparse, as shown in Figure 4.17 and Figure 4.18 - spectra 8 and 9 show 42.1 % Al and 51 % for O in the vicinity of the pores and 11.4 % Al and 20.2% O on the wire, respectively.

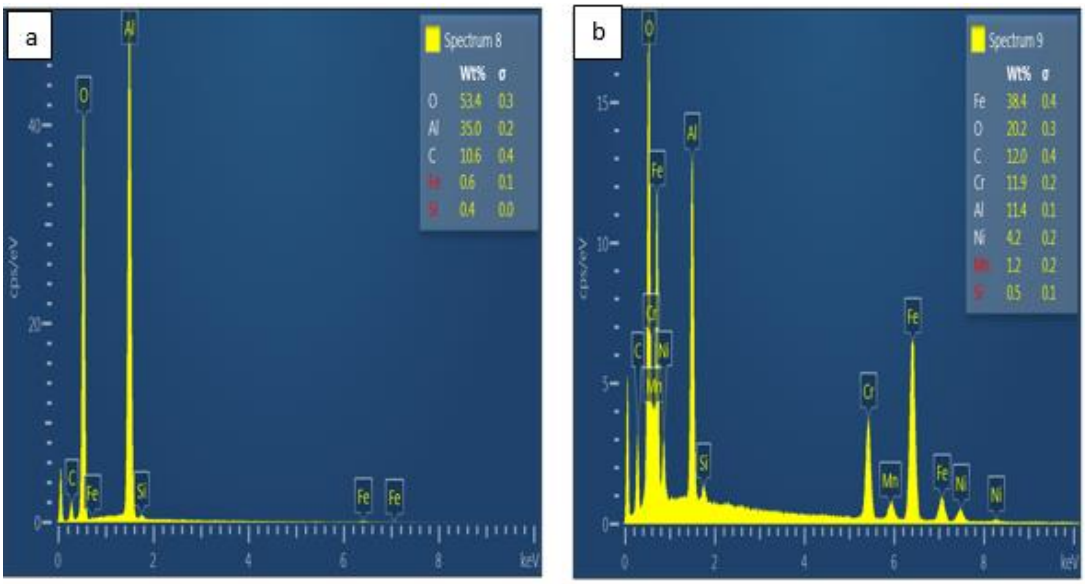

Figure 4.17: The EDS spectrum for the local points (a) 8 and (b) 9 for the sample in Figure 4.16

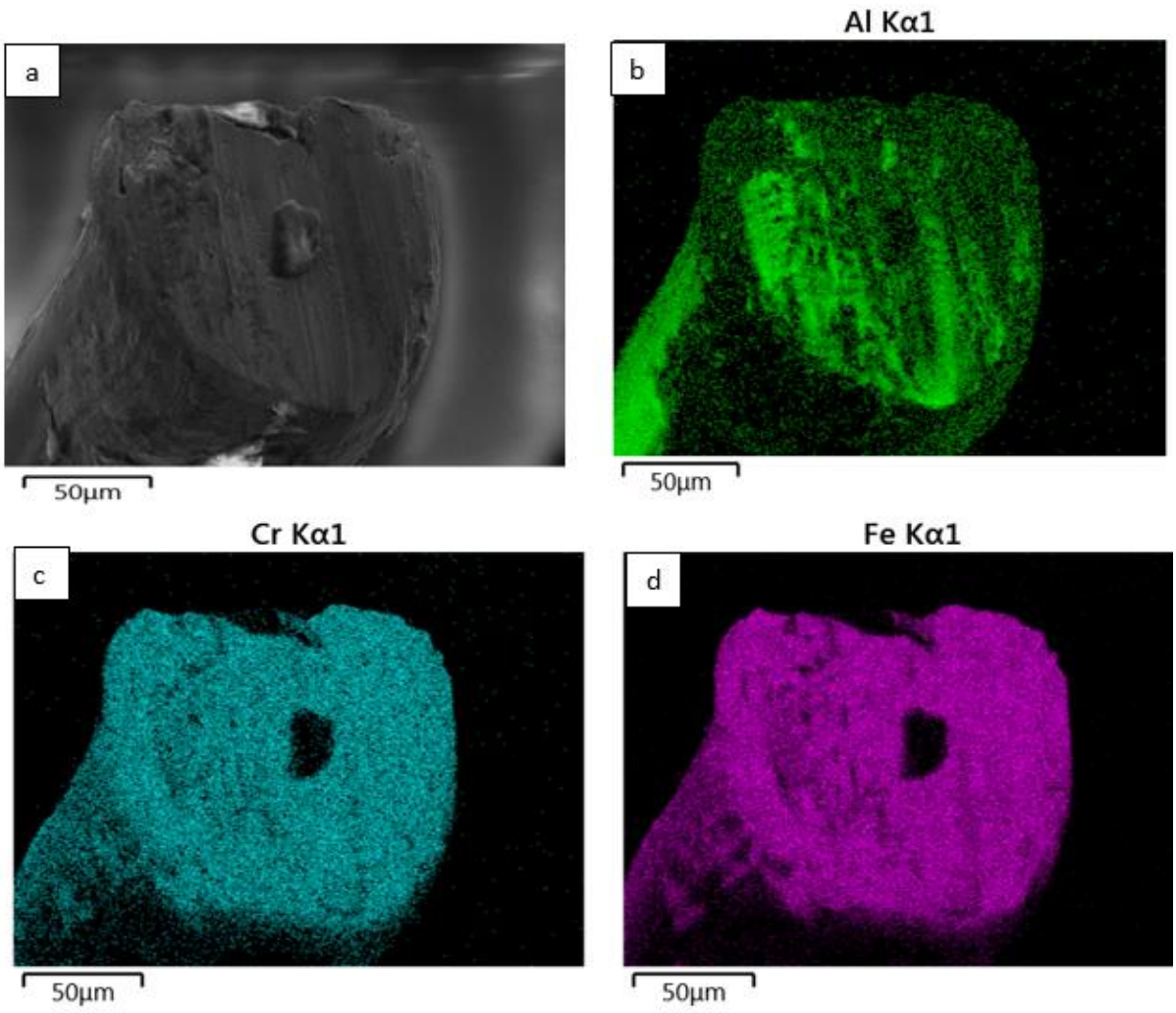

Figure 4.18: SEM image of the wire after the cut (a), coupled SEM-EDS mapping (b) Al (c) Cr (d) Fe results for a cut through a coated Dixon ring. Coating parameters: HCl/Al= 0.25 (mol /mol), Al/H_2O= 0.01 (mol /mol), mixing time= 96 h, ageing time= 48 h and calcination temperature= 773 K.

In order to check if any interfacial layers between the coating and substrate was formed by the chemical bonds, a cross-section cut of a coated Dixon ring was carried out to assess potential diffusion of alumina into the wires. Figure 4.18 (b) shows some traces of alumina within the wires but distribution at the boundary substrate-coating was not uniform (i.e. unlike Cr and Fe in Figure 4.18 (c) and (d), respectively). This shows that the diffusion or migration of Al to the substrate was a function of the coating distribution of the mesh-wire (i.e. it was concentrated particularly in locations in the vicinity of the wire's cross-section. The adhesion of the coating was therefore mainly driven by the chemical bonding at negligible mass transfer diffusion into the substrate.

4.5.2 Effect of calcination temperature

The effect of calcination temperature on the surface area and porosity of alumina was investigated. The results are illustrated in Table 4.1. Alumina has a mesoporous structure with strong contribution of micropores to the overall surface structure. The surface area of the sample calcined at 773 K (300.7 m^2/g) was higher than the one calcined at 1073 K (245.6 m^2/g). The decrease of the surface area correlates well with the increase of the pores sizes, particularly at temperatures higher than 773 K [25].

Table 4.1: The properties of alumina calcined at 773 K and 1073 K.

Temperature (K)	**Surface area (m^2/g)**	**Average pore diameter (nm)**	**Pore volume (cm^3/g)**
773	300.7	12.4	0.41
1073	245.6	12.6	0.46

The SEM image (Figure 4.19) shows the effect of the calcination temperature at 773 K, 1073 K and 1273 K on the morphology of the coating. Similar structure, glass-like, is observed at 773 K and 1073 K calcination temperature, which confirm the surface properties in Table 4.1, whilst at 1273 K, some particles agglomerated into aggregates are observed.

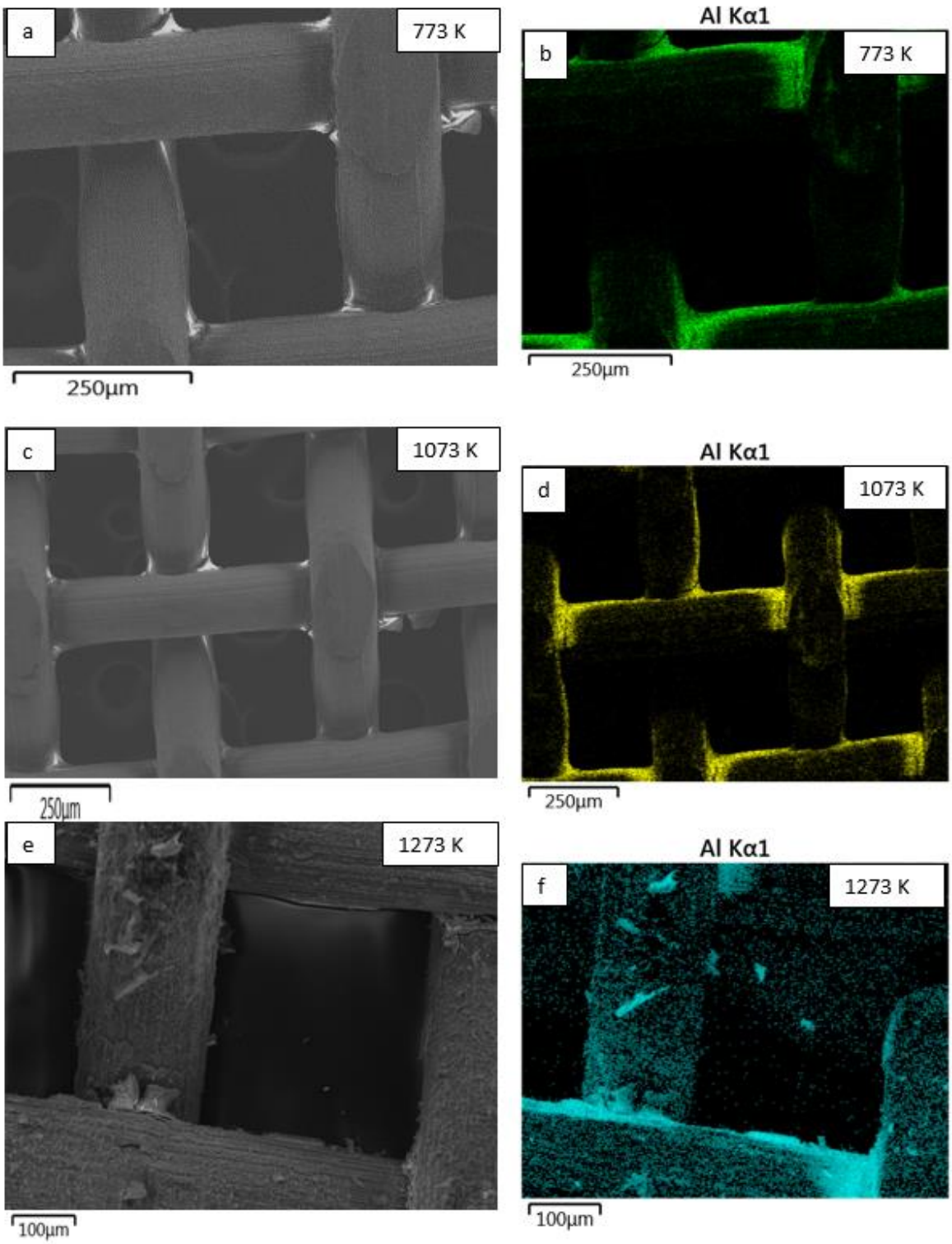

Figure 4.19: SEM images (a, c and e) and EDS images of Al distribution (b, d and f) of calcined coating. Calcination temperature: (a, b) at 773 K, (c, d) at 1073 K and (e, f) at 1273 K. Coating parameters: Al/H_2O = 0.01 (mol/mol), HCl/Al = 0.25 (mol/mol), mixing time = 96 h and ageing time = 48 h.

The alumina particles grew due to the increasing nucleation rate, and their migration promoted the surface thickness [15]. In addition, few cracks were observed at this temperature, which might be attributed to the residual stress due to the difference between the thermal expansion coefficient of the metal and the coating and to the reduction of the density of hydroxyl groups [27]. The coating load was measured for all temperatures and was the same, demonstrating a good thermal resistance up to 1273 K.

In this section, Dixon rings packing were coated with alumina using a sol-gel method. This method includes multiple steps: pretreatment, sol preparation, dipping, and calcination. The coating was characterised using visual methods such as optical microscopy and SEM. Adhesive tests were conducted, such as ultrasonic and temperature resistance tests. The coating was found to have a uniform thickness and excellent adhesive properties. The next step was determining if the alumina coating on Dixon rings affects the hydrodynamic properties such as the wetting efficiency and liquid holdup.

The next step was scaling up the procedure to produce multiple coated Dixon rings using the dip-coater. The section holding a single Dixon ring was replaced with a part that had several 15 elements of the Dixon rings attached. The dip-coating parameters such as the withdrawal speed, dipping speed, drying time, etc., were like the procedure used for a single element. The coating thickness and adhesiveness were excellent, like the single-element coating method described in section x. However, the procedure was very time-consuming, since each element needed to be attached separately to the holder.

5 Chapter 5: Tuning the wetting efficiency of wire mesh column: pore-scale flow analysis

In this section, the liquid flow over Dixon rings was studied microscopic using an imaging method and 3D modelling. The effect of surface properties was investigated by determining the interactions of the liquid with the uncoated and coated Dixon rings under a trickle flow regime. The wetting efficiency was determined on a local scale using VOF and Eulerian-Eulerian models which were validated using experiments conducted via imaging by a CCD camera. The liquid holdup and the effective surface area were calculated when the liquid velocity and contact angle were varied. The results from the 3D model were compared to results from literature for the liquid holdup and the effective surface area.

5.1 Model validation

5.1.1 Flow over uncoated Dixon rings

The dynamics of the capillary droplets on an uncoated stainless-steel Dixon ring at Weber number (W_e) of 0.23 at the nozzle and after collision with the Dixon ring wall are illustrated in Figure 5.1 (a-d) and (e-h) by a series of snapshots from laboratory experiments and Dixon rings cut used in simulations. The dynamics of the impact of the droplet over the Dixon ring were driven by competition of the inertial forces and the surface tension forces, in particular, the flow velocity, surface tension and Dixon ring surface roughness. During the impact and spreading of the capillary droplet, the inertial forces were converted into viscous dissipation forces, allowing the creation of new surfaces of the liquid for further spreading over the Dixon ring.

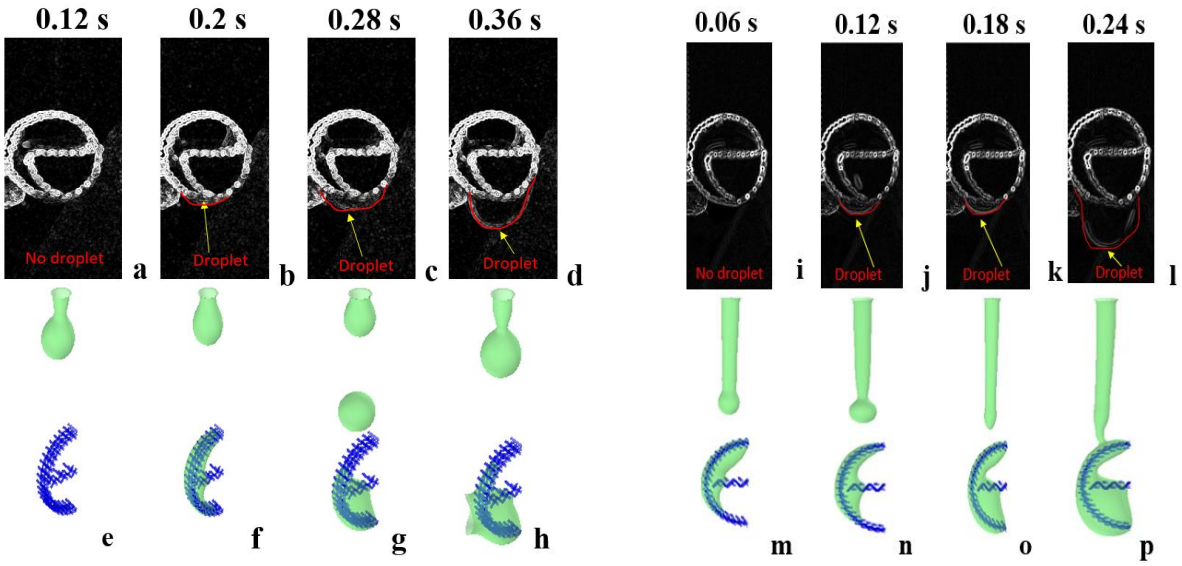

Figure 5.1: Flow pattern comparison between the experimental and Snapshots of the impact of droplets (a-h) and filaments (i-p) on uncoated stainless steel Dixon ring for W_e = 0.23 : (a-d) experiments, (e-h) simulation and for W_e = 0.64 : (i-l) experiments, (m-p) simulation.

The dropwise flow of water from the nozzle demonstrated the non-visco-elastic property of the flow and accumulated at the top part of the mesh openings for the uncoated rings. The droplets built up a liquid film and penetrated the grid by the formation of dripping drops inside the Dixon ring. The droplets were then obstructed by the horizontal grid at the centre of the ring at 0.2 s (Figure 5.1 (b)) but continued filling the bottom region of the Dixon ring (Figure 5.1 (c)). After 0.36 s, the bottom region became full and the liquid started to overflow through the sides at reduced velocity. This overflow led the droplets to reach the flooding conditions. The results from the model showed that the liquid was adhering to the ring until it reached the bottom section where the liquid was trapped and accumulated. The liquid film exhibited adherence to the uncoated ring, with no breakup and the thickness around the Dixon ring increased after each droplet until the liquid reached maximum value after four impact cycles and then detached at 0.36 s, as shown in Figure 5.1 (d). The CFD simulation (Figure 5.1 (e-h)) show dynamics of the impact of the droplets of a reasonable agreement with the experimental data. Both Figure 5.1 (b) and (f) of 0.2 s time snapshots show the droplet trapped inside the ring. These figures were improved by adding boundaries around the droplets to discriminate the flow pattern (red line). The experimental droplet was however mainly located above the horizontal grid (b) while the ring simulation shows a uniformly distributed droplet inside the ring (Figure 5.1(f)). The two snapshots at 28 s and 36 s

show the experimental droplet filling the bottom part of the ring and later accumulated underneath while the simulation droplets remained well adhered to the grid inside the ring. Overall, the flow patterns by the simulation appear to be built slightly faster, as they show the accumulated droplets being more developed. In conclusion, it is show that the water as a droplet or a jet went through the uncoated rings which illustrates the hydrophilic nature of the packing

When W_e was increased from 0.23 to 0.64, the same dynamics were observed as shown in Figure 5.1 (i-l) (i.e. experimental droplet accumulation above the horizontal grid vs. uniform distribution through the ring of the simulation in Figure 5.1 (m – p), accumulation of the experimental droplet at the bottom the ring vs. accumulation of simulation droplet inside the ring). Also, a continuous liquid stream occurred and fully developed at 0.24 s, as shown in Figure 5.1 (l and p). The liquid flow pattern from the experiments and the model reached a steady-state flow within a shorter time than that reached at W_e of 0.23.

5.2 Grid independence test and simulation validation

The complex geometry of Dixon rings made the implementation of structured meshes challenging. Therefore, unstructured grids of free tetrahedral elements were used for the fluid domains and triangular elements covered the surfaces. To ensure that the solution was independent of the size of the mesh used in the simulation, the grid independence (GR) test for different cell sizes was conducted. The properties of several meshes are presented in Table 5.1. The number of cells and the sizes of the elements that were used enabled the assessment of the resolution of the flow pattern.

When GR1 was tested, the liquid flow over Dixon rings did not change over time (Figure 5.2 (a–e)). As expected, GR1 results did not produce any liquid penetration through the Dixon rings. The refined mesh (i.e. GR2) is described in Figure 5.2 (f–j) illustrating a realistic pattern for the flowing liquid. Further increase in the number of elements (*i.e.* GR3) augmented the computational time with no clear discrepancies in the flow pattern observed, as shown in Figure 5.2 (k–o) and therefore GR2 was adopted for the simulation study. The computation time ranged from 672 to 840 h at W_e = 0.23 to 2.57.

The refined mesh domain (i.e. GR2) is described in Figure 5.3. This observation is confirmed by the trends of wetting efficiency with time illustrated in Table 5.2 where GR2 and GR3 demonstrated close performance. To ensure that the model replicates realistic flow, a segment of a larger sized Dixon ring was used for the simulation. The mesh used for this investigation, GR2-

1, had the same properties as GR2 except for the larger number of cells, as shown in Table 5.1. Figure 5.4 confirmed the trend observed in Figure 5.1, which were driven by a hydrophilic pattern, similar to the one produced using GR2.

Table 5.1: Mesh properties for the CFD model discretization.

Mesh type	Maximum element size (mm)	Minimum element size (mm)	Resolution of narrow regions (-)	Number of cells (cell)	Element size near Dixon rings wall (mm)
GR1	0.48	0.144	0.6	260798	0.06
GR2	0.322	0.096	0.7	586524	0.04
GR3	0.288	0.072	0.75	1008754	0.03
GR2-1	0.322	0.096	0.7	849542	0.05

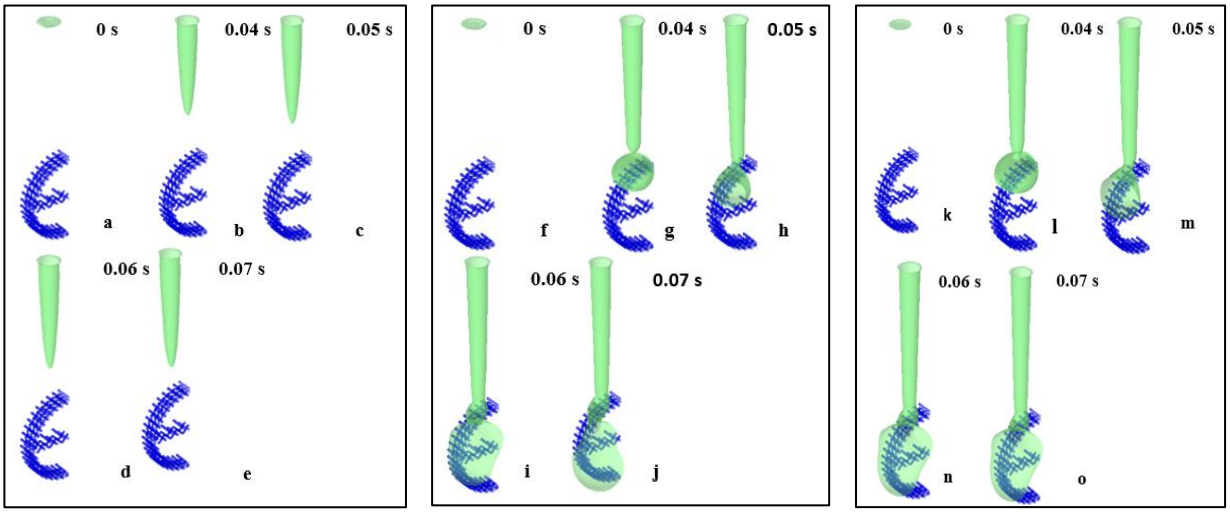

Figure 5.2: Flow pattern of VOF = 0.5 for uncoated Dixon rings using grid GR1 (a-e), GR2 (f-J) and GR3 (k-o) for W_e = 1.26 and θ = 105°

Table 5.2 shows the wetting efficiency against time for the coated Dixon rings for several mesh types. The wetting efficiency was initially 0 at t= 0 s. When the water droplet hit the Dixon rings at t= 0.04 to 0,07 s, it increases by a very small amount due to the hydrophobic nature of the coating.

Table 5.2: Quantitative comparison using the wetting efficiency against time (s) for several mesh types.

Mesh type	**t (s)**	**0.03**	**0.04**	**0.05**	**0.06**	**0.07**
GR1	Wetting efficiency (-)	0	0.002	0.02	0.033	0.045
GR2		0	0.037	0.027	0.04	0.049
GR3		0	0.038	0.027	0.042	0.047

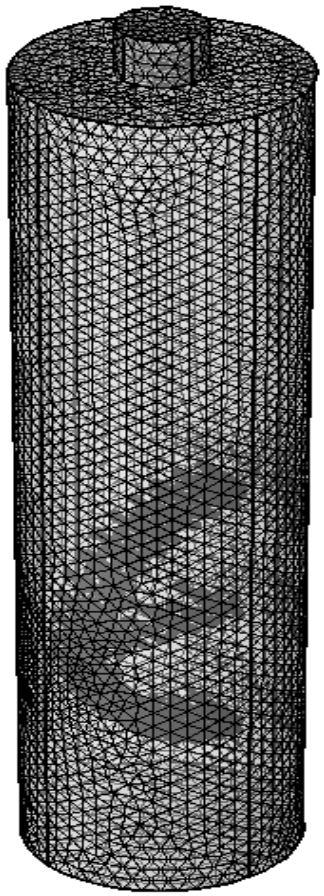

Figure 5.3: Illustration of a domain of GR2 mesh.

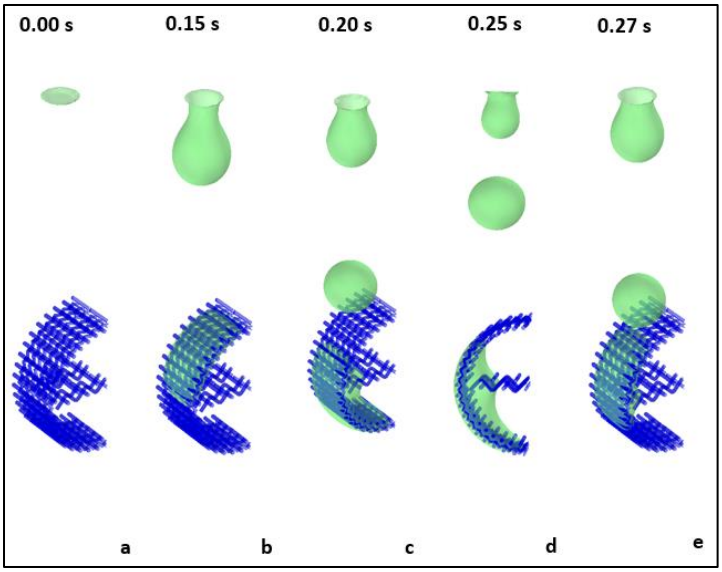

Figure 5.4: Flow pattern of VOF = 0.5 for uncoated Dixon rings using the grid GR2-1, $W_e = 0.23$ and $\theta = 60°$: (a) 0 s, (b) 0.04 s, (c) 0.05 s, (d) 0.06 and (e) 0.27 s.

5.3 Flow around coated Dixon rings

Figure 5.5 (a,b) shows a scanning electron microscope image of a coated Dixon ring. The coating was concentrated in the areas near the pores and an area where wires intersect. EDS tests showed the molar percentage of 8% alumina of coating at the convex area of the wires, as described in the previous work [66]. These surface non-uniform distributions of the coating will have an impact on fluid flow through the opening as discussed in the following section.

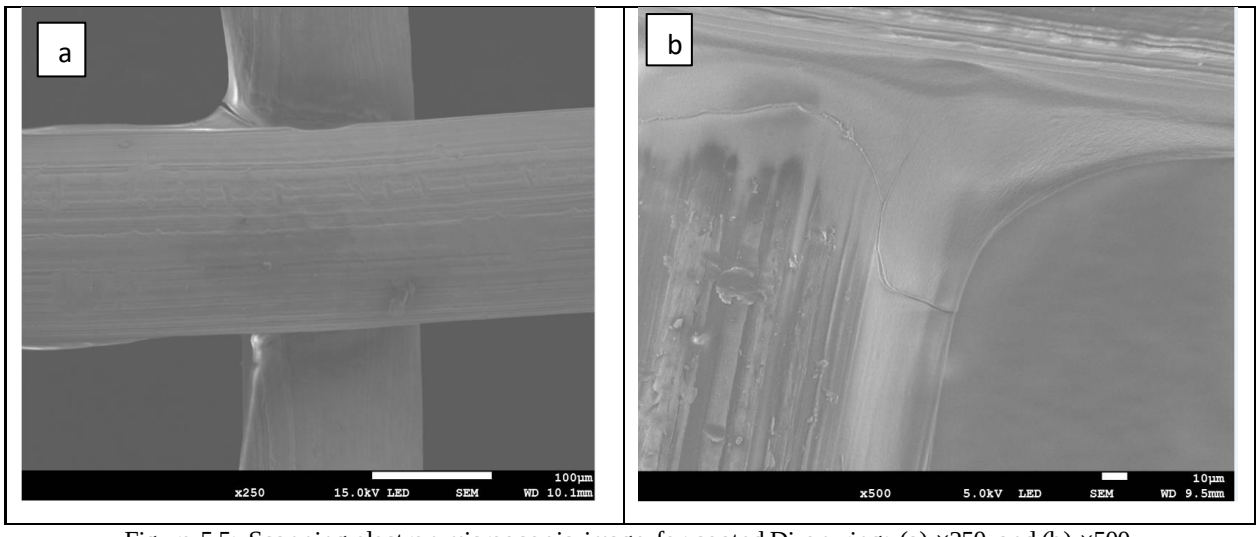

Figure 5.5: Scanning electron microscopic image for coated Dixon ring: (a) ×250 and (b) ×500.

The flow around the coated Dixon rings was assessed by the experimental flow analysis and the VOF simulation. The static contact angle of the coated Dixon ring was challenging to assess experimentally due to the complex geometry of the stainless-steel grid.

To confirm the contact angle θ of the coated Dixon rings, the results of the laboratory observations of three depositions of alumina were compared to those obtained by simulation for different contact angles, ranging from hydrophilic to hydrophobic nature (i.e. 60 to 120°). Among these, the one based on a static contact angle $\theta = 105°$ demonstrated flow patterns similar to the experiments on coated Dixon rings.

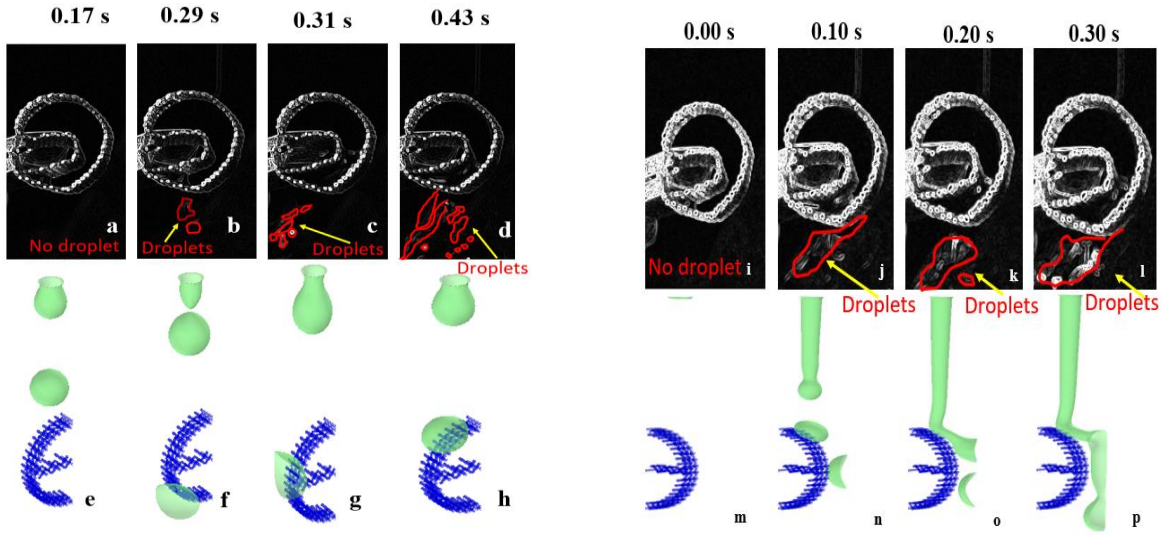

Figure 5.6: Flow pattern by the experimental and simulation observations: Snapshots of impact of droplets on coated stainless steel Dixon rings: $\theta = 105°$, $W_e = 0.23$ (a-h) and $W_e = 0.64$ (i-p)

As shown in Figure 5.6(a-h), at $W_e = 0.23$ and at 0.17 s, both experimental and simulation results show that capillary droplets were about to impinge the Dixon ring. The experimental droplet was repelled by the surface at 0.31 s while the simulation droplet was repealed at 0.29 s. The droplet accumulated at the top surface of the ring where the surface energy was high and the thickness of the liquid reached a maximum value, promoting then gravitational forces and leading the droplet to slip over the vertical curvature and detached at the bottom surface of the ring. Both the model and the experiments showed no penetration of the liquid into the grid of the coated Dixon ring, owing to its hydrophobic nature. Minor differences in the flow pattern occurred due to the non-uniformity of the contact angle, which made the droplet move around the Dixon ring until being

forced to detach by the next droplet at 0.43 s and 0.29, as shown in Figure 5.6 (d) and (f), respectively.

At W_e value of 0.64, the droplet accumulated at the top surface of the ring at a higher rate in comparison with the surface energy, accelerating the gravitational forces and detachment at the bottom surface of the ring. Few discrepancies were observed between the model results and the experiments, as illustrated in Figure 5.6 (i-p). The analysis focused on understanding the relationship between the nature of the packing (i.e. hydrophobic or hydrophilic) and the changes in the flow pattern over time. The images taken by the camera showed similar shapes to the droplets by simulation except for a minor amount of liquid that penetrated the Dixon rings opening, as shown in Figure 5.6 (i). This disagreement could be caused by some assumptions used in the CFD simulation (i.e. the initial wall boundary conditions, constant wetted wall angle instead of a dynamic one with associated hysteresis and phase properties).

Figure 5.6 (o and p) shows an average thickness over the length of the liquid film of 2 mm. Some tails are also observed which indicate the formation of a successive bubble that does not pass the mesh of the packing. Liquid-solid frictions led to extended droplets of lower local velocity compared with relevant bulk velocity. At a W_e value of 0.23, phenomena of shrinkage and spreading over the sides of the Dixon rings were not observed, demonstrating the relevance of inertial forces over the surface tension forces. Overall, the flow over the coated and the uncoated Dixon rings has shown that the coated version offered liquid spreading over the mesh opening in comparison with the uncoated one which offered more film flow that passed through the meshes for improved wetting efficiency.

5.4 Wetting efficiency by a parametric study

5.4.1 Influence of liquid inlet velocity

The wetting efficiency is defined as the ratio of the wetted area over the total area of packing. The effect of velocity u_o on the wetting efficiency was studied for the coated and uncoated rings. The profiles of wetting efficiency were calculated by averaging the liquid volume fraction (V_{f_1}) over the surface of the coated or uncoated rings with respect to time, as summarised in Figure 5.7 and Figure 5.8. The peaks appearing at u_o = 0.15 and 0.25 m/s illustrates the wetting profile of the liquid droplet over the Dixon rings packing. Two distinctive peaks appeared for u_o = 0.15 m/s,

each peak corresponded to dynamic profiles of wetting efficiency of the coated and uncoated rings with time and inlet liquid velocity and more relevant Figures of dynamics of the impact of the droplets with time were added (A 1). The liquid velocity was varied at 0.15, 0.25, 0.35 and 0.5 m/s. The velocity values of 0.15, 0.25 and 0.35 m/s corresponded to a dropwise flow from the nozzle while the velocity of 0.5 m/s corresponded to a jet flow from the nozzle. The residence time was approximately 0.05 s (i.e. first peak initiated at 0.15 s and ended at 0.2 s while the second peak started at 0.25 s and ended at 0.3 s). Conversely, five peaks appeared for the uncoated rings. The wetting efficiency reached a steady-state pattern after approximately 0.3 s. As shown in Figure 5.8, the residence time for a single peak is 0.09 s, which is three times higher than that of the coated rings.

As shown in Figure A1 (c), in appendix A, the droplet hit the Dixon ring at 0.14 s at high wetting efficiency but was then repelled by the hydrophobic nature of the ring at 0.15 s. As shown in Figure A2 (g-l), when u_o was increased to 0.25 m/s, the drag forces destabilised the liquid stream by delaying the outer layers of flow in respect to the inner ones, driving the cohesive molecular forces to become tenuous. The slower outer molecules dragged the inner molecules until the surface tension forces have exceeded the inertial forces [196]. At u_o of 0.35 m/s, the flow pattern changed because the surface tension forces were not dominant. The dynamic profiles of wetting efficiency of the coated rings with time and inlet liquid velocity are summarised in Figure A3 and A4. The profiles of wetting efficiency are similar to those observed in the coated rings, but the residence time of the droplets of the uncoated Dixon rings was longer than that of the coated rings due to stronger adherence of the droplets to the rings, slowing down their travel inside the rings. At high liquid rates in both cases of coated and uncoated rings, the inertial forces dominated over the surface forces, resulting in the steady-state profile. It was not surprising to find that the wetting efficiency increased with u_o, which agreed with the work reported by Du *et al.* [10] confirming that u_o and the time required to reach the steady-state were directly proportional to each other. Overall, the high-velocity values stabilised the liquid shape of both uncoated and coated Dixon rings. The flow around the uncoated Dixon ring was converted into a film flow of uniform thickness due to a significant change in velocity over local parts of the droplets (i.e. increased thickness of the rolling droplet with reduced changes of the local parts).

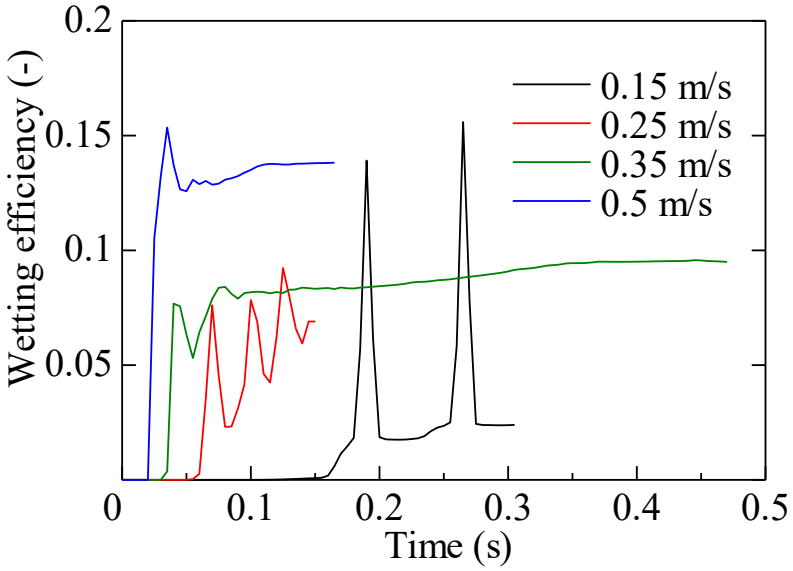

Figure 5.7: The wetting efficiency profile for u_o = 0.15 m/s (black line), 0.25 m/s (red line), 0.35 m/s (green line) and 0.5 m/s (blue line) for coated rings, θ = 105°.

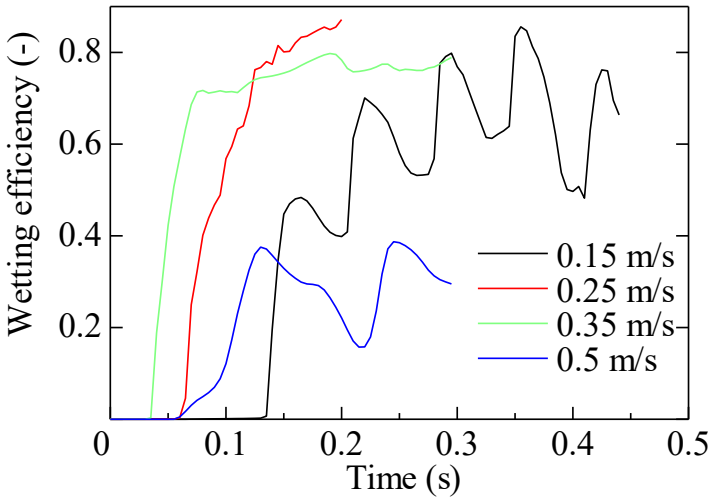

Figure 5.8: The wetting efficiency profile for u_o = 0.15 m/s (black line), 0.25 m/s (green line), 0.35 m/s (red line) and 0.5 m/s (blue line) for uncoated rings, θ = 60°.

5.4.2 Influence of contact angle

The influence of contact angle on the wetting of Dixon rings was investigated for a reference velocity u_o of 0.15 m/s. The droplet dynamics for the actual coated ring ($\theta = 105°$) and uncoated rings ($\theta = 60°$) were evaluated. Two additional values of the contact angle at 90° and 120° were also simulated, allowing observation of the behaviour of flow through the opening and flow over the surface of Dixon rings, prediction of the flow over more hydrophobic and hydrophilic conditions, that is a higher angle than 120° and lower than 60°, respectively, reproducing phenomena of solvent-surface interactions of a wide range of industrial applications [197].

At the value of $\theta = 60°$, which corresponds to the uncoated Dixon ring, the droplet adhered to the ring, spread over to achieve maximum wetting and passed through the mesh opening, as illustrated in Figure 5.9 (a). At $\theta = 90°$, the droplet passed through the mesh opening of the Dixon rings but with less wetting, as shown in Figure 5.9 (b) and then was repelled at long residence times in the Dixon ring. These trends continued at higher contact angles (i.e. $\theta = 105°$ and 120°) where the droplet observed no bouncing on the Dixon ring wall but a weaker adherence to the rings and more rolling over the wall of the rings, resulting in the lowest wetting efficiency, as shown in the wetting profile in Figure 5.10.

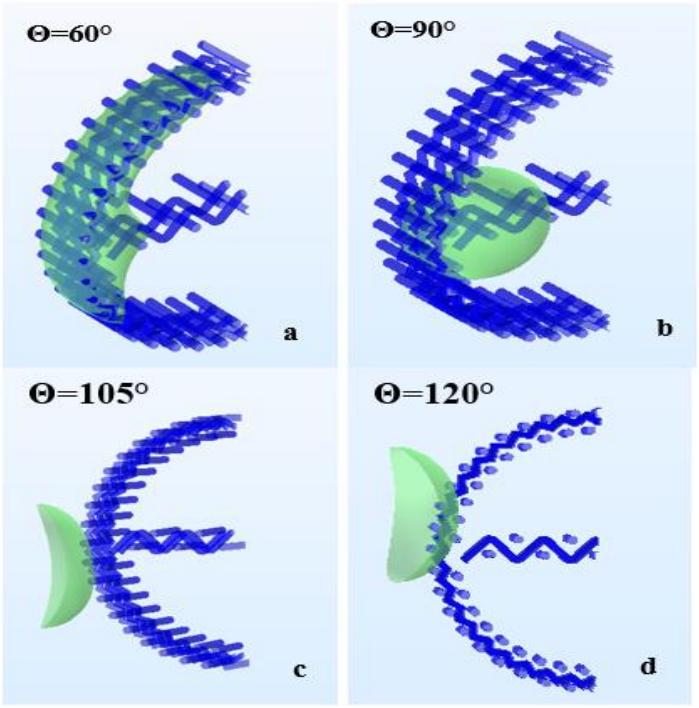

Figure 5.9: Flow pattern of VOF = 0.5 at 0.14 s using the grid GR2, We = 0.23 for θ: (a) 60° (uncoated Dixon rings); (b) 90°; (c) 105° (coated Dixon rings); (d) 120°.

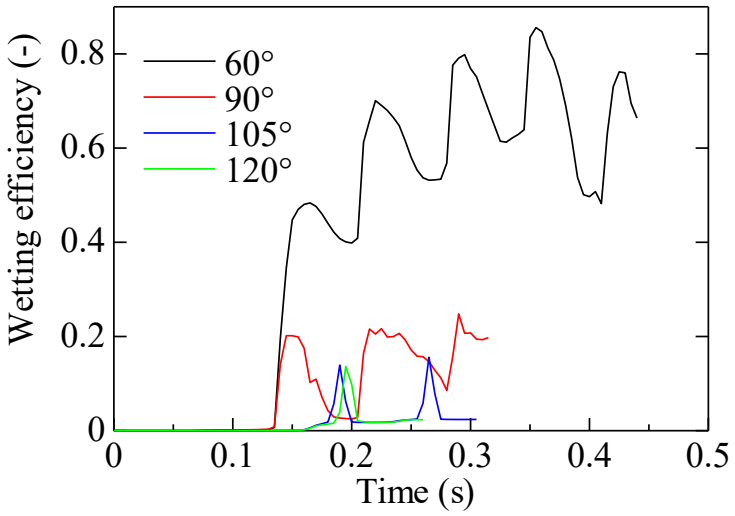

Figure 5.10: The wetting efficiency of Dixon rings for We = 0.23.

5.5 Hydrodynamic performance

5.5.1 Liquid holdup

The liquid holdup was obtained by averaging the volume of the liquid volume fraction (V_{f_1}) on Comsol. The liquid holdup (h_l) was studied for Weber number (W_e) 0.23 to 2.57 for θ = 60°, 90°, 105° and 120°, as shown in Figure 5.11 and Figure 5.12. The trend for h_l was similar to the wetting efficiency profiles, when the wetting efficiency increased, the liquid holdup increased and therefore h_l increased with W_e and reduced contact angles. The liquid holdup for the uncoated Dixon rings (i.e θ = 60°) is the highest among all, as shown in Figure 5.11. A minor discrepancy was found at W_e = 2.66, θ = 90° had the highest liquid holdup. This is a consequence of numerical modelling and could be explained by the fact that more liquid was allowed, which is particularly true in the range of contact angle from 90° to penetrate the mesh opening, while some adherence of the liquid is observed for the uncoated Dixon rings at θ = 105°.

The results from the VOF model were compared to models usually used in literature for random packing structure (i.e. Stichlmair *et al.* [198] by equations (5.1) and (5.2) and Billet and Schultes [26] by equation (5.3), as illustrated in Figure 5.12 (a-d). The model results for h_L were fitted to Stichlmair *et al.* [198] using 2-D curve-fitting on Matlab. An exclusive correlation for the liquid holdup for Dixon ring, is shown in equation (5.1). The model constant had 95% confidence bounds, b = 0.226, c = 0.08083 and R-square= 0.9557. The results for θ = 60°, 90°, 105° and 120° are in a reasonable agreement with those by Stichlmair's model, particularly in the hydrophilic zone of the contact angle 60° and 90°, as shown in Figure 5.12 (a) and (b), respectively. The comparison for hydrophilic Dixon rings showed that Stichlmair *et al.* [198] model is reliable at low W_e (i.e. the relative deviation of 7.21 % at θ = 60° and 14.12 % for θ = 90°). The reliability of the CFD model decreased at high W_e (i.e. relative difference was low for all W_e except at W_e = 2.66 where it reached deviation of 42.31 %). At θ = 105° and 120°, as shown in (c) and (d), both Stichlmair *et al.* [198] and Billet models showed poor predictions, the relative difference errors being 24.01% and 33.23%, confirming additional local mixing could take place. Discrepancies between the CFD model and the literature for h_L has been observed for the Dixon rings. The discrepancies were large at low We which corresponds to low liquid velocity. These disagreements occur due to the maldistribution of the fluid flow which is not accounted to in the empirical models in. More

disagreements were found for at low velocity where droplet regime occurs compared to the jet flow of water.

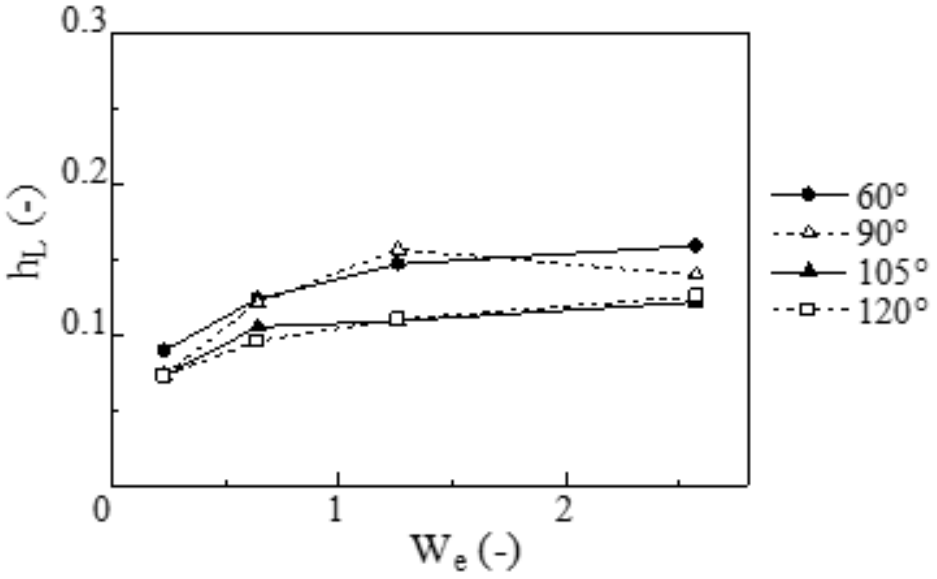

Figure 5.11: Effect of Weber number (W_e) on the liquid holdup (h_l) for uncoated Dixon rings, θ = 60° (filled circles), 90° (hollow triangles), 105° (filled triangles) and 120° (hollow squares).

$$h_L = 0.080\, {F_{r_L}}^{0.22} \tag{5.1}$$

$$F_{r_L} = \frac{{u_0}^2 a_p}{g} \tag{5.2}$$

$$h_L = 12\left(\frac{\vartheta}{g\rho_L} u_0 {a_p}^2\right)^{1/3}\left(\frac{a_e}{a_p}\right) \tag{5.3}$$

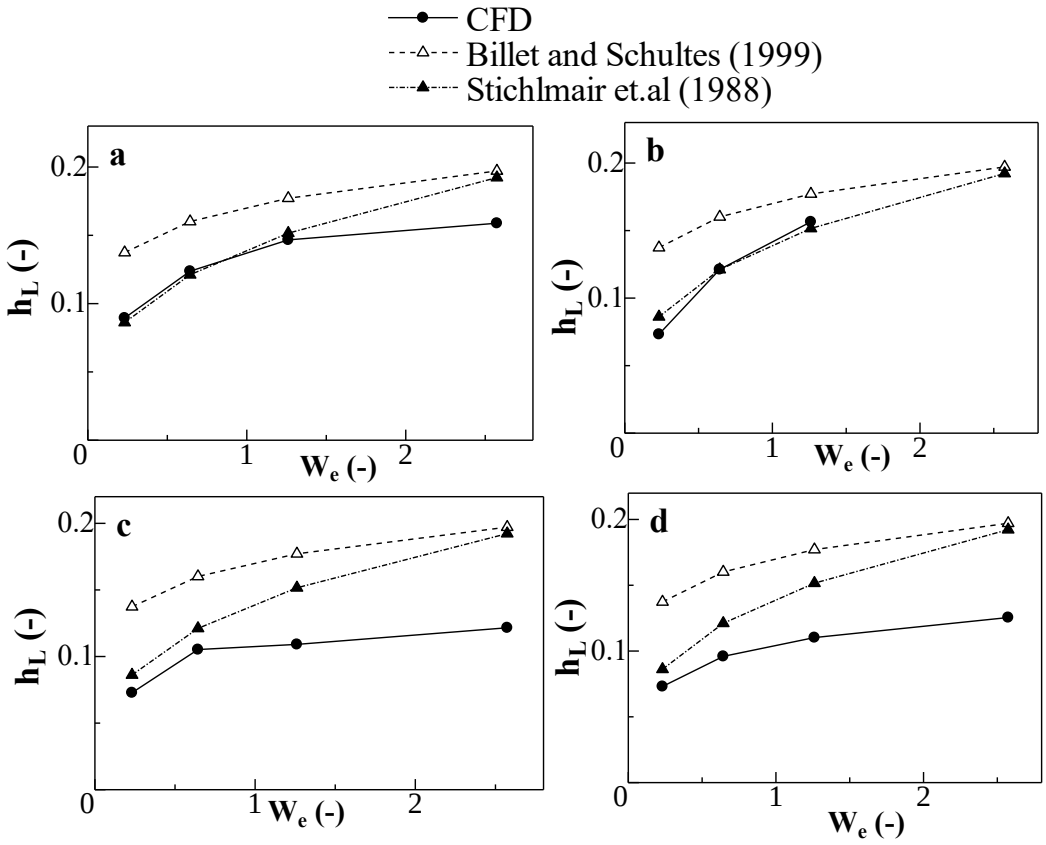

Figure 5.12: Effect of Weber number (W_e) on the liquid holdup (h_l): a) θ = 60°; b) θ = 90°; c) θ = 105°; d) θ = 120°.

5.5.2 Effective surface area

The effective area, which is a critical parameter in gas-liquid mass transfer operations, was calculated by averaging the liquid volume fraction (V_{f_1}) and dividing by the surface of the Dixon ring. The effective area (a_e) was studied for a range of Weber number between $W_e = 0.23$ and 2.57 and contact angle of θ = 60°, 90°, 105° and 120°, as illustrated in Figure 5.13. The general trend shows the effective area increased with W_e. The highest effective area is at θ = 60°, while the lowest is at $\theta =$ 120°, except for $W_e = 0.23$, the effective area at 105° is lower than that of 120° with a value of 0.031.

These results were compared to Linek *et al.* [199] given by equation (5.4) and Billet and Schultes [26] given by equation (5.5), for θ = 60°, θ = 90°, θ = 105° and θ = 120°, as shown in Figure 5.14

(a-d). Billet and Schultes [26] requires additional physical parameters such as density (ρ_L) and viscosity (u_L). The results obtained using the CFD modelling were closer to the model by Linek (i.e. relative difference error for Linek *et al.* [199]model are 15.40% at θ = 60° and 14.24% for θ = 90°). Billet and Schultes [26] were higher than 40% for most of the contact angles but at θ = 105° and 120°, the relative deviations were 31.05 % and 15.32%. This shows that Linek *et al.* [35] was more reliable to predict the effective area for Dixon rings.

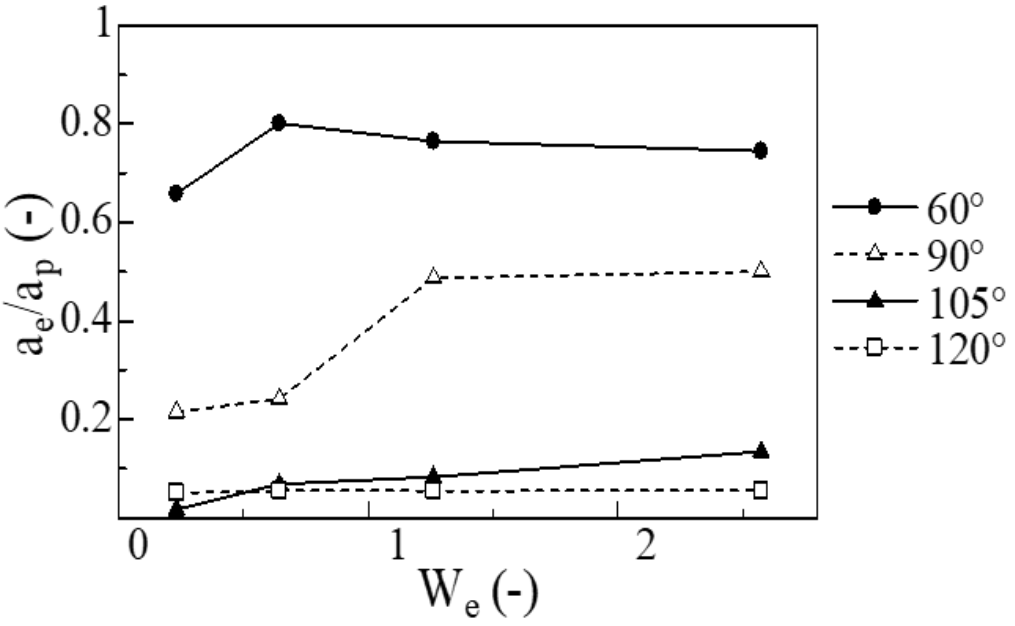

Figure 5.13: Effect of Weber number (W_e) on the normalized effective area for uncoated Dixon rings.

$$\frac{a_e}{a_p} = 0.0277 \left(\frac{1+cos\theta}{2}\right)^{3.477} (a_p d_p)^{1.585} \left(\frac{\rho_L u_0}{a_p \mu_L}\right)^{0.641-0.407\left(\frac{1+cos\theta}{2}\right)} \quad (5.4)$$

$$\frac{a_e}{a_p} = 1.5(a_p d_p)^{-0.5} \left(\frac{u_0 d_p}{\mu_L}\right)^{-0.2} \left(\frac{\rho_L d_p {u_L}^2}{\sigma_L}\right)^{0.75} \left(\frac{{u_L}^2}{g d_p}\right)^{-0.45} \quad (5.5)$$

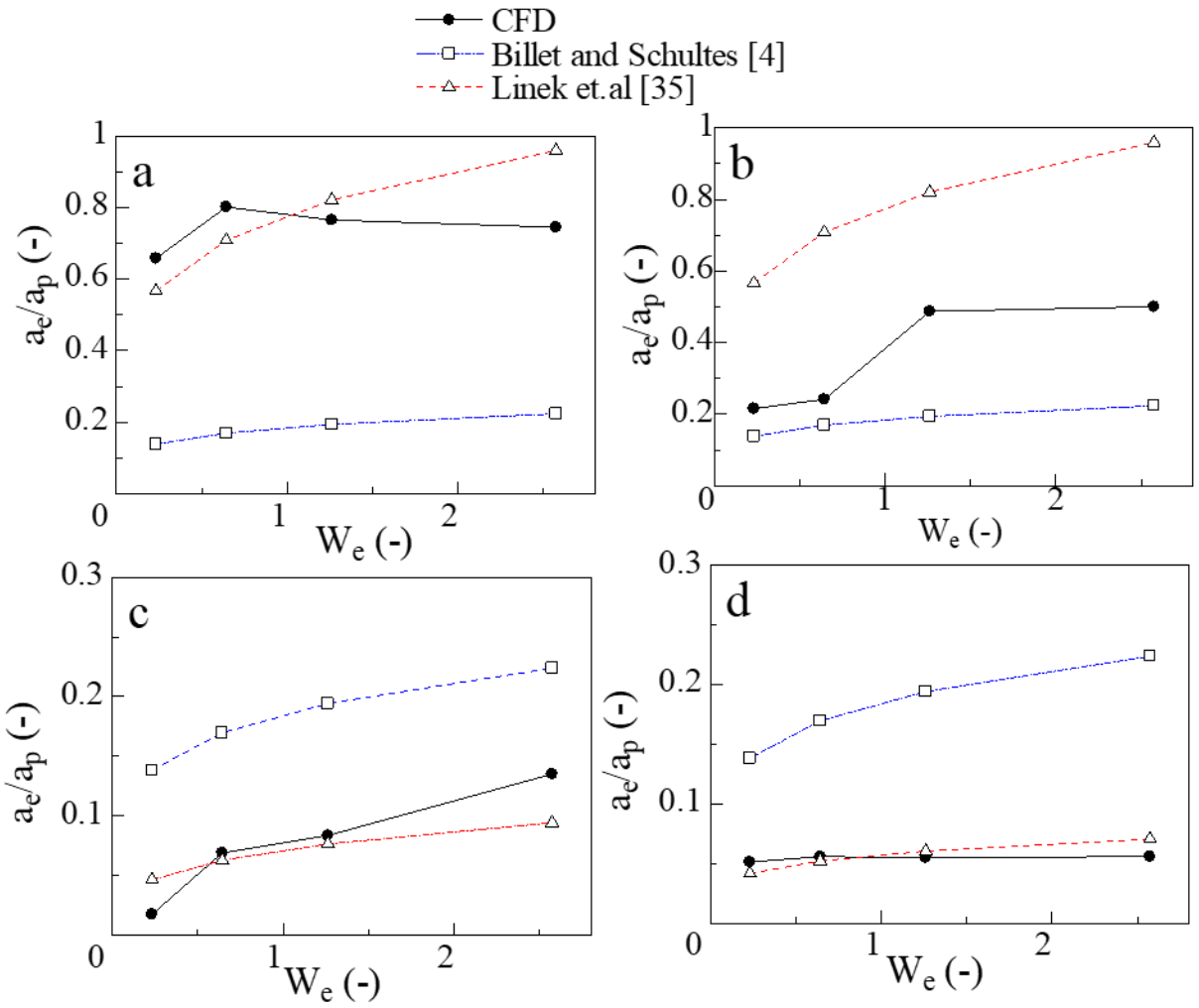

Figure 5.14: Effect of Weber number (W_e) on the normalised effective area for: a) θ = 60° b) θ = 90° c) θ = 105° d) θ = 120°.

In conclusion, using CFD, the pore-scale behavior of liquid was investigated for uncoated and coated Dixon rings. This investigation was conducted using VOF model using COMSOL Multiphysics 5.3a which was validated using CCD images. The effects of the liquid inlet velocity and the contact angle on the liquid flow pattern and the wetting efficiency were investigated using a parametric study. The coating resulted in hydrophobic surface properties which decreased the wetting efficiency from 0.8 to 0.15 at u_o= 0.15 m/s. Finally, the value of the liquid holdup for uncoated and coated Dixon rings was of 0.09 and 0.15, respectively.

6 Chapter 6: Macroscale experiments for hydrodynamics and mass transfer characteristics of Dixon rings

The hydrodynamics characteristics of the coated and uncoated Dixon rings were studied on a microscopic level, as described in Chapter 5. Understanding the hydrodynamics on larger scale is highly required to determine hydrodynamic parameters such as pressure drops, liquid holdup and mass transfer efficiency. Unfortunately, these parameters have been missing in the literature for Dixon rings packing. In this section, experiments were therefore conducted to evaluate the pressure drop, liquid hold up and mass transfer for Dixon rings $^{5}/_{8}$ and $^{1}/_{4}$ in.

A large column was used for this investigation, including a height and diameter of 0.08 m and 1.2 m, respectively. Since the sol-gel procedure for coating the Dixon rings was limited to 16 rings per batch, the scaleup was avoided for the coated Dixon rings for hydrodynamic and mass transfer studies. These studies were exclusively carried out for the non-coated rings because thousands of coated Dixon rings would have been needed to conduct a study.

6.1 Pressure drop

The pressure drop was evaluated for a range of gas and liquid flowrates for two Dixon rings sizes: $^{5}/_{8}$ in and $^{1}/_{4}$ in, as shown in Figure 6.1. The pressure drop increased with gas packing factor F_s which presents the gas velocity until reaching the flooding region. The general trend in Figure 6.1 showed that the pressure drop value also increased with increasing the liquid load. It can be observed that the lines are approximately parallel, and the gradient is approximately equal. Additionally, it is observed that as the liquid flow rate increases, the flooding point occurs sooner; i.e., the pressure drop is lower, and the gas flow rate is also lower.

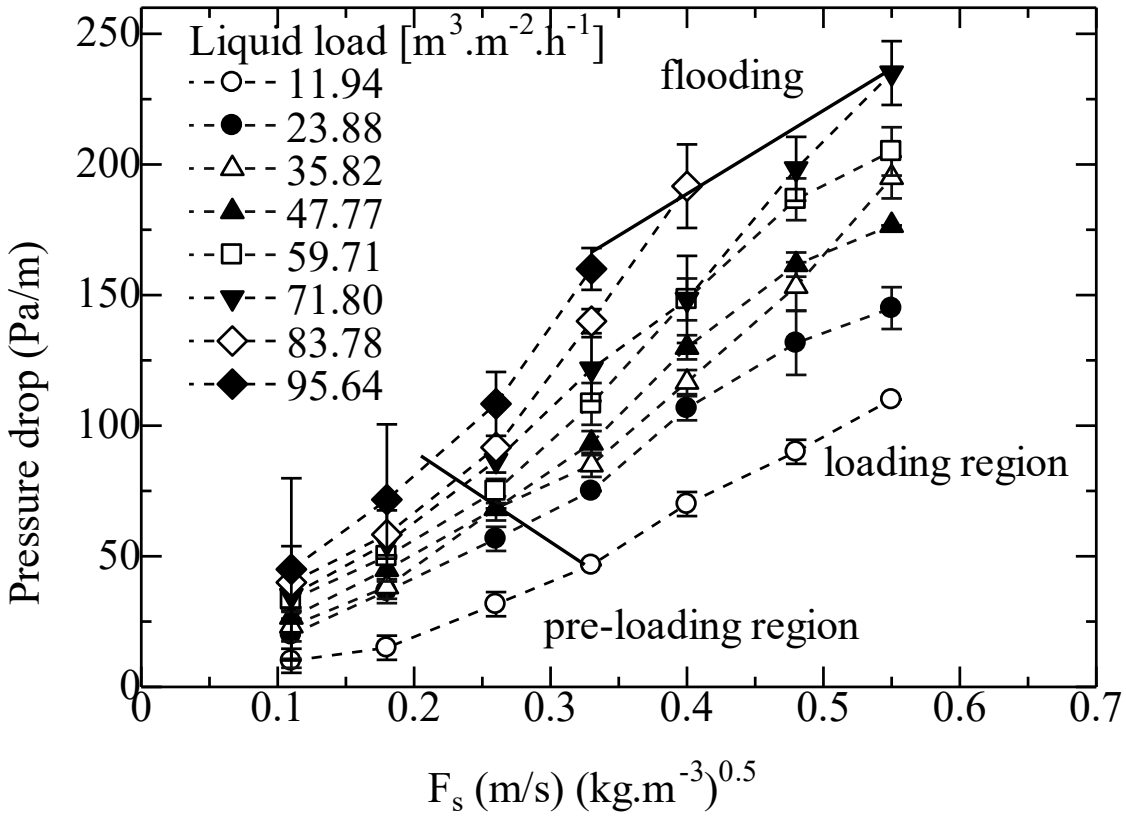

Figure 6.1: The variation of the pressure drop with the gas packing factor F_s for Dixon rings $^5/_8$ in.

The tested range of liquid load was from 11.94 to 95.64 ($m^3.m^{-2}\ h^{-1}$) for Dixon rings $^5/_8$ in as shown in Figure 6.1. It was also found that flooding reached a liquid load of 71.8 ($m^3.m^{-2}\ h^{-1}$). Conversely, the flooding boundary was reached for Dixon rings $^1/_4$ in starting from the lowest liquid loads at 11.94 at F_s 0.35 (m/s) $(kg/m^{-3})^{0.5}$ at pressure drop value of 250 Pa/m. Dixon rings $^5/_8$ in have a larger volume than Dixon rings $^1/_4$ in thus offering more free space for the gas and liquid to flow. This resulted in a lower pressure drop compared to Dixon rings $^5/_8$ in as the friction forces between gas and liquid are lower.

The pressure drop profile for Dixon rings ¼ in has three significant regions: pre-loading, loading, and flooding. At a particular liquid flowrate, each region is expressed by the change in pressure drop concerning the change in gas flowrate. As the column's liquid or gas flow rate increases, the

free area decreases, and the frictional force between the counter flow increases. Hence, liquid holdup occurs and eventually leads to flooding. The average of the data obtained for each liquid flowrate for the range of gas flowrates up to the flooding point are illustrated in Figure 6.2. Illustrative lines were added to differentiate between the loading and the pre-loading regions. The pre-loading region appears to originate from a single point, much like wet and dry packing. The pressure drop then linearly increases up until the loading point. In this region, an increase in liquid flow rate increases in gradient. With increasing liquid flow rate, the loading point linearly increases with pressure drop and linearly decreases with gas flow rate. This is a typical trend as the liquid in the column occupies more space, causing a more significant frictional force and, therefore, a larger pressure drop while at lower gas flow rates. Once the gas flow rate exceeds the loading point for the liquid flow rate, the pressure drop increases at a larger rate than the pre-loading region, as expected.

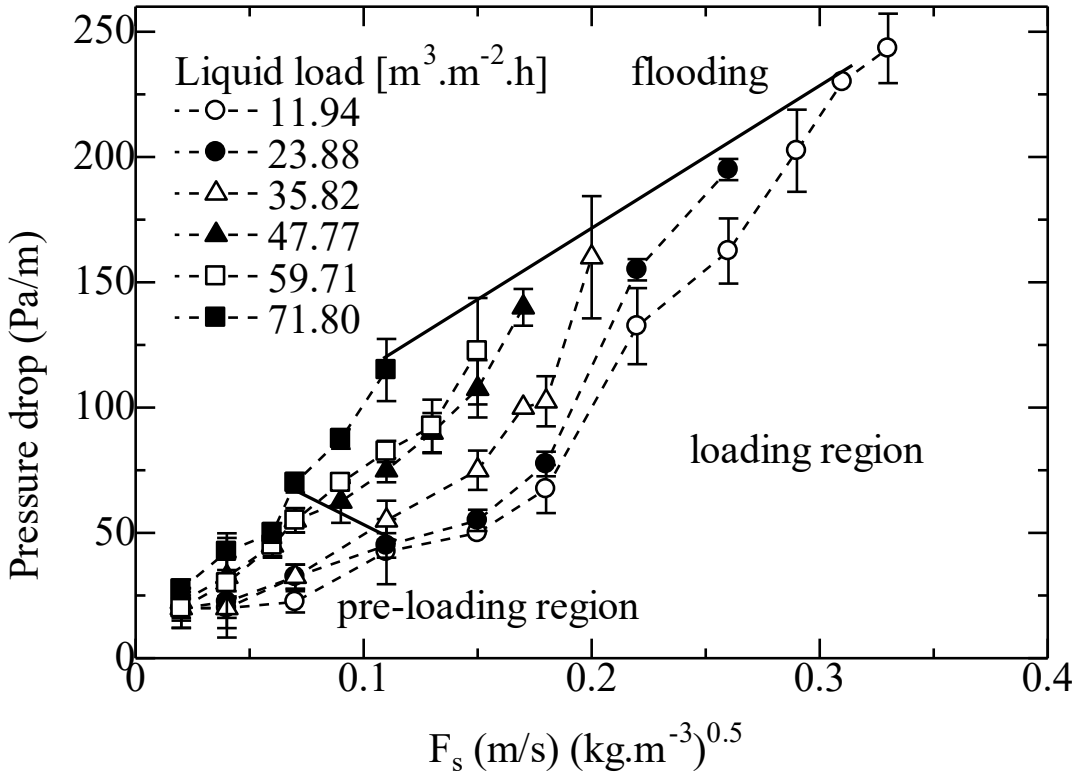

Figure 6.2: The variation of the pressure drop with the gas packing factor F_s for Dixon rings $^1/_4$ in.

The pressure drop trends for Dixon rings $^5/_8$ and $^1/_4$ in were revealed as shown in Figure 6.3. The pressure drop for Dixon rings $^5/_8$ in is much lower than Dixon rings $^1/_4$ in. As shown in Figure 6.2, a trend of a striaght line is shown for Dixon rings $^5/_8$ in. This is due to the pressure drop trend showed the column was operating at the pre-loading region. The pre-loading region accompanies low-pressure drop but is not the preferred region for operation due to the low mixing. It should be noted that the column's operational conditions were limited by the measurable ranges of the flowrate measurement devices (i.e., mass flow meters (MFC) and rotameters).

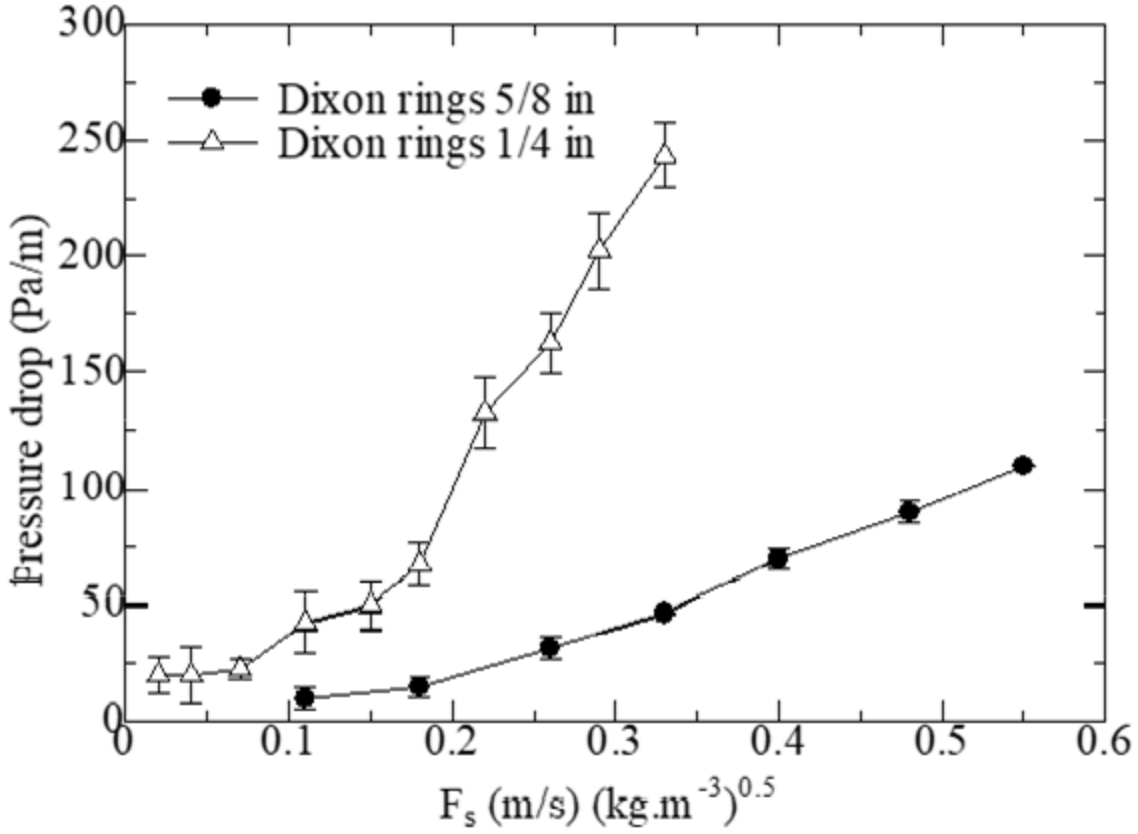

Figure 6.3: The variation of the pressure drop with the gas packing factor F_s for liquid load 11.94 ($m^3.m^{-2}$ h^{-1}).

Otherwise, the gas and liquid operational conditions should have been increased for Dixon rings $^5/_8$ in. On the other hand, the pressure drop profile for Dixon rings $^1/_4$ in illustrated that the operation had reached the pre-loading, loading, and flooding regions. The pre-loading region started at F_s 0.5 to 1.3 (m/s) $(kg/m^3)^{0.5}$. The column entered the loading region at F_s value of 1.3 to 3.5 (m/s) $(kg/m^3)^{0.5}$. Finally, flooding occurred at F_s value of 3.5 to 5 (m/s) $(kg/m^3)^{0.5}$, therefore, the operational conditions could not be increased further.

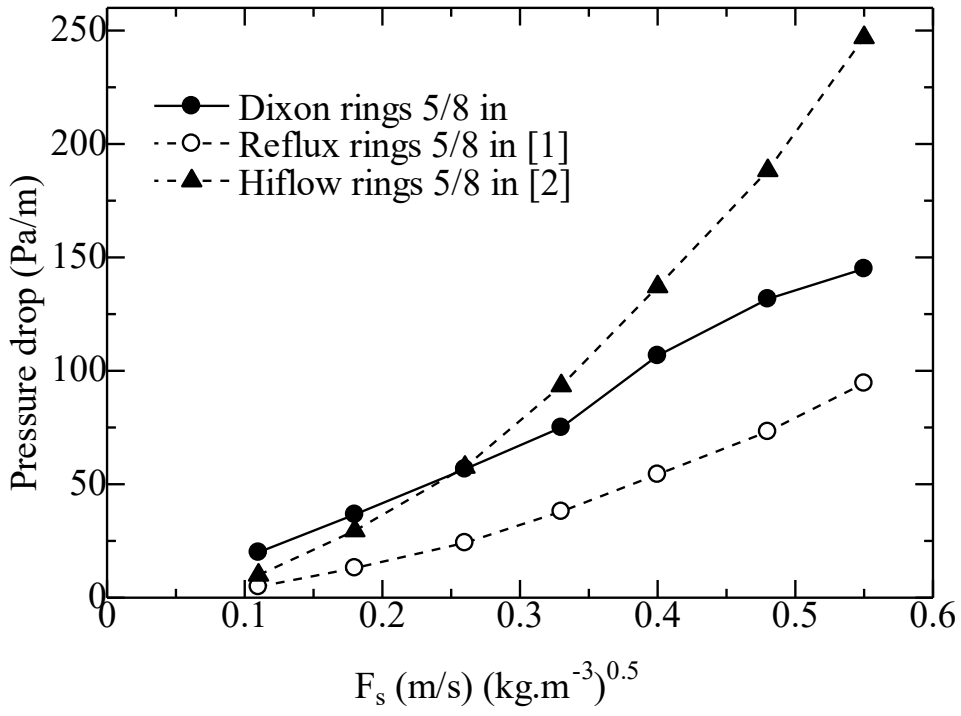

Figure 6.4: The variation of the pressure drop with the gas packing factor F_s for liquid load 23.88 ($m^3.m^{-2}$ h^{-1}). Solid lines represent experimental data while dashed lines are used for literature data.

The data for pressure drops were compared to other random packings of similar size and material. Data from Stichlmair et al. [200] and Maćkowiak [28] were used for comparison, as shown in Figure 6.4 and Figure 6.5. Hiflow rings $^5/_8$, which hold crosectional extensions that could obstruct the flow, were found to have higher pressure drop than Dixon rings $^5/_8$ in. Reflux rings $^5/_8$ in were found to have lower pressure drop than Dixon rings $^5/_8$ in. As shown in Figure 6.5, Raschig rings $^1/_4$ in, which holds plain lateral walls, have a higher pressure drop than Dixon rings $^1/_4$ in which holds lateral opening, but Pall rings $^1/_4$ in have a lower pressure drop due to its large lateral opening.

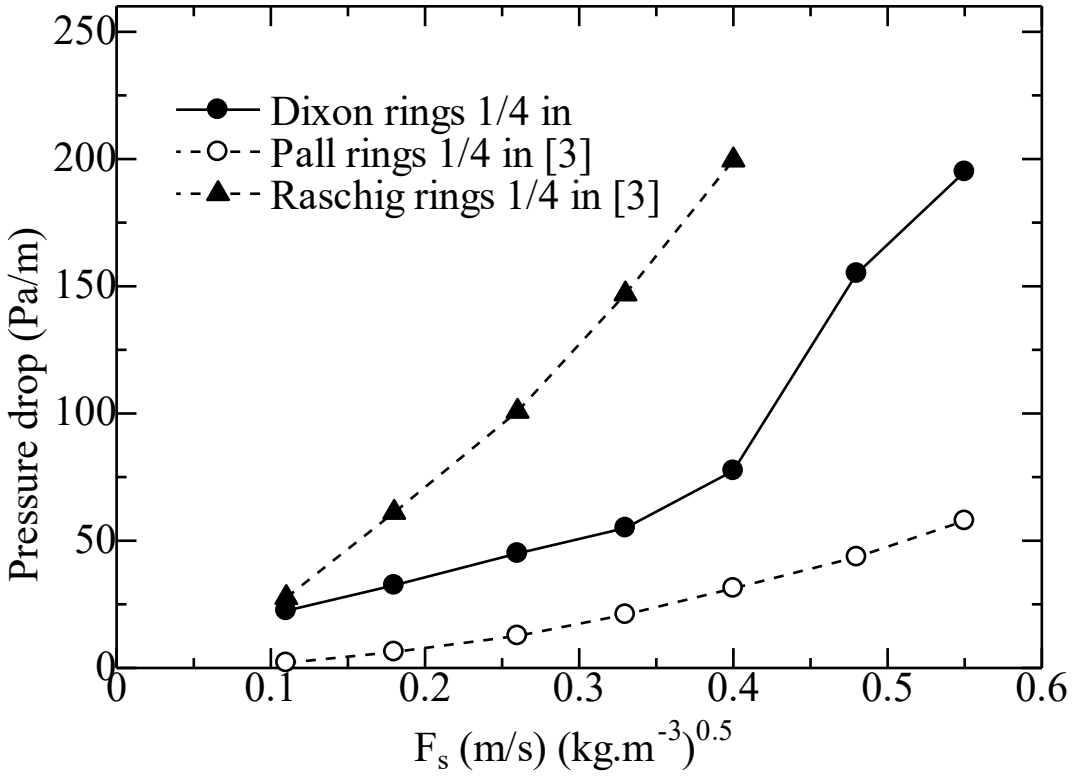

Figure 6.5: The variation of the pressure drop with the packing factor F_s for liquid load 22.88 ($m^3.m^{-2}$ h^{-1}). Solid lines represent experimental data while dashed lines are used for literature data

6.2 Liquid holdup

The liquid holdup was evaluated at various liquid flowrates which is presented as a function of liquid capacity factor L_s for several packing, as shown in Figure 6.6.

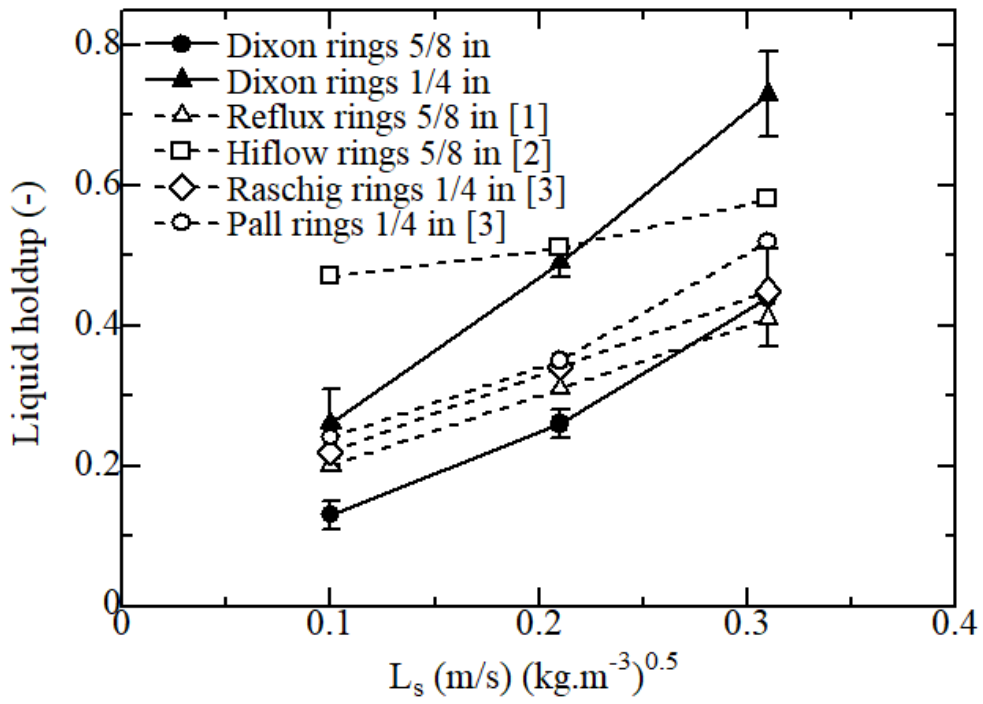

Figure 6.6: The variation of the liquid holdup with the liquid capacity factor L_s (m/s) $(kg/m^3)^{0.5}$ for F_s 0.02 (m/s) $(kg/m^3)^{0.5}$. Solid lines represent experimental data while dashed lines are used for literature data

The values of the liquid holdup for Dixon rings $^1/_4$ in were found to be higher than those of Dixon rings $^5/_8$ in. As shown with the circles data points in Figure 6.6, the liquid holdup for Dixon rings $^5/_8$ in increased from 0.135 to 0.4 from L_s 0.1 to 0.3 (m/s) $(kg/m^3)^{0.5}$. The liquid capacity factor L_s had a greater influence on the liquid holdup for Dixon rings $^1/_4$ in. The liquid holdup value increased from 0.21 to 0.7 from L_s 0.1 to 0.3 (m/s) $(kg/m^3)^{0.5}$. As L_s increase in the column, the free area decreases, and the frictional force between the counter flows increases. Hence, liquid holdup occurs and eventually leads to flooding. In addition, the differences in liquid holdup trends for Dixon rings $^5/_8$ in and Dixon rings $^1/_4$ in can be explained by the loading region. For Dixon rings $^5/_8$ in, the tested operational conditions did not achieve the loading region and the entire operation was conducted in the pre-loading region. For counter-current operations, the pre-loading region is only affected by the liquid film thickness and properties [200]. The liquid flowrate does

not have a significant influence on the liquid holdup. Conversely, the liquid holdup was found to increase for Dixon rings significantly $^1/_4$ in because the operation was conducted at the pre-loading and the loading regions. It is noted in Figure 6.6 that F_s 0.18 (m/s) $(kg/m^3)^{0.5}$, a sharp increase in the liquid holdup is observed due to the loading point occurrence. As shown in Figure 6.6, data from Stichlmair et al. [200], Maćkowiak [28], and Wagner et al. [183] were used for comparison. Dixon rings $^1/_4$ in was found to have a higher liquid holdup Dixon rings $^5/_8$ in. Pall rings exhibit a high liquid holdup of 0.5. Conversely, Reflux rings $^5/_8$ in have a lower liquid holdup of 0.25. It can be deducted that packings with smaller sizes have higher liquid holdup due to their large surface area offering higher wetting efficiency, resulting in higher liquid holdups.

6.3 Mass transfer

The mass transfer coefficient (K_{Ga}) was evaluated for several liquid loads for Dixon rings of the size $^5/_8$ in and $^1/_4$ in, as shown in Figure 6.7 and Figure 6.8. For Dixon rings $^1/_4$ in, K_{Ga} was found to be higher than those of Dixon rings $^5/_8$ in and the general trend showed that K_{Ga} increases with the increase in the gas and liquid velocities.

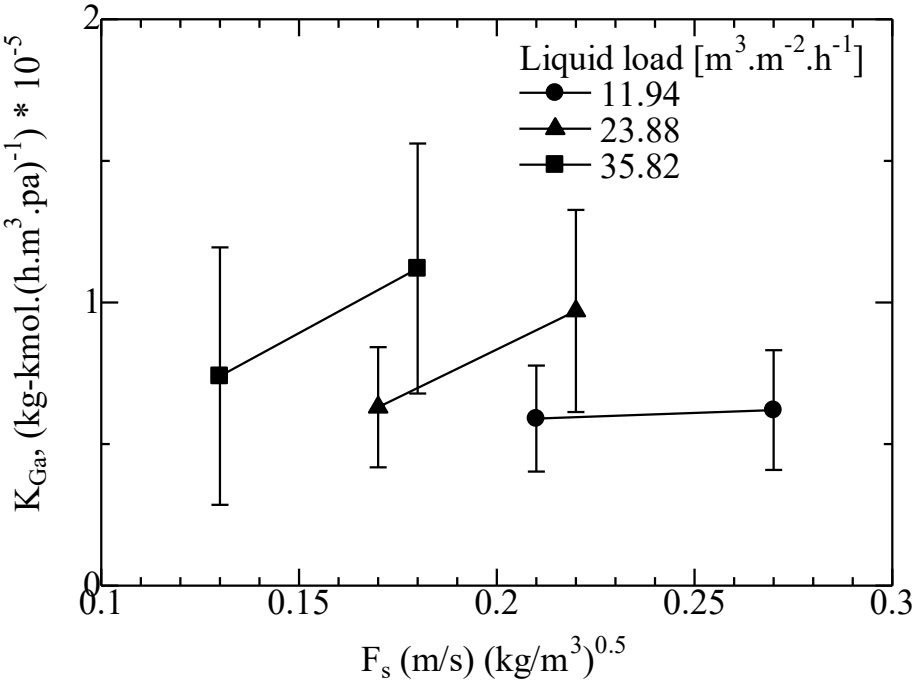

Figure 6.7: The variation of the mass transfer coefficient (K_{Ga}) with the packing factor F_s for different liquid loads: ($m^3.m^{-2}\ h^{-1}$) for Dixon rings $^5/_8$ in.

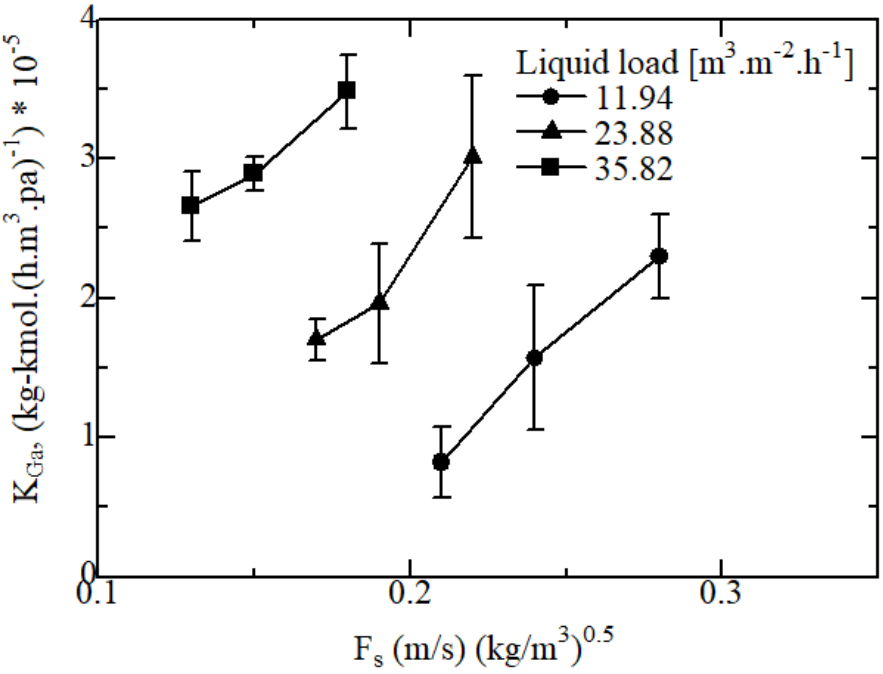

Figure 6.8: The variation of the mass transfer coefficient (K_{Ga}) with the packing factor F_s for different liquid loads: ($m^3.m^{-2}$ h^{-1}) for Dixon rings $^1/_4$ in.

The gas velocity had a low effect on K_{Ga} at low gas velocity for Dixon rings $^5/_8$ as shown in the circles with the solid line in Figure 6.7. For the liquid load 23.88 and 35.82 ($m^3.m^{-2}$ hr^{-1}), liquid flowrate K_{Ga} increased from 0.62 to 1.11 and 0.72 to 1.6 kg.mol/(kg-kmol/(hr.m^3.atm)), respectively. Conversely, Dixon rings $^1/_4$ in K_{Ga} increased at a constant rate by increasing the liquid flow rate. The general trends also showed that the liquid loading has a greater influence than F_s on K_{Ga}.

The HETP for Dixon rings $^5/_8$ in and Dixon rings $^1/_4$ in were compared to other random types of packings, as illustrated in Figure 6.9. Data from Wagner et al. [183] and Kaba et al. [163] were used to compare the HETP values.

The HETP for Dixon rings $^5/_8$ in were higher than Dixon rings $^1/_4$ in. The HETP for Dixon rings $^5/_8$ in were around 0.45 and 0.05 for Dixon rings $^1/_4$ in which indicates that Dixon rings $^1/_4$ in are more efficient in separation applications. Pall rings $^5/_8$ in were found to have the highest

HETP at a value of 0.9 m. On the other hand, Fleximax $^1/_4$ in was found to be the second-best choice after Dixon rings $^1/_4$ in with an average HETP of 0.45.

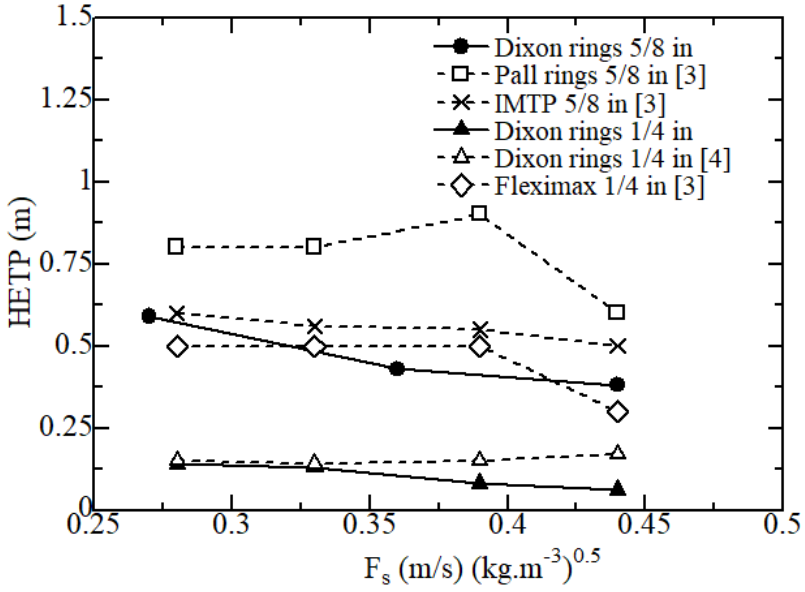

Figure 6.9: The variation of HETP with the gas packing factor F_s for liquid loads 22.88 ($m^3.m^{-2}$ h^{-1}). Solid lines represent experimental data while dashed lines are used for literature data

6.4 Data Modelling

The confidence interval (CI) is used to determine the error for an unknown parameter. A confidence interval is computed at a designated confidence level, 95% confidence level is most common, the confidence level represents the long-run proportion of corresponding CIs that contain the true value of the parameter. Factors affecting the width of the CI include the sample size, the variability in the sample, and the confidence level. [192] The experimental data were used to develop models to predict the dry pressure drop and loading regions on Dixon rings of relevance to the industrial partner of this project (Croft Filters Ltd, Warrington, UK). The values of the gradient and intercept of the dry pressure drop and the loading point were estimated and linear equations are used to describe the dry pressure drop and loading region for Dixon rings. The sum of squared estimate of errors (SSEE) were calculated according to:

$$SSEE = \sum (y_i - \bar{y}_i)^2 \qquad (6.1)$$

where y_i is the measured dependant variable and $\bar{y_i}$ does the model explain the predicted dependant variable. The dry pressure drop and loading point were regressed and involved using the Solver function of Microsoft Excel to minimise SSEE by changing the variables of the models).

$$CCI_{Grad,95,th} = t_{crit} \times SE_{Grad} \quad (6.2)$$

$$CCI_{Inter,95,th} = t_{crit} \times SE_{Inter} \quad (6.3)$$

$$SE_{Grad} = \sqrt{\frac{\sum(y_i - \bar{y_i})^2}{DOF}} \sum (x_i - \bar{x_i})^2 \quad ^{-0.5} \quad (6.4)$$

$$SE_{Inter} = \sqrt{\frac{\sum(y_i - \bar{y_i})^2}{DOF}} \frac{\sum {x_i}^2}{n \sum (x_i - \bar{x_i})^2} \quad (6.5)$$

The 95th confidence intervals values ($CCI_{95,th}$) is a number greater than 95% of the numbers in a given set and is a function of the standard error (SE) and critical value (t_{crit}). For all models, $CCI_{95,th}$ was evaluated for the gradient and the intercept, as shown in equations (6.2) and (6.3), respectively. SE was evaluated for the gradient and the intercept as shown in equations (6.4) and (6.5). SE is a function of dependant (y_i), (x_i) independent variables and the degree of freedom (DOF). The smaller the value of SE, the more accurately the model predicts the experimental data.

6.4.1 Dry pressure-drop

As shown in Figure 6.10 and Figure 6.11, the dry pressure drop for Dixon rings in Dixon rings the general trend indicates a uniform pressure drop increase with the gas capacity factor, and the dry pressure drop was a simple linear correlation. The solid line is the best fit, and the dashed line is generated using the following equations (6.6) and (6.7):

$$y_{95,th} = y_0 \times \left(CCI_{Grad,95,th} + SE_{Grad}\right) + \left(CCI_{Inter,95,th} + SE_{Inter}\right) \quad (6.6)$$

$$x_{95,th} = x_0 \times \left(CCI_{Grad,95,th} + SE_{Grad}\right) + \left(CCI_{Inter,95,th} + SE_{Inter}\right) \quad (6.7)$$

Where $y_{95,th}$ and $x_{95,th}$ are the 95th interval points while y_0 and x_0 are the initial values of the experimental data set.

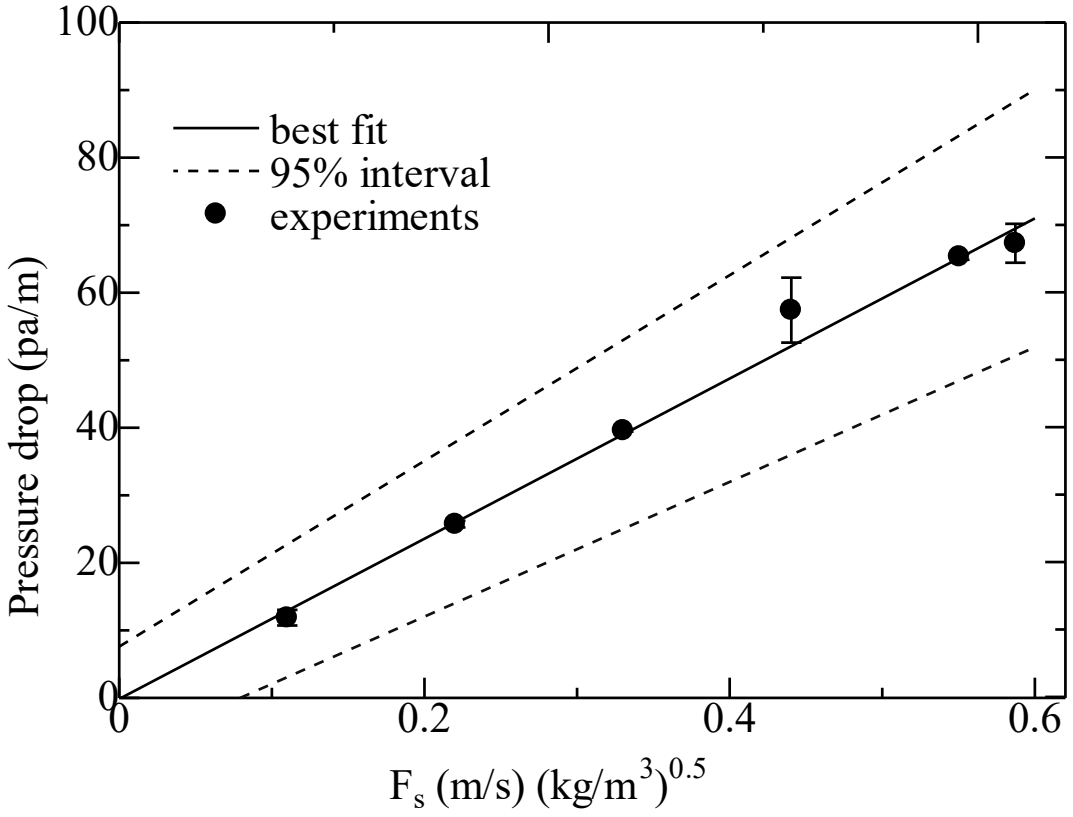

Figure 6.10: Dry pressure drop versus the gas capacity factor for Dixon rings $^5/_8$ in The circles represent the experimental data, the solid line is the linear regression of the data and the dashed lines represent the 95th-centile confidence interval in the data. Each data point shows the corresponding error due to each measurement.

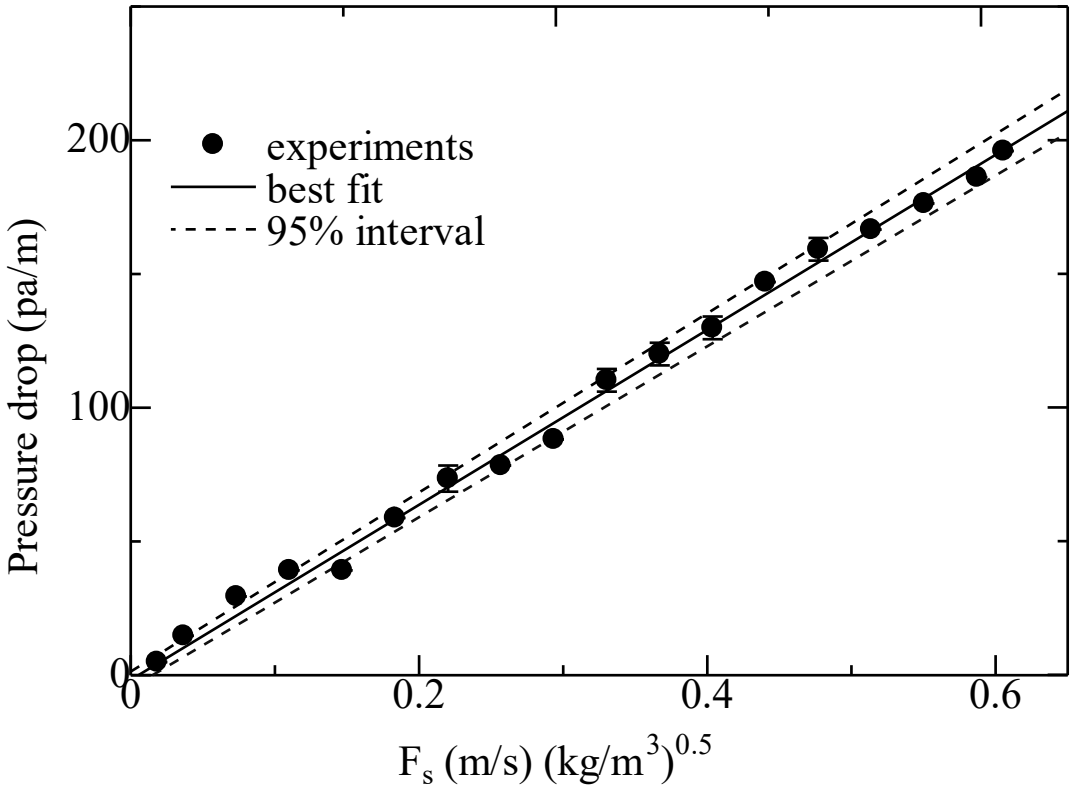

Figure 6.11: Dry pressure drop versus the gas capacity factor for Dixon rings $^1/_4$ in. The circles represent the experimental data, the solid line is the linear regression of the data and the dashed lines represent the 95th-centile confidence interval in the data. Each data point shows the corresponding error due to each measurement.

Table 6.1: Calculated parameters for dry pressure drop for Dixon rings $^1/_4$ in and Dixon rings $^5/_8$ in.

Packing (in)	Gradient ($Pa.m^{-1}$)		Intercept ($Pa.m^{-1}$)	
	$CCI_{Grad,95,th}$	SE_{Grad}	$CCI_{Grad,95,th}$	SE_{Inter}
Dixon $^5/_8$	12.1	±1.93	0.015	±0.79
Dixon $^1/_4$	74.8	±4.84	1.13	±1.56

In Table 6.1, SE for the gradient and the intercept for the dry pressure drop for Dixon rings $^1/_4$ in and $^5/_8$ in are highlighted**.** As demonstrated in Table 6.1, the SE for the gradient and intercept were low for Dixon rings $^1/_4$ in Dixon rings $^5/_8$ in , which shows that this model can accurately describe the gradient. The confidence interval values CCI_{95th} in Table 6.1 was calculated using equations (6.2) and (6.3)(6.3). The standard errors (SE) which are calculated using equations (6.4) and (6.5). The Standard of the intercept SE_{Inter} are very low, less than 2%. However, in this case, the intercept should be zero when no gas is flowing. The error was calculated based on the zero-intercept resulting in high percentage error, but the interval's bounds do not include zero. This indicates that the model may not be able to adequately describe the pressure drop when the gas flowrate is small.

6.4.2 Loading point determination

The loading point pressure drop is a simple linear correlation that is a function of the liquid and gas flowrates, as described in Figure 6.12 and Figure 6.13. The solid line is the best fit, and the dashed line is generated using equations (6.6) and (6.7).

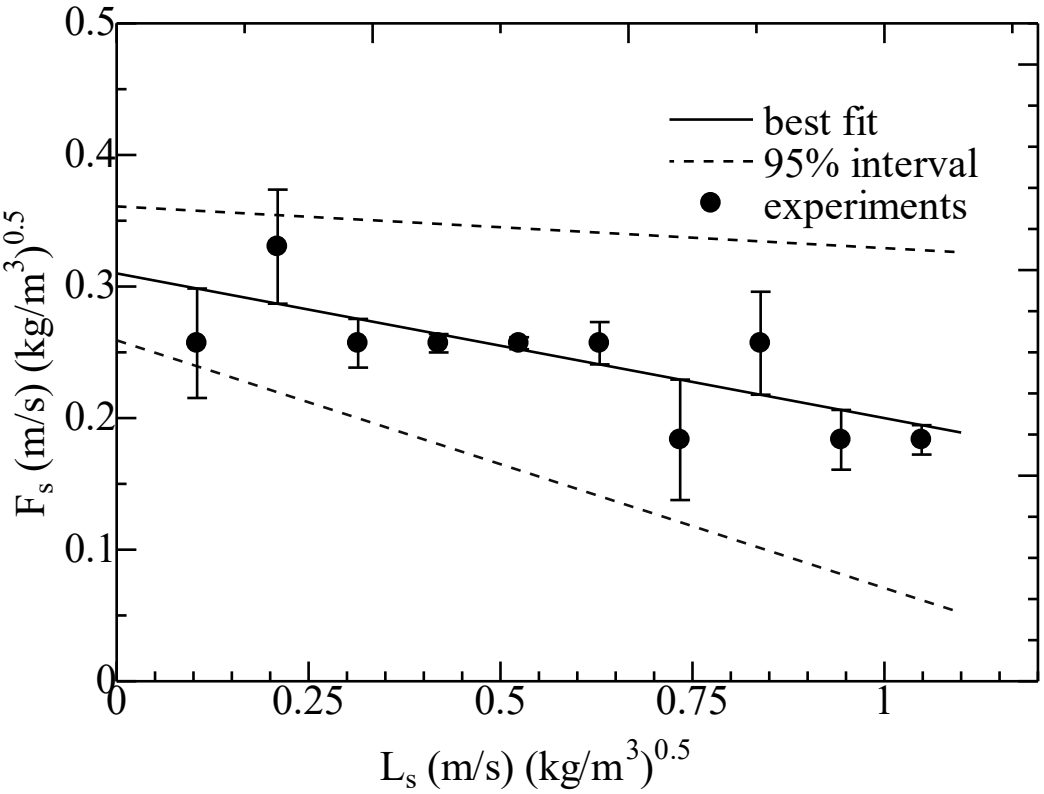

Figure 6.12: Loading point model for Dixon rings $^5/_8$ in, the liquid capacity factor versus the gas packing factor. The black data points represent the experimental data, the solid line is the linear regression of the data and the dotted lines represent the 95th-centile confidence interval in the data. Each data point shows the corresponding experimental error.

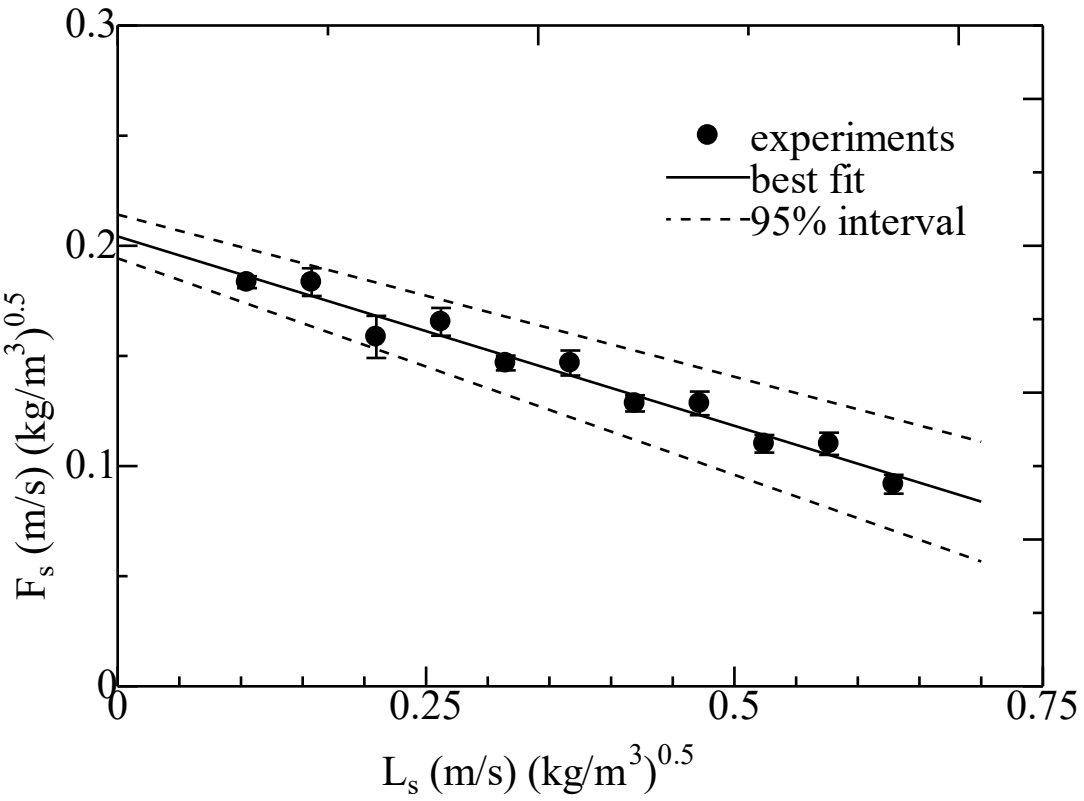

Figure 6.13: Loading point model for Dixon rings $^1/_4$ in represented as the liquid capacity factor versus the gas capacity factor. The data points represent the experimental data, the solid line is the linear regression of the data and the dotted lines represent the 95th-centile confidence interval in the data. Each data point shows the corresponding experimental error.

Table 6.2: Calculated parameters for the estimation of the loading pressure drop

Packing (in)	Gradient (Pa.m^{-1})		Intercept (Pa.m^{-1})	
	$CCI_{Grad,95,th}$	SE_{Grad}	$CCI_{Grad,95,th}$	SE_{Inter}
Dixon $^5/_8$	33.8	± 2.9	53.3	± 1.89
Dixon $^1/_4$	-1.7	± 0.02	2.0	± 0.01

A model was developed to predict the pressure drop at which the loading occurs for a given gas and liquid flowrate. The confidence interval values CCI_{95th} in Table 6.2 was calculated using

equations (6.2) and (6.3). The standard errors SE which are calculated using equations (6.4) and (6.5). The standard error for the gradient and the intercept uncertainties are very low, which indicates that the model is adequate to use to predict the loading region.

In conclusion, the pressure drop, liquid holdup, and mass transfer were investigated for the first time. Dixon rings of the size $^5/_8$ in and $^1/_4$ in. Dixon rings $^5/_8$ in were found to have the lowest pressure drop compared to other commercial packing. Dixon rings $^5/_8$ and $^1/_4$ in were found to have K_{Ga} value at the liquid load 23.88 ($m^3.m^{-2}$ hr^{-1}) were 0.55 and 2 (kg-kmol/($hr.m^3$.atm)), respectively. In addition to the experimental results, models were developed to calculate the dry pressure drop and loading point. The models had SE less than 5% and 3% for the dry pressure drop and loading point, respectively. Therefore, the model is reliable for the implementation for Dixon rings.

7 Chapter 7: Conclusion and future work

7.1 Review of the work

Packed columns are used in many separation applications such as water treatment and hydrocracking. The packing material interacts with the fluid through a column creating a pressure drop that affects the transfer phenomena. Dixon rings are random packing made from stainless steel metallic mesh rolled into a cylindrical shape. The physical structure of Dixon rings has the potential for high mixing abilities compared to other random packings. Dixon rings offer pore openings in the wire mesh and a larger surface area which may result in lower pressure drop. One method to improve the liquid distribution for Dixon rings is through developing uniform surface coatings of hydrophobic or hydrophilic properties. A uniform coating can change the structure of the surface composition; therefore, it reflects a change in the surface energy and the contact angles. However, the complex geometry of the Dixon rings hinders application where a coating is required.

The liquid dispersion and the wetting efficiency are critical parameters in the design and operation of packed columns. Studying these parameters on a large scale is impossible due to the computational limitations or expensive imaging techniques. However, studying these parameters at a microscale helps understand fluid patterns at a larger scale. The option was to design packing for gas-liquid separation applications with a tunable wetting efficiency. The liquid flow over a single Dixon ring was studied using laboratory imaging experiments and 3D simulations. The investigation was conducted on a single wire mesh uncoated and surface-modified Dixon ring with an alumina coating. The results of the VOF model were validated by imaging the flow using a CCD camera and by a grid test simulation solution independent of the number of cells.

Packings are usually evaluated based on hydrodynamic parameters such as pressure drop, liquid hold up, and mass transfer rate. The hydrodynamic parameters for Dixon rings packing are not known. The hydrodynamics were tested in a semi-pilot plant for Dixon rings packing $^5/_8$ in and $^1/_4$ in for a range of gas and liquid flow rates for counter-current operation. The performance of Dixon rings was compared to commercial packing gathered from the pressure drop, liquid holdup and mass transfer models of Stichlmar, Mackowiak, and Wagner, respectively. The 95^{th} centile

confidence interval models were developed to describe the dry pressure drop, and loading points were evaluated for all models.

7.2 The results achieved in this work

In Chapter 4**,** well-adhered alumina with a thickness of up to 20 µm was deposited on Dixon rings using a simple sol-gel coating technique. To overcome the difficulties associated with coating the stainless steel with complex geometry and achieve excellent adhesion, the effects of the initial composition on the coating properties were investigated. The ratios of 0.25 (mol/mol) for HCl/Al, 0.01 (mol/mol) for Al/H_2O, 48 h for the aging time, 96 h for the mixing time and 2.1 g/L of PEI binder formed a controlled and suitable coating of alumina on the Dixon ring. The coating was found free of microscopic cracks. Increasing the thickness was successfully achieved through multiple cycles. It was found that two cycles were suitable, meeting the viscosity boundary of 0.0035 (Pa.s).

In Chapter 5, the pore-scale flow for Dixon rings was testedusing visual experiments and CFD simulations. A cycle of droplet flow over an uncoated Dixon ring exhibited penetration of the hydrophilic mesh openings, adherence to the surface of the ring, obstruction by the horizontal grid at the centre of the ring and accumulation at the bottom region of the Dixon rings. The adherence of the droplet confirmed the hydrophilic nature of the Dixon ring. The cycle of the droplet interaction with the uncoated hydrophobic Dixon ring exhibited accumulation of the droplet at the top surface of the ring, where the thickness of liquid reached a maximum value. This has promoted the gravitational forces and led the droplet to slip over the vertical curvature to the bottom surface of the ring without any penetration inside the ring. Experiments and CFD simulations obtained the droplet profiles for the coated and uncoated rings, and these were in reasonable agreement which allowed the further parametric study of the impact of the flow and contact angle on the wetting efficiency, liquid holdup, and effective surface area. The uncoated Dixon rings were found to have a contact angle of 60°, describing a hydrophilic packing nature, promoting the wetting efficiency by making the droplet spread over it. The coated rings were shown to be hydrophobic (contact angle of 105°), promoting repellence of the droplets. The time needed to reach the steady-state decreased when the liquid inlet velocity was increased or the contact angle was decreased. High flow rates destabilised the liquid stream by delaying the outer layers of flow concerning the inner ones, driving the cohesive molecular forces to become tenuous. The 3D CFD model confirmed the

increase in the wetting efficiency, liquid holdup, and effective surface area with increased liquid flowrate and reduced contact angle, in reasonable agreement with Stichlmair's model, particularly in the hydrophilic zone of the contact angle and low W_e and Linek's model, particularly in the hydrophobic range of the contact angle. This was driven by the development of a uniform thickness film of over the coated ring and by an increase in the thickness and length of the droplet over the uncoated rings. The high wetting efficiency and the uncoated Dixon rings' hydrophilic nature can reduce the packed columns' operational condition. The hydrophobic coatings can be implemented in gas-liquid separation processes that require high mixing in packed beds.

In Chapter 6, the hydrodynamic properties for Dixon rings were tested in a semi-pilot plant. Dixon rings $^1/_4$ in were found to have a low-pressure drop, 100 % less than Dixon rings $^5/_8$ in. Due to the lateral opening, commercial Pall rings were found to have lower pressure drop than Dixon rings. The liquid holdup for Dixon rings $^1/_4$ in was found to have a value of 0.5 at L_s 0.2 (m/s) $(kg/m^3)^{0.5}$. On the other hand, Reflux rings $^5/_8$ in was found to offer the lowest liquid holdup with a value of 0.25. Dixon rings $^1/_4$ in were found to have the highest separation efficiency with HETP of 0.05 compared to Pall rings which had HETP value of 0.5. The SE was less than 5 % and 2 % for the gradient and intercepted, respectively. For the loading point, SE values were less than 3 % and 2 %, respectively. It was suggested that the models are valid for calculating the dry pressure drops and loading regions in various applications of Dixon rings packing.

7.3 Future recommendations

7.3.1 CFD model

This thesis successfully investigated the hydrodynamics for Dixon rings at microscopic and macroscopic scales for the uncoated Dixon rings, and the results were validated and compared with those in the literature. The microscopic study was conducted for a single element of the Dixon rings which included developing a CFD model and visual experiments. Developing a model based on several elements would be more realistic but Dixon rings have complex geometry and the number of elements required for meshing is high, thus leading the computational costs to be expensive and directed towards a separate scope of work. Due to the time constraints, some elements of this research are worthy of further investigation.

7.3.2 Coated Dixon rings

A study of the sol-gel coating on the Dixon rings was successfully conducted. The coated Dixon rings were implemented to study the microscopic flow due to the limitation in the experimental facilities and the cost of the project. The current semi-pilot plant used in the investigation would require thousands of coated Dixon rings, and the sol-gel dip-coating procedure used in this thesis produces sixteen Dixon rings per batch. Therefore, hundreds of batches would be needed to conduct the study on the coated rings. A scale-up study for the sol-gel coating procedure for coating Dixon rings with alumina is highly desirable. The fluid flow should be tested on a macroscopic level for coated Dixon rings to gain a better insight into the effects of coating on the hydrodynamics and mass transfer phenomena.

Appendix A

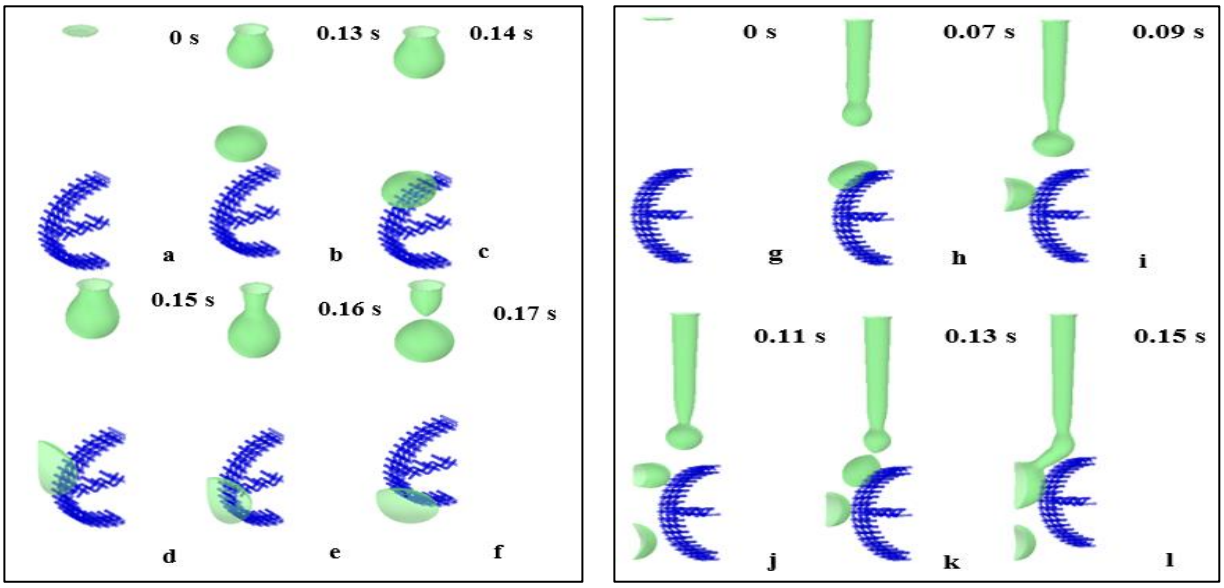

Figure A1 : Flow pattern of VOF = 0.5 for Dixon rings using the grid GR2, for coated rings, θ = 105° for u_o = 0.15 m/s: (a) 0 s, (b) 0.13 s, (c) 0.14 s, (d) 0.15 s, (e) 0.16 s and (f) 0.17 s, and , and u_o = 0.25 m/s: (g) 0 s, (h) 0.07 s, (i) 0.09 s, (j) 0.11 s, (k) 0.13 s and (l) 0.15 s.

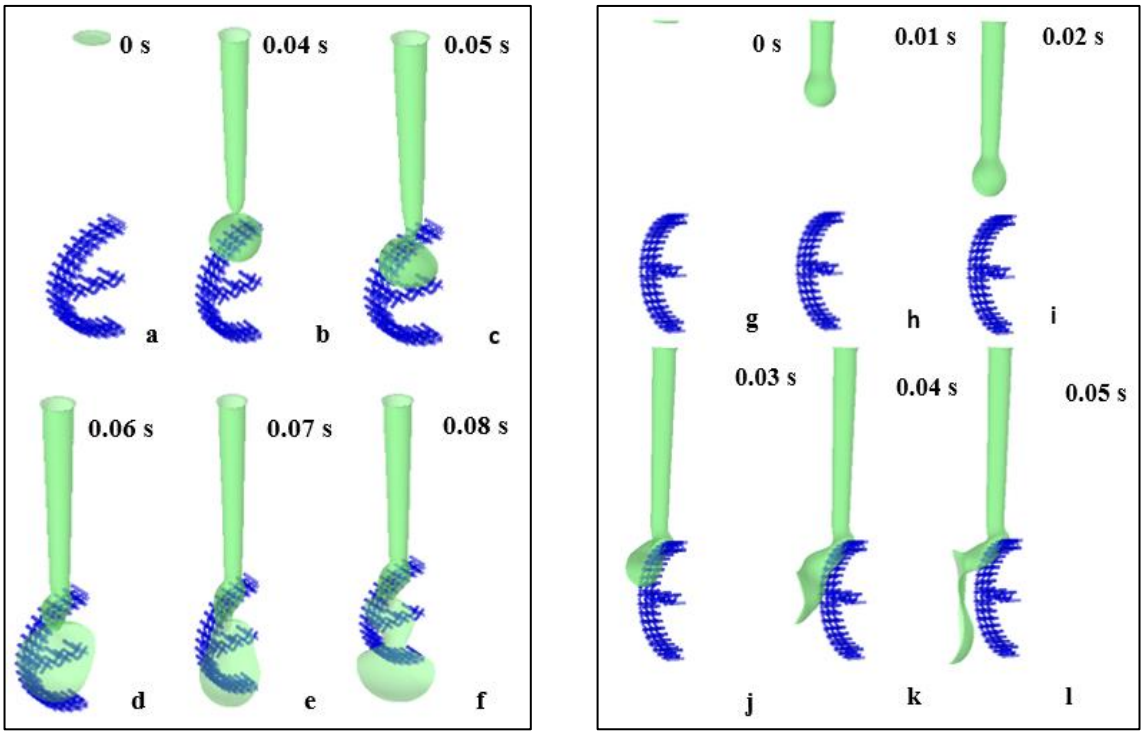

Figure A2 : Flow pattern of VOF = 0.5 for Dixon rings using the grid GR2, u_o = 0.35 m/s for coated rings, θ = 105°: (a) 0 s, (b) 0.04 s, (c) 0.05 s, (d) 0.06 and (e) 0.07 s and (f) 0.08 s. °: uo = 0.5 m/s (g) 0 s, (h) 0.01 s, (i) 0.02 s, (j) 0.03 and (k) 0.04 s and (l) 0.05

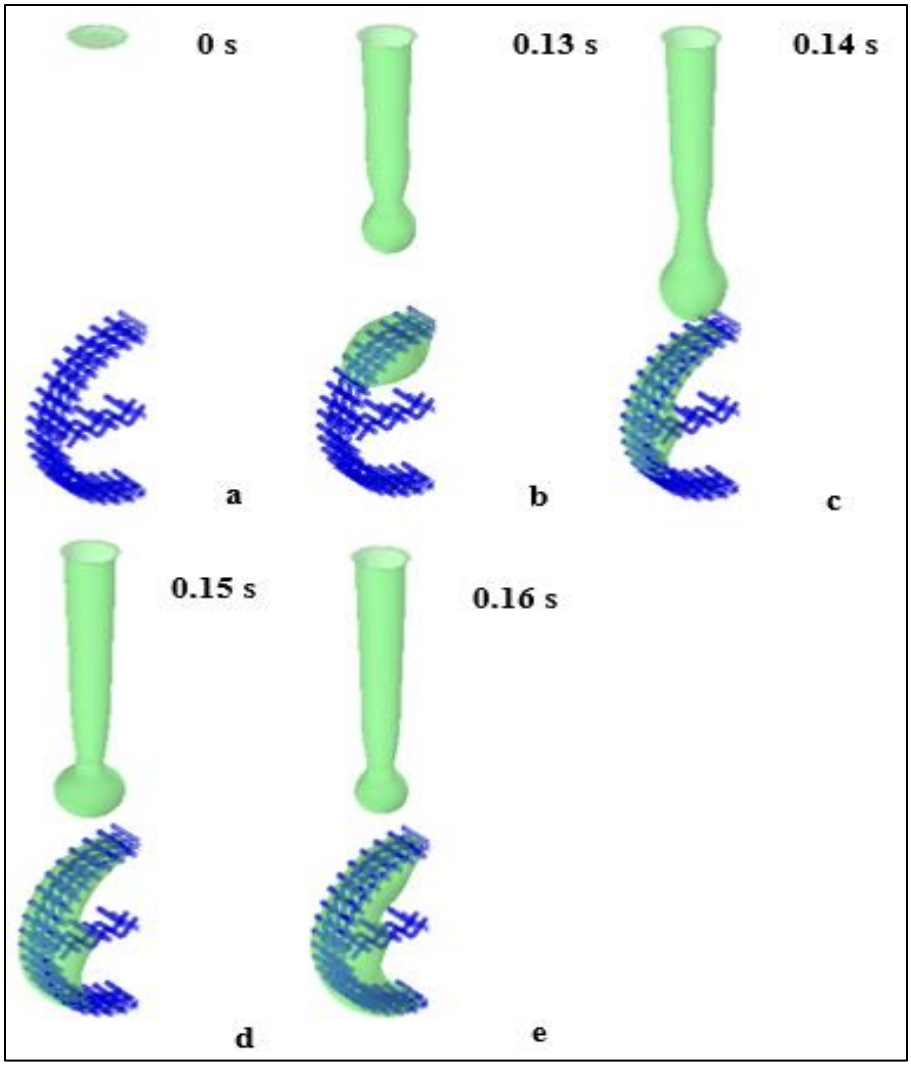

Figure A3: Flow pattern of VOF = 0.5 for Dixon rings using the grid GR2, u_0 = 0.25 m/s for uncoated rings, θ = 60°: (a) 0 s, (b) 0.13 s, (c) 0.14 s, (d) 0.15 s, (e) 0.16 s.

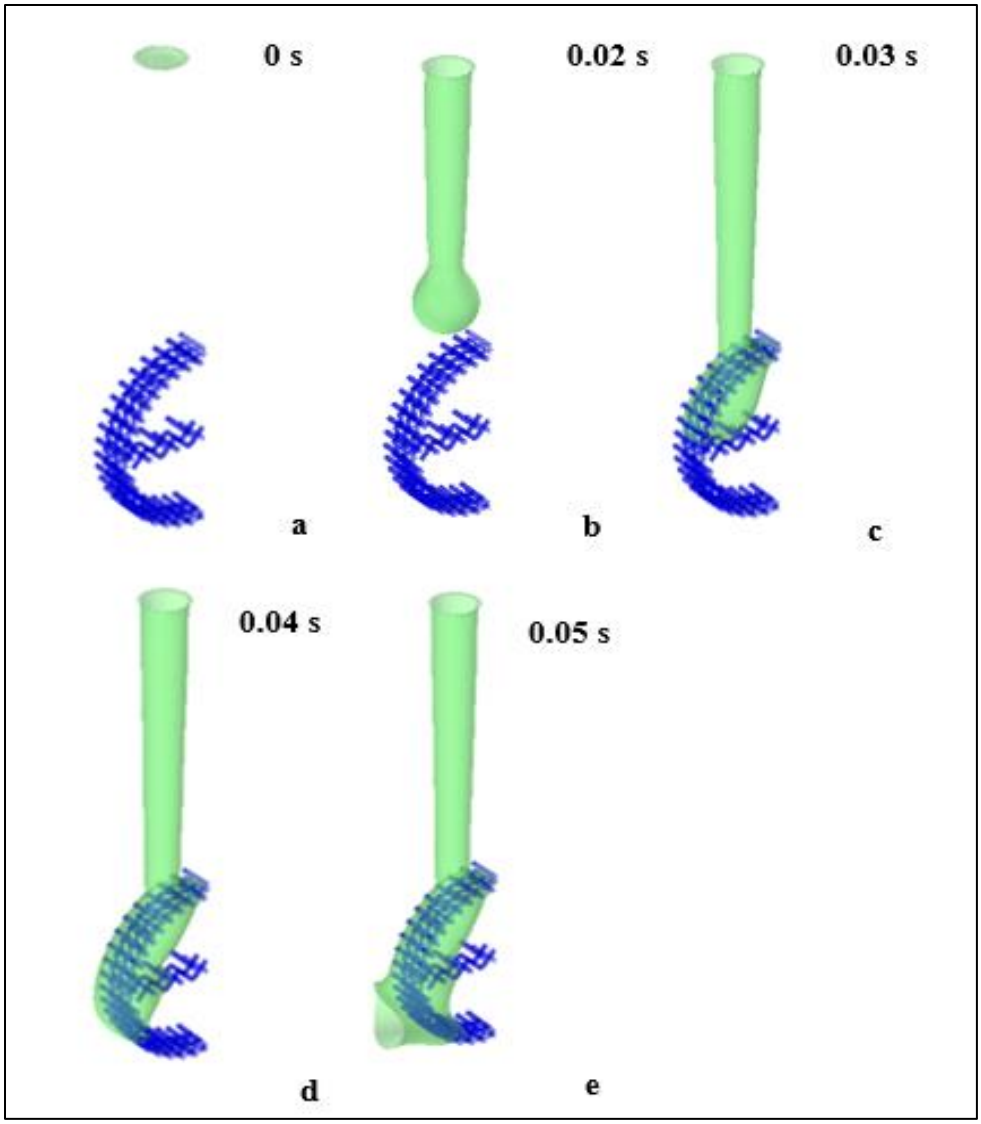

Figure A4: Flow pattern of VOF = 0.5 for Dixon rings using the grid GR2, u_o = 0.5 m/s for uncoated rings, θ = 60°: (a) 0 s, (b) 0.01 s, (c) 0.02 s, (d) 0.03 and (e) 0.04.

References

[1] P. Yan, X. Li, H. Li, Y. Shao, H. Zhang, X. Gao, Hydrodynamics and mechanism of hydrophobic foam column tray: Contact angle hysteresis effect, AIChE J. 66 (2020) 1–11. https://doi.org/10.1002/aic.16793.

[2] K. Fu, W. Rongwong, Z. Liang, Y. Na, R. Idem, P. Tontiwachwuthikul, Experimental analyses of mass transfer and heat transfer of post-combustion CO_2 absorption using hybrid solvent MEA-MeOH in an absorber, Chem. Eng. J. 260 (2015) 11–19. https://doi.org/10.1016/j.cej.2014.08.064.

[3] M. Abdelraouf, J. Hegarty, A. Rennie, R. Elizalde, N. Burns, Sol-gel alumina coating of wired mesh packing, Ceram. Int. (2020). https://doi.org/10.1016/j.ceramint.2020.05.043.

[4] J.T. Yeh, H.W. Pennline, K.P. Resnik, Study of CO_2 Absorption and Desorption in a Packed Column, Energy and Fuels. 15 (2001) 274–278. https://doi.org/10.1021/ef0002389.

[5] M. Abdelraouf, A. Rennie, N. Burns, L. Geekie, V. Najdanovic-Visak, F. Aiouache, Tuning the wettability of wire mesh column: pore-scale flow analysis, Chem. Eng. J. Adv. 8 (2021) 100181. https://doi.org/10.1016/j.ceja.2021.100181.

[6] D. Truyen, M. Courty, P. Alphonse, F. Ansart, Catalytic coatings on stainless steel prepared by sol-gel route, Thin Solid Films. 495 (2006) 257–261. https://doi.org/10.1016/j.tsf.2005.08.200.

[7] A.N. Bukin, V.S. Moseeva, A. V. Ovcharov, S.A. Marunich, Y.S. Pak, M.B. Rozenkevich, Mass transfer and hydrodynamics in a mixed bed of a hydrophobic catalyst and a hydrophilic packing, Fusion Eng. Des. 171 (2021) 112595. https://doi.org/10.1016/j.fusengdes.2021.112595.

[8] M. Zivdar, M. Haghshenas Fard, R.G.H. Prince, Evaluation of pressure drop and mass-transfer characteristics of a structured packing for production and separation of food flavours Part I: Pressure drop characteristics, Food Bioprod. Process. 84 (2006) 200–205. https://doi.org/10.1205/fbp.04002.

[9] P. Alix, L. Raynal, Pressure drop and mass transfer of a high capacity random packing.

Application to CO2 post-combustion capture, Energy Procedia. 1 (2009) 845–852. https://doi.org/10.1016/j.egypro.2009.01.112.

[10] E. Dumont, A. Couvert, A. Amrane, C. Couriol, G. Darracq, P. Le Cloirec, Equivalent Absorption Capacity (EAC) concept applied to the absorption of hydrophobic VOCs in a water/PDMS mixture, Chem. Eng. J. 287 (2016) 205–216. https://doi.org/10.1016/j.cej.2015.11.020.

[11] I. Mamaliga, D. Sidor, C. Condurat, E.T. Iacob Tudose, Hydrodynamics and mass transfer coefficients for a modified Raschig ring packed column, Heat Mass Transf. Und Stoffuebertragung. 50 (2014) 1385–1392. https://doi.org/10.1007/s00231-014-1324-2.

[12] J. Lévêque, D. Rouzineau, M. Prévost, M. Meyer, Hydrodynamic and mass transfer efficiency of ceramic foam packing applied to distillation, Chem. Eng. Sci. 64 (2009) 2607–2616. https://doi.org/10.1016/j.ces.2009.02.010.

[13] Y. Jiang, M.R. Khadilkar, M.H. Al-Dahhan, M.P. Dudukovic, CFD modeling of multiphase flow distribution in catalytic packed bed reactors: Scale down issues, Catal. Today. 66 (2001) 209–218.

[14] K.H. Javed, T. Mahmud, E. Purba, Enhancement of mass transfer in a spray tower using swirling gas flow, Chem. Eng. Res. Des. 84 (2006) 465–477. https://doi.org/10.1205/cherd.05119.

[15] Z. Guo, Z. Sun, N. Zhang, M. Ding, J. Liu, Pressure drop in slender packed beds with novel packing arrangement, Powder Technol. 321 (2017) 286–292. https://doi.org/10.1016/j.powtec.2017.08.024.

[16] M. Han, H. Lin, Y. Yuan, D. Wang, Y. Jin, Pressure drop for two phase counter-current flow in a packed column with a novel internal, Chem. Eng. J. 94 (2003) 179–187. https://doi.org/10.1016/S1385-8947(03)00059-7.

[17] A. Setameteekul, A. Aroonwilas, A. Veawab, Statistical factorial design analysis for parametric interaction and empirical correlations of CO2absorption performance in MEA and blended MEA/MDEA processes, Sep. Purif. Technol. 64 (2008) 16–25. https://doi.org/10.1016/j.seppur.2008.09.002.

[18] Ž. Olujić, Effect of column diameter on pressure drop of a corrugated sheet structured packing, Chem. Eng. Res. Des. 77 (1999) 505–510. https://doi.org/10.1205/026387699526539.

[19] A.K. Jammula, New Liquid Holdup, Load Point and Flooding Velocity Models in Different Regions of Operations for a Structured Packed Column, (2014) 282.

[20] R. Stockfleth, G. Brunner, Holdup, pressure drop, and flooding in packed countercurrent columns for the gas extraction, Ind. Eng. Chem. Res. 40 (2001) 347–356. https://doi.org/10.1021/ie000466q.

[21] N. Kolev, Packed Bed Columns for: absorption, desorption, rectification and direct heat transfer, Chapter 3: Industrial packing, Elsevier., Amsterdam, 2006, pp. 149–441. https://doi.org/10.1016/b978-044452829-2/50005-4

[22] R. Billet, J. Maćkowiak, How to Use the Absorption Data for Design and Scale-Up of Packed Columns, Fette, Seifen, Anstrichm. 86 (1984) 349–358. https://doi.org/10.1002/lipi.19840860905.

[23] L. Sang, J. Tu, H. Cheng, G. Luo, J. Zhang, Hydrodynamics and mass transfer of gas–liquid flow in micropacked bed reactors with metal foam packing, AIChE J. 66 (2020) 15–17. https://doi.org/10.1002/aic.16803.

[24] X. Zhao, K.H. Smith, M.A. Simioni, W. Tao, S.E. Kentish, W. Fei, G.W. Stevens, Comparison of several packings for CO2 chemical absorption in a packed column, Int. J. Greenh. Gas Control. 5 (2011) 1163–1169. https://doi.org/10.1016/j.ijggc.2011.07.006.

[25] J. Neukäufer, N. Sarajlic, H. Klein, S. Rehfeldt, H. Hallmann, C. Knösche, T. Grützner, Flexible distillation test rig on a laboratory scale for characterization of additively manufactured packings, AIChE J. 67 (2021) 1–11. https://doi.org/10.1002/aic.17381.

[26] R. Billet, M. Schultes, Modelling of pressure drop in packed columns, Chem. Eng. Technol. 14 (1991) 89–95. https://doi.org/10.1002/ceat.270140203.

[27] S. Bolton, A. Kasturi, S. Palko, C. Lai, L. Love, J. Parks, S. Xin, C. Tsouris, 3D printed structures for optimized carbon capture technology in packed bed columns, Sep. Sci. Technol. 54 (2019) 2047–2058. https://doi.org/10.1080/01496395.2019.1622566.

[28] J. Maćkowiak, Pressure drop in irrigated packed columns, Chem. Eng. Process. 29 (1991) 93–105. https://doi.org/10.1016/0255-2701(91)87018-X.

[29] B. Xu, H. Gao, X. Luo, H. Liao, Z. Liang, Mass transfer performance of CO2absorption into aqueous DEEA in packed columns, Int. J. Greenh. Gas Control. 51 (2016) 11–17. https://doi.org/10.1016/j.ijggc.2016.05.004.

[30] L. Wen, H. Liu, W. Rongwong, Z. Liang, K. Fu, R. Idem, P. Tontiwachwuthikul, Comparison of Overall Gas-Phase Mass Transfer Coefficient for CO_2 Absorption between Tertiary Amines in a Randomly Packed Column, Chem. Eng. Technol. 38 (2015) 1435–1443. https://doi.org/10.1002/ceat.201400606.

[31] M. Sheng, C. Liu, C. Ge, M. Arowo, Y. Xiang, B. Sun, G. Chu, H. Zou, Mass-Transfer Performance of CO2Absorption with Aqueous Diethylenetriamine-Based Solutions in a Packed Column with Dixon Rings, Ind. Eng. Chem. Res. 55 (2016) 10788–10793. https://doi.org/10.1021/acs.iecr.6b02280.

[32] L.B. Hunt, The early history of gold plating, Gold Bull. 6 (1973) 16–27. https://doi.org/10.1007/bf03215178.

[33] T.P. Chou, C. Chandrasekaran, S.J. Limmer, S. Seraji, Y. Wu, M.J. Forbess, C. Nguyen, G.Z. Cao, Organic-inorganic hybrid coatings for corrosion protection, J. Non. Cryst. Solids. 290 (2001) 153–162. https://doi.org/10.1016/S0022-3093(01)00818-3.

[34] R. Figueira, I. Fontinha, C. Silva, E. Pereira, Hybrid Sol-Gel Coatings: Smart and Green Materials for Corrosion Mitigation, Coatings. 6 (2016) 12. https://doi.org/10.3390/coatings6010012.

[35] L. Giani, C. Cristiani, G. Groppi, E. Tronconi, Washcoating method for Pd/γ-Al2O3 deposition on metallic foams, Appl. Catal. B Environ. 62 (2006) 121–131. https://doi.org/10.1016/j.apcatb.2005.07.003.

[36] J. Ma, Electrophoretic deposition of lead zirconate titanate ceramics, J. Am. Ceram. Soc. 37 (2002) 1735–1737. https://doi.org/10.1111/j.1151-2916.2002.tb00344.x.

[37] J. Masalski, J. Gluszek, J. Zabrzeski, K. Nitsch, P. Gluszek, Improvement in corrosion resistance of the 316l stainless steel by means of Al< sub> 2</sub> O< sub> 3</sub>

coatings deposited by the sol-gel method, Thin Solid Films. 349 (1999) 186–190. https://doi.org/10.1016/s0040-6090(99)00230-8.

[38] O. Sanz, E.D. Banús, A. Goya, H. Larumbe, J.J. Delgado, A. Monzón, M. Montes, Stacked wire-mesh monoliths for VOCs combustion: Effect of the mesh-opening in the catalytic performance, Catal. Today. 296 (2017) 76–83. https://doi.org/10.1016/j.cattod.2017.05.054.

[39] M. Valentini, G. Groppi, C. Cristiani, M. Levi, E. Tronconi, P. Forzatti, The deposition of γ-Al2O3 layers on ceramic and metallic supports for the preparation of structured catalysts, Catal. Today. 69 (2001) 307–314. https://doi.org/10.1016/S0920-5861(01)00383-2.

[40] L. Sang, B. Sun, H. Tan, C. Du, Y. Wu, C. Ma, Catalytic reforming of methane with CO2over metal foam based monolithic catalysts, Int. J. Hydrogen Energy. 37 (2012) 13037–13043. https://doi.org/10.1016/j.ijhydene.2012.05.056.

[41] K. Shik, Z. Jiang, J. Shik, Electrophoretically Al-coated wire mesh and its application for catalytic oxidation of 1 , 2-dichlorobenzene, Science (80-.). 168 (2003) 103–110.

[42] V. Meille, S. Pallier, P. Rodriguez, Reproducibility in the preparation of alumina slurries for washcoat application-Role of temperature and particle size distribution, Colloids Surfaces A Physicochem. Eng. Asp. 336 (2009) 104–109. https://doi.org/10.1016/j.colsurfa.2008.11.029.

[43] B. Song, Simple and fast fabrication of superhydrophobic metal wire mesh for efficiently gravity-driven oil/water separation, Mar. Pollut. Bull. 113 (2016) 211–215. https://doi.org/10.1016/j.marpolbul.2016.09.010.

[44] M.J. Su, S. Bai, Y. Luo, G.W. Chu, B.C. Sun, Y. Le, J.F. Chen, Controllable wettability on stainless steel substrates with highly stable coatings, Chem. Eng. Sci. 195 (2019) 791–800. https://doi.org/10.1016/j.ces.2018.10.025.

[45] F. Zhang, Z. Shi, L. Chen, Y. Jiang, C. Xu, Z. Wu, Y. Wang, C. Peng, Porous superhydrophobic and superoleophilic surfaces prepared by template assisted chemical vapor deposition, Surf. Coatings Technol. 315 (2017) 385–390.

https://doi.org/10.1016/j.surfcoat.2017.02.058.

[46] R. Xing, Y. Rao, W. TeGrotenhuis, N. Canfield, F. Zheng, D.W. Winiarski, W. Liu, Advanced thin zeolite/metal flat sheet membrane for energy efficient air dehumidification and conditioning, Chem. Eng. Sci. 104 (2013) 596–609. https://doi.org/10.1016/j.ces.2013.08.061.

[47] R.L. Vander Wal, L.J. Hall, Carbon nanotube synthesis upon stainless steel meshes, Carbon N. Y. 41 (2003) 659–672. https://doi.org/10.1016/S0008-6223(02)00369-X.

[48] F.J. Maldonado-Hódar, M.A. Ferro-García, J. Rivera-Utrilla, C. Moreno-Castilla, Synthesis and textural characteristics of organic aerogels, transition-metal-containing organic aerogels and their carbonized derivatives, Carbon N. Y. 37 (1999) 1199–1205. https://doi.org/10.1016/S0008-6223(98)00314-5.

[49] F. Cernuschi, L. Lorenzoni, S. Capelli, C. Guardamagna, M. Karger, R. Vaßen, K. von Niessen, N. Markocsan, J. Menuey, C. Giolli, Solid particle erosion of thermal spray and physical vapour deposition thermal barrier coatings, Wear. 271 (2011) 2909–2918. https://doi.org/10.1016/j.wear.2011.06.013.

[50] S. Takeda, S. Suzuki, H. Odaka, H. Hosono, Photocatalytic TiO2 thin film deposited onto glass by DC magnetron sputtering, Thin Solid Films. 392 (2001) 338–344. https://doi.org/10.1016/S0040-6090(01)01054-9.

[51] H. Sun, Y. Shu, X. Quan, S. Chen, B. Pang, Z.Y. Liu, Experimental and modeling study of selective catalytic reduction of NOxwith NH3over wire mesh honeycomb catalysts, Chem. Eng. J. 165 (2010) 769–775. https://doi.org/10.1016/j.cej.2010.09.057.

[52] S.H. Lee, S.W. Yang, E.S. Park, J.Y. Hwang, D.S. Lee, High-performance adhesives based on maleic anhydride-g-EPDM rubbers and polybutene for laminating cast polypropylene film and aluminum foil, Coatings. 9 (2019). https://doi.org/10.3390/coatings9010061.

[53] H.J. John, C.E. Rehberg, Simplified Wire-Screen Packing for Fractionating Columns, Ind. Eng. Chem. 41 (1949) 1056–1058. https://doi.org/10.1021/ie50473a037.

[54] F. Zhang, Z. Shi, C. Xu, D. Huo, W. Zhang, C. Peng, Self-fibering growth in the soot-

templated CVD coating of silica on mesh for efficient oil/water separation, Mater. Des. 154 (2018) 370–377. https://doi.org/10.1016/j.matdes.2018.05.038.

[55] M. Dvořáková, R. Perekrestov, P. Kšírová, J. Balabánová, K. Jirátová, J. Maixner, P. Topka, J. Rathouský, M. Koštejn, M. Čada, Z. Hubička, F. Kovanda, Preparation of cobalt oxide catalysts on stainless steel wire mesh by combination of magnetron sputtering and electrochemical deposition, Catal. Today. 334 (2019) 13–23. https://doi.org/10.1016/j.cattod.2019.03.008.

[56] L. Besra, M. Liu, A review on fundamentals and applications of electrophoretic deposition (EPD), Prog. Mater. Sci. 52 (2007) 1–61. https://doi.org/10.1016/j.pmatsci.2006.07.001.

[57] G. Wang, P. Sarkar, P.S. Nicholson, Influence of Acidity on the Electrostatic Stability of Alumina Suspensions in Ethanol, J. Am. Ceram. Soc. 80 (1997) 965–972. https://doi.org/10.1111/j.1151-2916.1997.tb02928.x.

[58] H. Sun, X. Quan, S. Chen, H. Zhao, Y. Zhao, Preparation of well-adhered γ-Al2O3washcoat on metallic wire mesh monoliths by electrophoretic deposition, Appl. Surf. Sci. 253 (2007) 3303–3310. https://doi.org/10.1016/j.apsusc.2006.07.044.

[59] M.P. Vorob'eva, A.A. Greish, A. V. Ivanov, L.M. Kustov, Preparation of catalyst carriers on the basis of alumina supported on metallic gauzes, Appl. Catal. A Gen. 199 (2000) 257–261. https://doi.org/10.1016/S0926-860X(99)00563-3.

[60] M. Guglielmi, Sol-Gel Coatings on Metals, J. Sol-Gel Sci. Technol. 8 (1997) 443–449. https://doi.org/10.1007/BF02436880.

[61] Y. Dimitriev, Y. Ivanova, R. Iordanova, ChemInform Abstract: History of Sol-Gel Science and Technology, ChemInform. 40 (2009) 181–192. https://doi.org/10.1002/chin.200912249.

[62] J. Zarzycki, Past and Present of Sol-Gel Science and Technology, J. Sol-Gel Sci. Technol. 8 (1997) 17–22. https://doi.org/10.1007/BF02436811.

[63] C.J. Brinker, A.J. Hurd, P.R. Schunk, G.C. Frye, C.S. Ashley, Review of sol-gel thin film formation, J. Non. Cryst. Solids. 147–148 (1992) 424–436. https://doi.org/10.1016/S0022-3093(05)80653-2.

[64] J. Livage, Sol-gel processes, Curr. Opin. Solid State Mater. Sci. 2 (1997) 132–138. https://doi.org/10.1016/s1359-0286(97)80057-5.

[65] J. Livage, C. Sanchez, Sol-gel chemistry, J. Non. Cryst. Solids. 145 (1992) 11–19. https://doi.org/10.1016/S0022-3093(05)80422-3.

[66] M. Abdelraouf, J. Hegarty, A. Rennie, R. Elizalde, N. Burns, L. Geekie, V. Najdanovic-Visak, F. Aiouache, Sol-gel alumina coating of wire mesh packing, Ceram. Int. 46 (2020) 20777–20787. https://doi.org/10.1016/j.ceramint.2020.05.043.

[67] B.D. Fabes, D.P. Birnie, B.J.J. Zelinski, Porosity and composition effects in sol-gel derived interference filters, Thin Solid Films. 254 (1995) 175–180. https://doi.org/10.1016/0040-6090(94)06244-F.

[68] S.D. Bhagat, Y. Kim, Y. Ahn, Room temperature synthesis of water repellent silica coatings by the dip coat technique, APSUSC. 253 (2006) 2217–2221. https://doi.org/10.1016/j.apsusc.2006.04.030.

[69] E.D. Banús, O. Sanz, V.G. Milt, E.E. Miró, M. Montes, Development of a stacked wire-mesh structure for diesel soot combustion, Chem. Eng. J. 246 (2014) 353–365. https://doi.org/10.1016/j.cej.2014.02.086.

[70] D.L. Marchisio, F. Omegna, A.A. Barresi, P. Bowen, Effect of mixing and other operating parameters in sol-gel processes, Ind. Eng. Chem. Res. 47 (2008) 7202–7210. https://doi.org/10.1021/ie800217b.

[71] M. Faustini, B. Louis, P.A. Albouy, M. Kuemmel, D. Grosso, Preparation of sol-gel films by dip-coating in extreme conditions, J. Phys. Chem. C. 114 (2010) 7637–7645. https://doi.org/10.1021/jp9114755.

[72] D.A. Ward, E.I. Ko, Preparing Catalytic Materials by the Sol-Gel Method, Ind. Eng. Chem. Res. 34 (1995) 421–433. https://doi.org/10.1021/ie00041a001.

[73] B. Ferrari, R. Moreno, Electrophoretic deposition of aqueous alumina slips, J. Eur. Ceram. Soc. 17 (1997) 549–556. https://doi.org/10.1016/S0955-2219(96)00113-6.

[74] D.C.L. Vasconcelos, E.H.M. Nunes, W.L. Vasconcelos, AES and FTIR characterization

of sol-gel alumina films, J. Non. Cryst. Solids. 358 (2012) 1374–1379. https://doi.org/10.1016/j.jnoncrysol.2012.03.017.

[75] B.E. Yoldas, Hydrolysis of aluminium alkoxides and bayerite conversion, J. Appl. Chem. Biotechnol. 23 (1973) 803–809. https://doi.org/10.1002/jctb.5020231103.

[76] T. Hubert, J. Schwarz, B. Oertel, Sol-gel alumina coatings on stainless steel for wear protection, J. Sol-Gel Sci. Technol. 38 (2006) 179–184. https://doi.org/10.1007/s10971-006-6470-7.

[77] D. Cabaleiro, S. Hamze, F. Agresti, P. Estellé, S. Barison, L. Fedele, S. Bobbo, Dynamic viscosity, surface tension and wetting behavior studies of paraffin–in–water nano–emulsions, Energies. 12 (2019) 1–19. https://doi.org/10.3390/en12173334.

[78] K.I. Sarwani, R.H. Madon, S.A. Ibrahim, M. Fawzi, Effect of Calcination Temperature on Morphological and Topography of Nickel-Alumina Thin Film, MATEC Web Conf. 78 (2016). https://doi.org/10.1051/matecconf/20167801049.

[79] S.A. Adegbite, Measuring the adhesion of alumina coatings onto Fecralloy supports using a mechanical testing system, Appl. Surf. Sci. 259 (2012) 338–342. https://doi.org/10.1016/j.apsusc.2012.07.046.

[80] J.-W. Lee, C.-W. Won, B.-S. Chun, H.Y. Sohn, Dip coating of alumina films by the sol-gel method, J. Mater. Res. 8 (1993) 3151–3157. https://doi.org/10.1557/JMR.1993.3151.

[81] H. Eshtiagh-Hosseini, M.R. Housaindokht, M. Chahkandi, Effects of parameters of sol-gel process on the phase evolution of sol-gel-derived hydroxyapatite, Mater. Chem. Phys. 106 (2007) 310–316. https://doi.org/10.1016/j.matchemphys.2007.06.002.

[82] G. Bahlakeh, B. Ramezanzadeh, A Detailed Molecular Dynamics Simulation and Experimental Investigation on the Interfacial Bonding Mechanism of an Epoxy Adhesive on Carbon Steel Sheets Decorated with a Novel Cerium-Lanthanum Nanofilm, ACS Appl. Mater. Interfaces. 9 (2017) 17536–17551. https://doi.org/10.1021/acsami.7b00644.

[83] B.B. He, U. Preckwinkel, K.L. Smith, fundamentals of 2D x-ray diffraction.pdf, 43 (2000) 273–280.

[84] M. Pandey, K. Tyagi, P. Mishra, D. Saha, K. Sengupta, S.S. Islam, Nanoporous morphology of alumina films prepared by sol-gel dip coating method on alumina substrate, J. Sol-Gel Sci. Technol. 64 (2012) 282–288. https://doi.org/10.1007/s10971-012-2855-y.

[85] W. Zhou, R. Apkarian, Z.L. Wang, D. Joy, Fundamentals of scanning electron microscopy (SEM), Scanning Microsc. Nanotechnol. Tech. Appl. (2007) 1–40. https://doi.org/10.1007/978-0-387-39620-0_1.

[86] R. Ran, G. Xiong, W. Yang, An in-situ modified sol - Gel process for monolith catalyst preparation used in the partial oxidation of methane, J. Mater. Chem. 12 (2002) 1854–1859. https://doi.org/10.1039/b110820b.

[87] M.A. Butt, A. Chughtai, J. Ahmad, R. Ahmad, U. Majeed, I.H. Khan, Theory of Adhesion and its Practical Implications. A Critical Review, J. Fac. Eng. Technol. (2007) 21–45.

[88] U. Çaydaş, S. Ekici, Support vector machines models for surface roughness prediction in CNC turning of AISI 304 austenitic stainless steel, J. Intell. Manuf. 23 (2012) 639–650. https://doi.org/10.1007/s10845-010-0415-2.

[89] M. Atik, P. de Lima Neto, L.A. Avaca, M.A. Aegerter, J. Zarzycki, Protection of 316L stainless steel against corrosion by SiO2coatings, J. Mater. Sci. Lett. 13 (1994) 1081–1085. https://doi.org/10.1007/BF00633520.

[90] B. Li, X. Liu, X. Zhang, W. Chai, Stainless steel mesh coated with silica for oil-water separation, Eur. Polym. J. 73 (2015) 374–379. https://doi.org/10.1016/j.eurpolymj.2015.10.031.

[91] P. Galliano, J.J. De Damborenea, M.J. Pascual, A. Durán, Sol-Gel Coatings on 316L Steel for Clinical Applications, J. Sol-Gel Sci. Technol. 13 (1998) 723–727. https://doi.org/10.1023/a:1008653208083.

[92] M.H. Habibi, M. Khaledi Sardashti, Structure and morphology of nanostructured zinc oxide thin films prepared by dip vs. spin-coating methods, J. Iran. Chem. Soc. 5 (2008) 603–609. https://doi.org/10.1007/BF03246140.

[93] R. Balzarotti, C. Cristiani, L.F. Francis, Combined dip-coating/spin-coating depositions on

ceramic honeycomb monoliths for structured catalysts preparation, Catal. Today. 334 (2019) 90–95. https://doi.org/10.1016/j.cattod.2019.01.037.

[94] K.N. Ismail, K. Halim, K. Hamid, S.A.S.A. Kadir, M. Musa, R. Mikhail, Woven Stainless Steel Wire Mesh Supported Catalyst for NOx Reduction in Municipal Solid Waste Flue (MSW) Gas: Synthesis and Characterization, Malaysian J. Anal. Sci. 11 (2007) 246–254.

[95] Z. Wang, J. Nie, W. Qin, Q. Hu, B.Z. Tang, Gelation process visualized by aggregation-induced emission fluorogens, Nat. Commun. 7 (2016) 1–8. https://doi.org/10.1038/ncomms12033.

[96] A.N. Pavlenko, J. Zeng, N.I. Pecherkin, V.E. Zhukov, O.A. Volodin, Separation efficiency and pressure drop of SiC ceramic and Mellapak structured packings, J. Eng. Thermophys. 25 (2016) 1–14. https://doi.org/10.1134/S181023281601001X.

[97] J.J. Llano, R. Rosal, H. Sastre, F. V. Díez, Determination of Wetting Efficiency in Trickle-Bed Reactors by a Reaction Method, Ind. Eng. Chem. Res. 36 (1997) 2616–2625. https://doi.org/10.1021/ie960435o.

[98] S. Schwidder, K. Schnitzlein, A new model for the design and analysis of trickle bed reactors, Chem. Eng. J. 207–208 (2012) 758–765. https://doi.org/10.1016/j.cej.2012.07.054.

[99] M. Aldehani, F. Alzahrani, M.N.A. tSaoir, D.L.A. Fernandes, S. Assabumrungrat, F. Aiouache, Kinetics and reactive stripping modelling of hydrogen isotopic exchange of deuterated waters, Chem. Eng. Process. Process Intensif. 108 (2016) 58–73. https://doi.org/10.1016/j.cep.2016.07.008.

[100] Y. Amini, J. Karimi-Sabet, M. Nasr Esfahany, Experimental characterization of new wire gauze with high capacity structured packing, Can. J. Chem. Eng. 95 (2017) 535–542. https://doi.org/10.1002/cjce.22731.

[101] M.J. Baker, P.G. Young, G.R. Tabor, Image based meshing of packed beds of cylinders at low aspect ratios using 3d MRI coupled with computational fluid dynamics, Comput. Chem. Eng. 35 (2011) 1969–1977. https://doi.org/10.1016/j.compchemeng.2011.03.017.

[102] V. Sodhi, Trickle/pulse flow regime transition in downflow packed tower involving

foaming liquids, Chem. Ind. Chem. Eng. Q. 18 (2012) 349–359. https://doi.org/10.2298/ciceq111201011s.

[103] G. Urrutia, P. Bonelli, M.C. Cassanello, A.L. Cukierman, On dynamic liquid holdup determination by the drainage method, Chem. Eng. Sci. 51 (1996) 3721–3726. https://doi.org/10.1016/0009-2509(96)00017-6.

[104] M.I. Urseanu, J.G. Boelhouwer, H.J.M. Bosman, J.C. Schroijen, Induced pulse operation of high-pressure trickle bed reactors with organic liquids: Hydrodynamics and reaction study, Chem. Eng. Process. Process Intensif. 43 (2004) 1411–1416. https://doi.org/10.1016/j.cep.2003.09.010.

[105] P.R. Gunjal, M.N. Kashid, V. V. Ranade, R. V. Chaudhuri, Hydrodynamics of trickle bed reactors: experiments and CFD modeling, Ind. Eng. Chem. Res. 44 (2005) 6278–6294.

[106] J. Drahoš, J. Čermák, Diagnostics of gas-liquid flow patterns in chemical engineering systems, Chem. Eng. Process. 26 (1989) 147–164. https://doi.org/10.1016/0255-2701(89)90007-X.

[107] G.G. Bemer, F.J. Zuiderweg, Radial liquid spread and maldistribution in packed columns under different wetting conditions, Chem. Eng. Sci. 33 (1978) 1637–1643. https://doi.org/10.1016/0009-2509(78)85140-9.

[108] M.I. Urseanu, J.G. Boelhouwer, H.J.M. Bosman, J.C. Schroijen, G. Kwant, Estimation of trickle-to-pulse flow regime transition and pressure drop in high-pressure trickle bed reactors with organic liquids, Chem. Eng. J. 111 (2005) 5–11. https://doi.org/10.1016/j.cej.2005.04.015.

[109] D. Krieg, Origin of disturbances in cocurrent gas-liquid packed bed flows, Int. J. Multiph. Flow. 22 (1996) 95. https://doi.org/10.1016/s0301-9322(97)88140-2.

[110] Z. Tong, A. Marek, W. Hong, J.U. Repke, Experimental and numerical investigation on gravity-driven film flow over triangular corrugations, Ind. Eng. Chem. Res. 52 (2013) 15946–15958. https://doi.org/10.1021/ie303038c.

[111] L. Yang, Cfd Modeling of Multiphase Counter-Current Flow in Packed, (2015).

[112] Y. Wang, J. Chen, F. Larachi, Modelling and simulation of trickle-bed reactors using computational fluid dynamics: A state-of-the-art review, Can. J. Chem. Eng. 91 (2013) 136–180. https://doi.org/10.1002/cjce.20702.

[113] W. Du, L. Zhang, S. Lv, P. Lu, J. Xu, W. Wei, Numerical study of liquid coverage in a gas-liquid-solid packed bed, Particuology. 23 (2015) 90–99. https://doi.org/10.1016/j.partic.2014.10.013.

[114] G.M. Karthik, V. V. Buwa, Effect of particle shape on catalyst deactivation using particle-resolved CFD simulations, Chem. Eng. J. 377 (2019). https://doi.org/10.1016/j.cej.2018.10.101.

[115] D.P. Edwards, K.R. Krishnamurthy, R.W. Potthoff, Development of an improved method to quantify maldistribution and its effect on structured packing column performance, Chem. Eng. Res. Des. 77 (1999) 656–662. https://doi.org/10.1205/026387699526593.

[116] W.P. Johnson, X. Li, G. Yal, Colloid retention in porous media: Mechanistic confirmation of wedging and retention in zones of flow stagnation, Environ. Sci. Technol. 41 (2007) 1279–1287. https://doi.org/10.1021/es061301x.

[117] F. Garner, W. Broom, J. Taylor, Distillation and Absortion in Packed Columns, Ind. Eng. Chem. 27 (1935) 977–978. https://doi.org/10.1021/ie50308a600.

[118] K.E. Porter, G.K. Stephens, A method for estimating inter rivulet mixing, Can. J. Chem. Eng. 47 (1969) 258–264. https://doi.org/10.1002/cjce.5450470317.

[119] F. Yin, Z. Wang, A. Afacan, K. Nandakumar, K.T. Chuang, Experimental studies of liquid flow maldistribution in a random packed column, Can. J. Chem. Eng. 78 (2000) 449–457. https://doi.org/10.1002/cjce.5450780303.

[120] M. Zhang, Y. Li, Y. Li, H. Han, L. Teng, Numerical simulations on the effect of sloshing on liquid flow maldistribution of randomly packed column, Appl. Therm. Eng. 112 (2017) 585–594. https://doi.org/10.1016/j.applthermaleng.2016.10.049.

[121] K. Onda, H. Takeuchi, Y. Maeda, N. Takeuchi, Liquid distribution in a packed column, Chem. Eng. Sci. 28 (1973) 1677–1683. https://doi.org/10.1016/0009-2509(73)80021-1.

[122] A. Souadnia, M.A. Latifi, Analysis of two-phase ow distribution in trickle-bed reactors, Chem. Eng. Sci. 56 (2001) 5977–5985.

[123] P. Harriott, Effect Maldistribution, 23 (1989) 309–314.

[124] E. Dutkai, E. Ruckenstein, New experiments concerning the distribution of a liquid in a packed column, Chem. Eng. Sci. 25 (1970) 483–488. https://doi.org/10.1016/0009-2509(70)80046-X.

[125] Z. Solomenko, Y. Haroun, M. Fourati, F. Larachi, C. Boyer, F. Augier, Liquid spreading in trickle-bed reactors: Experiments and numerical simulations using Eulerian-Eulerian two-fluid approach, Chem. Eng. Sci. 126 (2015) 698–710. https://doi.org/10.1016/j.ces.2015.01.013.

[126] F. Alzahrani, M. Aldehani, H. Rusi, M. McMaster, D.L. Abreu Fernandes, S. Assabumrungrat, M. Nic An tSaoir, F. Aiouache, Gas Flow Visualization in Low Aspect Ratio Packed Beds by Three-Dimensional Modeling and Near-Infrared Tomography, Ind. Eng. Chem. Res. 54 (2015) 12714–12729. https://doi.org/10.1021/acs.iecr.5b02635.

[127] M.A. Basden, Characterization of Structured Packing via Computational Fluid Dynamics, (2014).

[128] J. Ellenberger, R. Krishna, Counter-current operation of structured catalytically packed distillation columns: Pressure drop, holdup and mixing, Chem. Eng. Sci. 54 (1999) 1339–1345. https://doi.org/10.1016/S0009-2509(99)00055-X.

[129] H.S. Grewal, H. Nam Kim, I.J. Cho, E.S. Yoon, Role of Viscous Dissipative Processes on the Wetting of Textured Surfaces, Sci. Rep. 5 (2015). https://doi.org/10.1038/srep14159.

[130] H. Zhang, X. Zhang, X. Yi, F. He, F. Niu, P. Hao, Effect of wettability on droplet impact: Spreading and splashing, Exp. Therm. Fluid Sci. 124 (2021) 110369. https://doi.org/10.1016/j.expthermflusci.2021.110369.

[131] D. Hlushkou, U. Tallarek, Transition from creeping via viscous-inertial to turbulent flow in fixed beds, J. Chromatogr. A. 1126 (2006) 70–85. https://doi.org/10.1016/j.chroma.2006.06.011.

[132] J.W.J. Kaiser, J.M. Winter, S. Adami, N.A. Adams, Investigation of interface deformation dynamics during high-Weber number cylindrical droplet breakup, Int. J. Multiph. Flow. 132 (2020) 103409. https://doi.org/10.1016/j.ijmultiphaseflow.2020.103409.

[133] C. Ma, M.J. Su, Y. Luo, G.W. Chu, B.C. Sun, J.F. Chen, Wetting behavior of the stainless steel wire mesh with Al2O3 coatings and mass transfer intensification in a rotating packed bed, Ind. Eng. Chem. Res. 59 (2020) 1374–1382. https://doi.org/10.1021/acs.iecr.9b04745.

[134] V. Linek, T. Moucha, F.J. Rejl, Hydraulic and mass transfer characteristics of packings for absorption and distillation columns. Rauschert-Metall-Sattel-Rings, Chem. Eng. Res. Des. 79 (2001) 725–732. https://doi.org/10.1205/026387601753192046.

[135] R. Kumar, H.J. Pant, V.K. Sharma, S. Mohan, S.M. Mahajani, Investigation of hydrodynamic behaviour of a pilot-scale trickle bed reactor packed with hydrophobic and hydrophilic packings using radiotracer technique, J. Radioanal. Nucl. Chem. 294 (2012) 71–75. https://doi.org/10.1007/s10967-011-1512-1.

[136] R. Kumar, H.J.P.V.K. Sharma, Investigation of hydrodynamic behaviour of a pilot-scale trickle bed reactor packed with hydrophobic and hydrophilic packings using radiotracer technique, (2012) 71–75. https://doi.org/10.1007/s10967-011-1512-1.

[137] P. Yan, X. Gao, Hydrodynamics and mechanism of hydrophobic foam column tray : Contact angle hysteresis effect, (2020) 1–11. https://doi.org/10.1002/aic.16793.

[138] J.P. Zhang, Y. Luo, G.W. Chu, L. Sang, Y. Liu, L.L. Zhang, J.F. Chen, A hydrophobic wire mesh for better liquid dispersion in air, Chem. Eng. Sci. 170 (2017) 204–212. https://doi.org/10.1016/j.ces.2017.03.058.

[139] M. Su, S. Bai, Y. Luo, G. Chu, B. Sun, Y. Le, Controllable wettability on stainless steel substrates with highly stable coatings, 195 (2019) 791–800. https://doi.org/10.1016/j.ces.2018.10.025.

[140] M.J. Su, Y. Le, G.W. Chu, Y. Bin Li, L.L. Zhang, Y. Luo, Intensification of Droplet Dispersion by Using Multilayer Wire Mesh and Its Application in a Rotating Packed Bed, Ind. Eng. Chem. Res. 59 (2020) 3584–3592. https://doi.org/10.1021/acs.iecr.9b07033.

[141] S.A. Kooij, A.M. Moqaddam, T.C. De Goede, D. Derome, J. Carmeliet, N. Shahidzadeh, D. Bonn, Sprays from droplets impacting a mesh, J. Fluid Mech. 871 (2019) 489–509. https://doi.org/10.1017/jfm.2019.289.

[142] K.J. Bathe, H. Zhang, A mesh adaptivity procedure for CFD and fluid-structure interactions, Comput. Struct. 87 (2009) 604–617. https://doi.org/10.1016/j.compstruc.2009.01.017.

[143] P.I. Muiruri, O.S. Motsamai, Three dimensional CFD simulations of a wind turbine blade section; validation, J. Eng. Sci. Technol. Rev. 11 (2018) 138–145. https://doi.org/10.25103/jestr.111.16.

[144] R.J.G. Lopes, R.M. Quinta-Ferreira, Three-dimensional numerical simulation of pressure drop and liquid holdup for high-pressure trickle-bed reactor, Chem. Eng. J. 145 (2008) 112–120. https://doi.org/10.1016/j.cej.2008.07.053.

[145] R.K. Singh, J.E. Galvin, X. Sun, Multiphase flow studies for microscale hydrodynamics in the structured packed column, Chem. Eng. J. 353 (2018) 949–963. https://doi.org/10.1016/j.cej.2018.07.067.

[146] Y. Liu, Y. Luo, G.W. Chu, F. Larachi, H.K. Zou, J.F. Chen, Liquid microflow inside the packing of a rotating packed bed reactor: Computational, observational and experimental studies, Chem. Eng. J. 386 (2020) 121134. https://doi.org/10.1016/j.cej.2019.03.010.

[147] T.N. Phillips, A.J. Williams, Viscoelastic flow through a planar contraction using a semi-Lagrangian finite volume method, J. Nonnewton. Fluid Mech. 87 (1999) 215–246. https://doi.org/10.1016/S0377-0257(99)00065-8.

[148] S.R. Idelsohn, E. Onate, F. Del Pin, The particle finite element method: A powerful tool to solve incompressible flows with free-surfaces and breaking waves, Int. J. Numer. Methods Eng. 61 (2004) 964–989. https://doi.org/10.1002/nme.1096.

[149] M.R. Pivello, M.M. Villar, R. Serfaty, A.M. Roma, A. Silveira-Neto, A fully adaptive front tracking method for the simulation of two phase flows, Int. J. Multiph. Flow. 58 (2014) 72–82. https://doi.org/10.1016/j.ijmultiphaseflow.2013.08.009.

[150] A. Ataki, P.D.-I.D. techn. habil. H.-J. Bart, Wetting of Structured Packing Elements -

CFD and Experiment, Fachbereich Für Maschinenbau Und Verfahrenstechnik. Dr.-Ing (2006).

[151] W. Lou, M. Zhu, Numerical simulation of gas and liquid two-phase flow in gas-stirred systems based on Euler-Euler approach, Metall. Mater. Trans. B Process Metall. Mater. Process. Sci. 44 (2013) 1251–1263. https://doi.org/10.1007/s11663-013-9897-6.

[152] D. Zuzio, A. Orazzo, J.L. Estivalèzes, I. Lagrange, A new efficient momentum preserving Level-Set/VOF method for high density and momentum ratio incompressible two-phase flows, J. Comput. Phys. 410 (2020) 109342. https://doi.org/10.1016/j.jcp.2020.109342.

[153] J.A. Rocha, J.L. Bravo, J.R. Fair, Distillation columns containing structured packings: A comprehensive model for their performance. 2. Mass-transfer model, Ind. Eng. Chem. Res. 35 (1996) 1660–1667. https://doi.org/10.1021/ie940406i.

[154] C.K. Lambert, R.D. Gonzalez, Effect of Gd2O3 and Sm2O3 addition on the properties of CeO2, J. Korean Inst. Electr. Electron. Mater. Eng. 16 (2003) 979–986. https://doi.org/10.4313/JKEM.2003.16.11.979.

[155] Z. Dong, L. Wu, J. Wang, J. Ma, L. Jiang, Superwettability Controlled Overfl ow, Adv. Mater. (2015) 1745–1750. https://doi.org/10.1002/adma.201405387.

[156] Y. Haroun, L. Raynal, P. Alix, Prediction of effective area and liquid hold-up in structured packings by CFD, Chem. Eng. Res. Des. 92 (2014) 2247–2254. https://doi.org/10.1016/j.cherd.2013.12.029.

[157] A. Ataki, H.J. Bart, Experimental and CFD simulation study for the wetting of a structured packing element with liquids, Chem. Eng. Technol. 29 (2006) 336–347. https://doi.org/10.1002/ceat.200500302.

[158] W. Du, D. Feng, J. Xu, W. Wei, Computational Fluid Dynamics Modeling of Gas-Liquid Two-Phase Flow around a Spherical Particle, Chem. Eng. Technol. 36 (2013) 840–850. https://doi.org/10.1002/ceat.201200486.

[159] F. Augier, A. Koudil, A. Royon-Lebeaud, L. Muszynski, Q. Yanouri, Numerical approach to predict wetting and catalyst efficiencies inside trickle bed reactors, Chem. Eng. Sci. 65 (2010) 255–260. https://doi.org/10.1016/j.ces.2009.06.027.

[160] J.A. Rocha, J.L. Bravo, J.R. Fair, Distillation columns containing structured packings: a comprehensive model for their performance. 1. Hydraulic models, Ind. Eng. Chem. Res. 32 (2005) 641–651. https://doi.org/10.1021/ie00016a010.

[161] X. Zhao, K.H. Smith, M.A. Simioni, W. Tao, S.E. Kentish, W. Fei, G.W. Stevens, Comparison of several packings for CO2 chemical absorption in a packed column, Int. J. Greenh. Gas Control. 5 (2011) 1163–1169. https://doi.org/10.1016/j.ijggc.2011.07.006.

[162] K. Fu, T. Sema, Z. Liang, H. Liu, Y. Na, H. Shi, R. Idem, P. Tontiwachwuthikul, Investigation of mass-transfer performance for CO 2 absorption into diethylenetriamine (DETA) in a randomly packed column, Ind. Eng. Chem. Res. 51 (2012) 12058–12064. https://doi.org/10.1021/ie300830h.

[163] A. KABA, R. AKAI, I. YAMAMOTO, A. KANAGAWA, Measurement of HETP of SUS Dixon Ring and Porcelain Packing in Small-Scale Water Distillation Column for H_2O-HTO Isotope Separation, J. Nucl. Sci. Technol. 25 (1988) 825–830. https://doi.org/10.1080/18811248.1988.9735930.

[164] R. Billet, M. Schultes, Prediction of Mass Transfer Columns with Dumped and Arranged Packings, Chem. Eng. Res. Des. 77 (1999) 498–504. https://doi.org/10.1205/026387699526520.

[165] J.M. Coulson, J. M., Richardson, J. F., and Coulson, Coulson and Richardson's chemical engineering, in: Butterworth-Heinemann, Oxford, 1999: p. 223.

[166] F.J. Bolles WL, Performance and design of packed distillation columns, in: 3rd Int. Symp. Destill., EFCE Publications Series No. 3, London, 1979: p. vol. 2, 3.3./35–89.

[167] G.E. Walker WH, Levis WK, Mc Adams WH, Principles of Chemical Engineering, 3rd ed, Mc Graw-Hill, New York, 1937.

[168] S. Piché, S. Lévesque, B.P.A. Grandjean, F. Larachi, Prediction of HETP for randomly packed towers operation: Integration of aqueous and non-aqueous mass transfer characteristics into one consistent correlation, Sep. Purif. Technol. 33 (2003) 145–162. https://doi.org/10.1016/S1383-5866(03)00005-4.

[169] A. Zakeri, A. Einbu, H.F. Svendsen, Experimental investigation of liquid holdup in

structured packings, Chem. Eng. Res. Des. 90 (2012) 585–590. https://doi.org/10.1016/j.cherd.2011.08.012.

[170] D. Sebastia-Saez, S. Gu, P. Ranganathan, K. Papadikis, Meso-scale CFD study of the pressure drop, liquid hold-up, interfacial area and mass transfer in structured packing materials, Int. J. Greenh. Gas Control. 42 (2015) 388–399. https://doi.org/10.1016/j.ijggc.2015.08.016.

[171] A.E. Sáez, R.G. Carbonell, Hydrodynamic Parameters for Gas-Liquid Cocurrent Flow in Packed Beds, AIChE J. 31 (1985) 52–62. https://doi.org/10.1002/aic.690310105.

[172] S. Aferka, M. Crine, A.K. Saroha, D. Toye, P. Marchot, In situ measurements of the static liquid holdup in Katapak-SP 12TM packed column using X-ray tomography, Chem. Eng. Sci. 62 (2007) 6076–6080. https://doi.org/10.1016/j.ces.2007.06.025.

[173] T.J. Schildhauer, I. Hoek, F. Kapteijn, J.A. Moulijn, Zeolite BEA catalysed esterification of hexanoic acid with 1-octanol: Kinetics, side reactions and the role of water, Appl. Catal. A Gen. 358 (2009) 141–145. https://doi.org/10.1016/j.apcata.2009.02.004.

[174] K. Bornhütter, A. Mersmann, Mass transfer in packed columns: The cylinder model, Chem. Eng. Technol. 16 (1993) 46–57. https://doi.org/10.1002/ceat.270160109.

[175] I. Iliuta, F. Larachi, M.H. Al-Dahhan, Multiple-zone model for partially wetted trickle flow hydrodynamics, Chem. Eng. Res. Des. 78 (2000) 982–990. https://doi.org/10.1205/026387600528256.

[176] D. Sebastia-Saez, S. Gu, P. Ranganathan, K. Papadikis, 3D modeling of hydrodynamics and physical mass transfer characteristics of liquid film flows in structured packing elements, Int. J. Greenh. Gas Control. 19 (2013) 492–502. https://doi.org/10.1016/j.ijggc.2013.10.013.

[177] L. Valenz, F.J. Rejl, V. Linek, Gas and liquid axial mixing in the column packed with Mellapak 250Y, Pall rings 25, and intalox saddles 25 under flow conditions prevailing in distillation columns, Ind. Eng. Chem. Res. 49 (2010) 10016–10025. https://doi.org/10.1021/ie101092e.

[178] D. Yang, P. Tontiwachwuthikul, Y. Gu, Dynamic interfacial tension method for

measuring gas diffusion coefficient and interface mass transfer coefficient in a liquid, Ind. Eng. Chem. Res. 45 (2006) 4999–5008. https://doi.org/10.1021/ie060047e.

[179] L. Svensson, M. Ferm, Mass Transfer Coefficient and Equilibrium Concentration as Key Factors in a New Approach to Estimate Ammonia Emission from Livestock Manure, J. Agric. Eng. Res. 56 (1993) 1–11. https://doi.org/10.1006/jaer.1993.1056.

[180] T.W. Chung, T.K. Ghosh, A.L. Hines, Comparison between Random and Structured Packings for Dehumidification of Air by Lithium Chloride Solutions in a Packed Column and Their Heat and Mass Transfer Correlations, Ind. Eng. Chem. Res. 35 (1996) 192–198. https://doi.org/10.1021/ie940652u.

[181] H.L. Shulman, C.F. Ullrich, A.Z. Proulx, J.O. Zimmerman, Performance of packed columns. II. Wetted and effective-interfacial areas, gas - and liquid-phase mass transfer rates, AIChE J. 1 (1955) 253–258. https://doi.org/10.1002/aic.690010220.

[182] K. Fu, T. Sema, Z. Liang, H. Liu, Y. Na, H. Shi, R. Idem, P. Tontiwachwuthikul, Investigation of mass-transfer performance for CO2 absorption into diethylenetriamine (DETA) in a randomly packed column, Ind. Eng. Chem. Res. 51 (2012) 12058–12064. https://doi.org/10.1021/ie300830h.

[183] I. Wagner, J. Stichlmair, J.R. Fair, Mass Transfer in Beds of Modern, High-Efficiency Random Packings, Ind. Eng. Chem. Res. 36 (1997) 227–237. https://doi.org/10.1021/ie9600194.

[184] D. Janssen, R. De Palma, S. Verlaak, P. Heremans, W. Dehaen, Static solvent contact angle measurements, surface free energy and wettability determination of various self-assembled monolayers on silicon dioxide, Thin Solid Films. 515 (2006) 1433–1438. https://doi.org/10.1016/j.tsf.2006.04.006.

[185] M. Vonka, J. Kosek, Modelling the morphology evolution of polymer materials undergoing phase separation, Chem. Eng. J. 207–208 (2012) 895–905. https://doi.org/10.1016/j.cej.2012.06.091.

[186] L.J.S. Halloran, P. Brunner, D. Hunkeler, COMPEST, a PEST-COMSOL interface for inverse multiphysics modelling: Development and application to isotopic fractionation of

groundwater contaminants, Comput. Geosci. 126 (2019) 107–119. https://doi.org/10.1016/j.cageo.2019.02.001.

[187] A. Fortin, A. Zine, An improved GMRES method for solving viscoelastic fluid flow problems, J. Nonnewton. Fluid Mech. 42 (1992) 1–18. https://doi.org/https://doi.org/10.1016/0377-0257(92)80001-E.

[188] S.C. Beutelspacher, N. Serbecic, P. Tan, M.O. McClure, Vergleich verschiedener viraler vektoren zur gentherapie von hornhautendothelzellen, Ophthalmologe. 102 (2005) 1168–1174. https://doi.org/10.1007/s00347-005-1230-6.

[189] P. Yue, J.J. Feng, C. Liu, J. Shen, A diffuse-interface method for simulating two-phase flows of complex fluids, J. Fluid Mech. 515 (2004) 293–317. https://doi.org/10.1017/S0022112004000370.

[190] R. Maiti, A. Atta, K.D.P. Nigam, Effect of particle porosity on hysteresis in trickle-bed reactors, Ind. Eng. Chem. Res. 47 (2008) 8126–8135. https://doi.org/10.1021/ie8003539.

[191] R.M. Propp, P. Colella, W.Y. Crutchfield, M.S. Day, A Numerical Model for Trickle Bed Reactors, J. Comput. Phys. 165 (2000) 311–333. https://doi.org/10.1006/jcph.2000.6604.

[192] D. Jacqmin, Calculation of Two-Phase Navier – Stokes Flows Using Phase-Field Modeling, J. Comput. Phys. 127 (1999) 96–127.

[193] R.L. Oréfice, W.L. Vasconcelos, Sol-Gel transition and structural evolution on multicomponent gels derived from the alumina-silica system, J. Sol-Gel Sci. Technol. 9 (1997) 239–249. https://doi.org/10.1007/BF02437187.

[194] B.E. Yoldas, Transparent activated nonparticulate alumina and method of preparing same, U.S. Patent 3 (1976) 941,719, Mar. 2.

[195] M. Nguefack, A.F. Popa, S. Rossignol, C. Kappenstein, Preparation of alumina through a sol-gel process. Synthesis, characterization, thermal evolution and model of intermediate boehmite, Phys. Chem. Chem. Phys. 5 (2003) 4279–4289. https://doi.org/10.1039/b306170a.

[196] R.S. Volkov, G. V. Kuznetsov, P.A. Strizhak, Water droplet deformation in gas stream:

Impact of temperature difference between liquid and gas, Int. J. Heat Mass Transf. 85 (2015) 1–11. https://doi.org/10.1016/j.ijheatmasstransfer.2015.01.078.

[197] M. Osękowska, E. Karuga-Kuźniewska, D. Wojcieszak, M. Mazur, A. Poniedziałek, D. Kaczmarek, M. Szymonowicz, Z. Rybak, Influence of nanocrystalline structure and surface properties of TiO2 thin films on the viability of L929 cells, Polish J. Chem. Technol. 17 (2015) 33–39. https://doi.org/10.1515/pjct-2015-0047.

[198] J. Stichlmair, J.L. Bravo, J.R. Fair, General model for prediction of pressure drop and capacity of countercurrent gas/liquid packed columns, Gas Sep. Purif. 3 (1989) 19–28. https://doi.org/http://dx.doi.org/10.1016/0950-4214(89)80016-7.

[199] V. Linek, P. Petricek, P. Benes, R. Braun, Effective interfacial area and liquid side mass transfer coefficients in absorption columns packed with hydriphilised and untreated plastic packings., Chem. Eng. Res. Des. 62 (1984) 13–21.

[200] J. Stichlmair, J.L. Bravo, J.R. Fair, General model for prediction of pressure drop and capacity of countercurrent gas/liquid packed columns, Gas Sep. Purif. 3 (1989) 19–28. https://doi.org/10.1016/0950-4214(89)80016-7.